Constraints on decreases in η Carinae's mass-loss from 3D hydrodynamic simulations of its binary colliding winds

T. I. Madura,[1]*† T. R. Gull,[1] A. T. Okazaki,[2] C. M. P. Russell,[2] S. P. Owocki,[3] J. H. Groh,[4] M. F. Corcoran,[5,6] K. Hamaguchi[5,7] and M. Teodoro[1]‡

[1]*Astrophysics Science Division, Code 667, NASA Goddard Space Flight Center, Greenbelt, MD 20771, USA*
[2]*Hokkai-Gakuen University, Toyohira-ku, Sapporo 062-8605, Japan*
[3]*Department of Physics and Astronomy, University of Delaware, Newark, DE 19716, USA*
[4]*Geneva Observatory, Geneva University, Chemin des Maillettes 51, CH-1290 Sauverny, Switzerland*
[5]*CRESST and X-ray Astrophysics Laboratory, NASA Goddard Space Flight Center, Greenbelt, MD 20771, USA*
[6]*Universities Space Research Association, 10211 Wisconsin Circle, Suite 500, Columbia, MD 21044, USA*
[7]*Department of Physics, University of Maryland, Baltimore County, 1000 Hilltop Circle, Baltimore, MD 21250, USA*

ABSTRACT

Recent work suggests that the mass-loss rate of the primary star η_A in the massive colliding wind binary η Carinae dropped by a factor of 2–3 between 1999 and 2010. We present results from large- (± 1545 au) and small- (± 155 au) domain, 3D smoothed particle hydrodynamics (SPH) simulations of η Car's colliding winds for three η_A mass-loss rates ($\dot{M}_{\eta_A} = 2.4$, 4.8 and $8.5 \times 10^{-4}\,\mathrm{M_\odot\,yr^{-1}}$), investigating the effects on the dynamics of the binary wind–wind collision (WWC). These simulations include orbital motion, optically thin radiative cooling and radiative forces. We find that $\dot{M}_{\eta_A}$ greatly affects the time-dependent hydrodynamics at all spatial scales investigated. The simulations also show that the post-shock wind of the companion star η_B switches from the adiabatic to the radiative-cooling regime during periastron passage ($\phi \approx 0.985$–1.02). This switchover starts later and ends earlier the lower the value of $\dot{M}_{\eta_A}$ and is caused by the encroachment of the wind of η_A into the acceleration zone of η_B's wind, plus radiative inhibition of η_B's wind by η_A. The SPH simulations together with 1D radiative transfer models of η_A's spectra reveal that a factor of 2 or more drop in $\dot{M}_{\eta_A}$ should lead to substantial changes in numerous multiwavelength observables. Recent observations are not fully consistent with the model predictions, indicating that any drop in $\dot{M}_{\eta_A}$ was likely by a factor of $\lesssim 2$ and occurred after 2004. We speculate that most of the recent observed changes in η Car are due to a small increase in the WWC opening angle that produces significant effects because our line of sight to the system lies close to the dense walls of the WWC zone. A modest decrease in $\dot{M}_{\eta_A}$ may be responsible, but changes in the wind/stellar parameters of η_B, while less likely, cannot yet be fully ruled out. We suggest observations during η Car's next periastron in 2014 to further test for decreases in $\dot{M}_{\eta_A}$. If $\dot{M}_{\eta_A}$ is declining and continues to do so, the 2014 X-ray minimum should be even shorter than that of 2009.

Key words: hydrodynamics – binaries: close – stars: mass-loss – stars: individual: Eta Carinae – stars: winds, outflows.

1 INTRODUCTION

Deep within Eta Carinae's spectacular bipolar 'Homunculus' nebula lies an extremely luminous ($L_{\mathrm{Total}} \gtrsim 5 \times 10^6\,\mathrm{L_\odot}$) collid-

ing wind binary with a highly eccentric ($e \sim 0.9$), 5.54 yr orbit (Damineli, Conti & Lopes 1997; Hillier et al. 2001; Damineli et al. 2008a,b; Corcoran et al. 2010). The primary of the system, η_A, is our closest (2.3 ± 0.1 kpc, Smith 2006) example of a very massive star. A luminous blue variable (LBV) with a current mass of $\sim 100\,\mathrm{M_\odot}$ and a powerful stellar wind with a mass-loss rate $\dot{M} \approx 8.5 \times 10^{-4}\,\mathrm{M_\odot\,yr^{-1}}$ and terminal speed $v_\infty \approx 420\,\mathrm{km\,s^{-1}}$ (Hillier et al. 2001, 2006; Groh et al. 2012a, hereafter H01, H06 and G12a, respectively), η_A is in a relatively short and poorly

---

understood stage of stellar evolution. Such very massive stars can lose substantial amounts of mass in giant, violent outbursts as they rapidly transition from hydrogen burning to helium core burning (Conti 1984; Humphreys & Davidson 1994). The most prominent illustration of this is the mid-1840s 'Great Eruption' of Eta Carinae (η Car), wherein $\sim$10–20 M$_\odot$ was ejected over a period of $\sim$5–15 yr, forming the Homunculus nebula (Davidson & Humphreys 1997; Smith 2006). Evidence indicates that such strong mass-loss dominates the evolution of the most massive ($\gtrsim$40 M$_\odot$) stars (see e.g. Smith & Owocki 2006). The physical mechanisms leading to these eruptions are not well understood, in either single stars (Smith & Owocki 2006; Smith & Townsend 2007; Quataert & Shiode 2012) or binaries (Ofek et al. 2007; Smith 2011). Determining their cause is of fundamental importance for understanding how very massive stars evolve into supernovae (SNe), gamma-ray bursts and black holes.

Ground- and space-based multiwavelength observations over the last two decades show that η_A has a less-luminous binary companion, η_B (Damineli et al. 1997; Ishibashi et al. 1999; Smith et al. 2004b; Whitelock et al. 2004; Damineli et al. 2008a,b; Gull et al. 2009; Fernández-Lajús et al. 2010; Corcoran et al. 2010, hereafter C10). Some of the strongest evidence for binarity comes from extended X-ray monitoring of the system (Ishibashi et al. 1999; Corcoran 2005; Hamaguchi et al. 2007; C10). η Car's *Rossi X-ray Timing Explorer* (*RXTE*) light curve is characteristic of a highly eccentric colliding wind binary, the variable X-ray emission arising in a wind–wind collision (WWC) shock zone formed between the stars (Pittard & Corcoran 2002; Parkin et al. 2009, 2011, hereafter P09 and P11; C10). The hard X-ray spectrum ($kT \approx 4-5$ keV) requires that η_B have an unusually high wind terminal speed of $\sim$3000 km s^{-1}, while modelling of the X-ray spectrum suggests an enormous mass-loss rate of $\sim$10^{-5} M$_\odot$ yr^{-1} (Pittard & Corcoran 2002; P09). Due to η_A's immense brightness, η_B has never been directly observed. Nonetheless, studies of the photoionization effects of η_B on the circumstellar ejecta known as the 'Weigelt blobs' (Weigelt & Ebersberger 1986) have helped constrain η_B's temperature ($T_{\rm eff} \sim$ 37 000–43 000 K) and luminosity (log L/L$_\odot \sim$ 5–6, Verner, Bruhweiler & Gull 2005; Mehner et al. 2010).

Monitoring of η Car with *RXTE* and *Swift* shows that, broadly speaking, the X-ray flux repeats itself from orbit to orbit with more consistency than is shown in any other waveband (C10; Corcoran 2011). Surprisingly, the observed X-ray minimum in 2009 was $\sim$50 per cent shorter than the minima of 1998 and 2003.5 (fig. 3 of C10). The sudden recovery of the X-ray flux in 2009 probably represents a change in the cooling of the WWC shock due to currently unknown reasons (P09; P11). Simple calculations suggest a large reduction in η_A's $\dot{M}$, of a factor of $\sim$2–4, is needed to match the reduced 2009 minimum (C10).

Spectroscopic changes observed in stellar-wind emission features such as Hα are also interpreted as being due to a secular decrease of η_A's mass-loss rate (by a factor of 2–3 between 1999 and 2010, Mehner et al. 2010, 2011, 2012). However, monitoring of Balmer Hδ wind lines shows no significant changes in the inner wind of η_A (Teodoro et al. 2012). Moreover, while a secular change is visible in various wind profiles for a direct view of the central source, little to no change is seen in wind profiles at high stellar latitudes or reflected off of the Weigelt blobs (Gull et al. 2009; Mehner et al. 2012). Model stellar spectra also predict that a factor of 2 or more change in the $\dot{M}$ of η_A should lead to very significant changes in the observed spectrum (H06). He I wind lines should become very bright, while lines of Fe II should nearly disappear (fig. 11 of H06).

Such changes have not been observed, and so the puzzle of what recently occurred in η Car remains.

Here, we present results from large- ($\pm$1545 au) and small- ($\pm$155 au) domain, 3D smoothed particle hydrodynamics (SPH) simulations of η Car's massive colliding winds for three different mass-loss rates of η_A (2.4, 4.8 and 8.5 $\times$ 10^{-4} M$_\odot$ yr^{-1}). The goal is to investigate how decreases in η_A's $\dot{M}$ affect the 3D geometry and dynamics of η_A's optically thick wind and spatially extended WWC regions, both of which are known sources of observed X-ray, optical, UV and near-infrared (IR) emission and absorption (Pittard & Corcoran 2002; van Boekel et al. 2003; Martin et al. 2006b; Nielsen et al. 2007; Weigelt et al. 2007; Gull et al. 2009, 2011; P09, C10; Groh et al. 2010a,b; P11; G12a; Madura & Groh 2012; Madura et al. 2012; Teodoro et al. 2012). We use several computational domain sizes in order to better understand how the various observables that form at different length-scales may be influenced by declines in η_A's $\dot{M}$. This is the first such parameter study of η Car in 3D, which is essential since orbital motion greatly affects the shape and dynamics of the WWC zones during periastron passage (Okazaki et al. 2008, P09; P11; Madura & Groh 2012; Madura et al. 2012). The simulations in this paper can help constrain η Car's recent mass-loss history and possible future state.

The following section describes the 3D SPH simulations, while Section 3 presents the results. A qualitative discussion of the observational implications is in Section 4. Section 5 summarizes our conclusions and outlines the direction of future work.

2 THE 3D SPH SIMULATIONS

The hydrodynamical simulations in this paper were performed with an improved version of the 3D SPH code used in Okazaki et al. (2008) and Madura et al. (2012, hereafter M12), which is based on a version originally developed by Benz et al. (1990) and Bate, Bonnell & Price (1995), to which we refer the reader for further details. The linear and non-linear SPH artificial viscosity parameters are $\alpha_{\rm SPH} = 1$ and $\beta_{\rm SPH} = 2$, respectively (Okazaki et al. 2008). Optically thin radiative cooling is now implemented using the Exact Integration scheme of Townsend (2009). The radiative cooling function $\Lambda(T)$ is calculated with CLOUDY 90.01 (Ferland et al. 1998) for an optically thin plasma with solar abundances. The pre-shock stellar winds and rapidly cooling dense gas in the WWC region are assumed to be maintained at a floor temperature = 10^{4}K due to photoionization heating by the stars (P11). The same initial temperature is assumed for both winds for simplicity. The effect of the initial wind temperature ($T_{\rm wind}$) on the flow dynamics is negligible (Okazaki et al. 2008).

Radiative forces are incorporated in the SPH code via an 'antigravity' formalism developed by two of us (ATO and SPO), the details of which can be found in Appendix A and Russell (2013). We parametrize the individual stellar winds using the standard 'beta-velocity law' $v(r) = v_\infty(1 - R_\star/r)^\beta$, where v_∞ is the wind terminal velocity, $R_\star$ the stellar radius and β a free parameter describing the steepness of the velocity law. Effects due to 'radiative braking,' in which one of the stellar winds experiences a sudden deceleration before reaching the WWC zone (Gayley, Owocki & Cranmer 1997, P11) are not included. Such braking effects are not expected to play a prominent role in η Car (P09; P11; Russell 2013). We include the more important velocity-altering effects of 'radiative inhibition' (RI), in which one star's radiation field reduces the net rate of acceleration of the opposing star's wind (Stevens & Pollock 1994, P09; P11). However, because we fix the stellar mass-loss rates in

our antigravity approach, possible changes to the mass-loss due to RI are not included. These mass-loss changes are not expected to be significant in η Car and should not greatly affect our results or conclusions (see Appendix A3 for details).

Using a standard *xyz* Cartesian coordinate system, the binary orbit is set in the *xy* plane, with the origin at the system centre-of-mass (COM) and the major axis along the *x*-axis. The two stars orbit counter-clockwise when viewed from the +*z*-axis. By convention, $t = 0$ ($\phi = t/2024 = 0$) is defined as periastron. Simulations are started with the stars at apastron and run for multiple consecutive orbits. Orbits are numbered such that $\phi = 1.5, 2.5$ and 3.5 correspond to apastron at the end of the second, third and fourth full orbits, respectively.

The outer spherical simulation boundary is set at $r = 10a$ and $100a$ from the system COM for the small- and large-domain simulations, respectively, where $a = 15.45$ au is the length of the orbital semimajor axis. Particles crossing this boundary are removed from the simulations. The total number of SPH particles used in the small- and large-domain simulations is roughly the same (between $\sim 5 \times 10^5$ and 9×10^5, depending on the value of the primary $\dot{M}$). The small-domain simulations are better suited for studying the complex physics and geometry of the WWC zone very close to the central stars where most of the instantaneous changes observed in numerous spectral lines, the optical/near-IR/radio continuum fluxes and X-rays across η Car's 5.54 yr orbital cycle occur (see e.g. Damineli et al. 2008b).

The large-domain simulations are comparable in size to past and planned *Hubble Space Telescope*/Space Telescope Imaging Spectrograph (*HST*/STIS) mapping observations of the interacting stellar winds in η Car's central core ($\sim \pm 0.67$ arcsec $\approx \pm 1540$ au, Gull et al. 2011; M12; Teodoro et al. 2013). As demonstrated by Gull et al. (2011) and M12, 3D simulations at this scale are necessary for understanding and modelling the extended, time-variable forbidden line emission structures that are spatially and spectrally resolved by *HST*/STIS. We note that the SPH formalism is ideally suited for such large-scale 3D simulations due to the significantly decreased computational cost, as compared to grid-based hydrodynamics codes (Price 2004; Monaghan 2005).

The adopted simulation parameters (Table 1) are consistent with those derived from the available observations, although there has been some debate on the exact value of η_A's mass-loss rate (hereafter $\dot{M}_{\eta_A}$). For the current study, we investigate three values of $\dot{M}_{\eta_A}$, which we refer to as Cases A−C. The largest adopted value, 8.5×10^{-4} M$_\odot$ yr^{-1} (Case A), is based on the latest CMFGEN radiative transfer model fits to *HST*/STIS spatially resolved spectroscopic observations of η Car (G12a). H01, H06, Davidson et al. (1995) and Cox et al. (1995) derived a mass-loss rate of 10^{-3} M$_\odot$ yr^{-1} and a wind terminal speed of 500 km s^{-1} for η_A. The good match between the synthetic [Fe III] spectroimages of M12 and *HST*/STIS observations taken between 1998 and 2004 (Gull et al. 2009) further suggests $\dot{M}_{\eta_A}$ was $\sim 10^{-3}$ M$_\odot$ yr^{-1} during that time. G12a improved upon the original model fits of H01, H06 by using a slightly lower $\dot{M}_{\eta_A}$ (8.5×10^{-4} M$_\odot$ yr^{-1}) and v_∞ (420 km s^{-1}). The optical and UV spectra modelled by G12a were taken by *HST* in 2000 March and 2001 April, corresponding to a phase near apastron. We adopt the G12a value and assume it as the initial $\dot{M}_{\eta_A}$ before any possible drop after 2001. We also use the same v_∞ for η_A ($v_{\infty,\eta_A} = 420$ km s^{-1}) in each simulation.

Our second adopted $\dot{M}_{\eta_A}$ (4.8×10^{-4} M$_\odot$ yr^{-1}, Case B) is consistent with that derived by P09 and used in the 3D adaptive mesh refinement (AMR) hydrodynamical simulations of P11. The lowest value of $\dot{M}_{\eta_A}$ used in our simulations (2.4×10^{-4} M$_\odot$ yr^{-1}, Case C)

Table 1. Stellar, wind and orbital parameters of the 3D SPH simulations.

Parameter	η_A	η_B	Reference
$M_\star$ (M$_\odot$)	90	30	H01, O08
$R_\star$ (R$_\odot$)	60	30	H01, H06
$T_{\rm wind}$ (10^4 K)	3.5	3.5	O08, this work
$\dot{M}$ (10^{-4} M$_\odot$ yr^{-1})	8.5, 4.8, 2.4	0.14	G12a, P09
v_∞ (km s^{-1})	420	3000	G12a, PC02
β	1	1	H01, G12a
η	0.12, 0.21, 0.42		this work
q	22.28, 15.22, 9.59		H01, P09, this work
$P_{\rm orb}$ (d)	2024		D08a
e	0.9		C01, P09
a (au)	15.45		C01, O08

Notes. $M_\star$ and $R_\star$ are the stellar mass and radius. $T_{\rm wind}$ is the initial wind temperature. $\dot{M}$, v_∞ and β are the stellar-wind mass-loss rate, terminal speed and velocity-law index, respectively. $\eta \equiv (\dot{M}v_\infty)_{\eta_B}/(\dot{M}v_\infty)_{\eta_A}$ is the secondary/primary wind momentum ratio, q is the primary/secondary stellar luminosity ratio assuming $L_{\star,\eta_A} = 5 \times 10^6$ L$_\odot$, $P_{\rm orb}$ is the period, e is the eccentricity and a is the length of the orbital semimajor axis.
References: C01: Corcoran et al. (2001); H01: Hillier et al. (2001); PC02: Pittard & Corcoran (2002); H06: Hillier et al. (2006); D08a: Damineli et al. (2008a); O08: Okazaki et al. (2008); P09: Parkin et al. (2009); G12a: Groh et al. (2012a).

is nearly identical to the $\dot{M}_{\eta_A}$ obtained by Pittard & Corcoran (2002) in their attempts, using 2D hydrodynamical simulations of the colliding winds, to fit a *Chandra* grating spectrum of η Car collected near apastron. This same $\dot{M}_{\eta_A}$ was later used by Okazaki et al. (2008) in a 3D SPH simulation to model η Car's *RXTE* X-ray light curve. We note that all of the X-ray modelling studies mentioned assume wind terminal speeds of 500 and 3000 km s^{-1} for η_A and η_B, respectively, and that we use the same $\dot{M}$ and v_∞ as P11 for η_B (Table 1).

3 RESULTS

3.1 Small-domain simulations

We begin with the results of our $r = 10a$ simulations, focusing on slices in the orbital plane. Results for slices in the *xz* and *yz* planes are in Appendix B1. Movies of the simulations are also available in the online version of this paper (see Supporting Information).

Figs 1 and 2 display the density and temperature at five select orbital phases, demonstrating the key features of the WWC and the effects of orbital motion. As in previous 3D simulations (Okazaki et al. 2008; P11; Madura & Groh 2012; M12), the fast, low-density wind of η_B carves a large cavity out of the slower, denser wind of η_A for most of the 5.54 yr orbit. Around apastron (row a of both figures) when orbital speeds are their lowest (~ 14 km s^{-1} for η_B with respect to the system COM), this cavity and the WWC zone maintain the expected axisymmetric conical shape. The measured half-opening angle of each shock cone (55°, 65° and 75° for $\eta \approx 0.12, 0.21$ and 0.42, respectively) is consistent with that predicted by the analytic asymptotic formula (28) of Canto, Raga & Wilkin (1996) (53°.5, 62°.4 and 74°.2) and increases as the value of $\dot{M}_{\eta_A}$ decreases. This increase is due to the changing wind momentum balance, which also moves the apex of the WWC zone closer to η_A. At apastron, the WWC apex is ~ 22 au (18 au) from η_A when $\eta \approx 0.12$ (0.42).

The WWC zone in each simulation consists of a distended shock containing hot ($T \gtrsim 10^6$ K), low-density η_B wind material and a
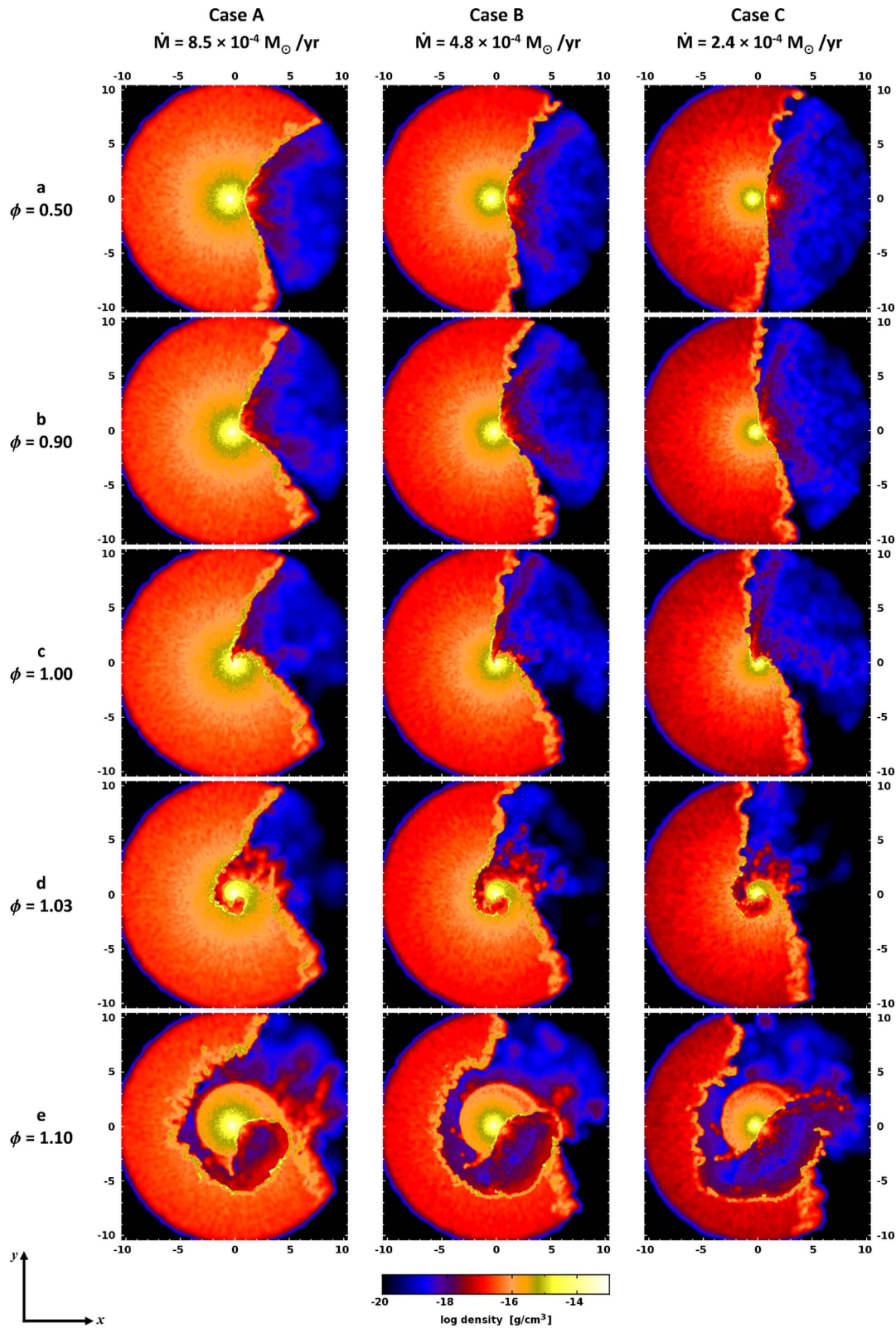
Figure 1. Slices in the orbital plane from the small-domain 3D SPH simulations of η Car (Table 1) at orbital phases $\phi = 0.5$ (apastron), 0.9, 1.0 (periastron), 1.03 and 1.10 (rows, top to bottom). Columns correspond to the three assumed η_A mass-loss rates. Colour shows log density in cgs units. The spherical computational domain size is $r = 10a \approx 155$ au ≈ 0.067 arcsec ($D = 2.3$ kpc). Axis tick marks correspond to an increment of $1a \approx 15.45$ au. The orbital motion of the stars is counter-clockwise. η_A is to the left and η_B is to the right at apastron.

Case A
$\dot{M} = 8.5 \times 10^{-4}$ M$_\odot$ /yr

Case B
$\dot{M} = 4.8 \times 10^{-4}$ M$_\odot$ /yr

Case C
$\dot{M} = 2.4 \times 10^{-4}$ M$_\odot$ /yr

a
$\phi = 0.50$

b
$\phi = 0.90$

c
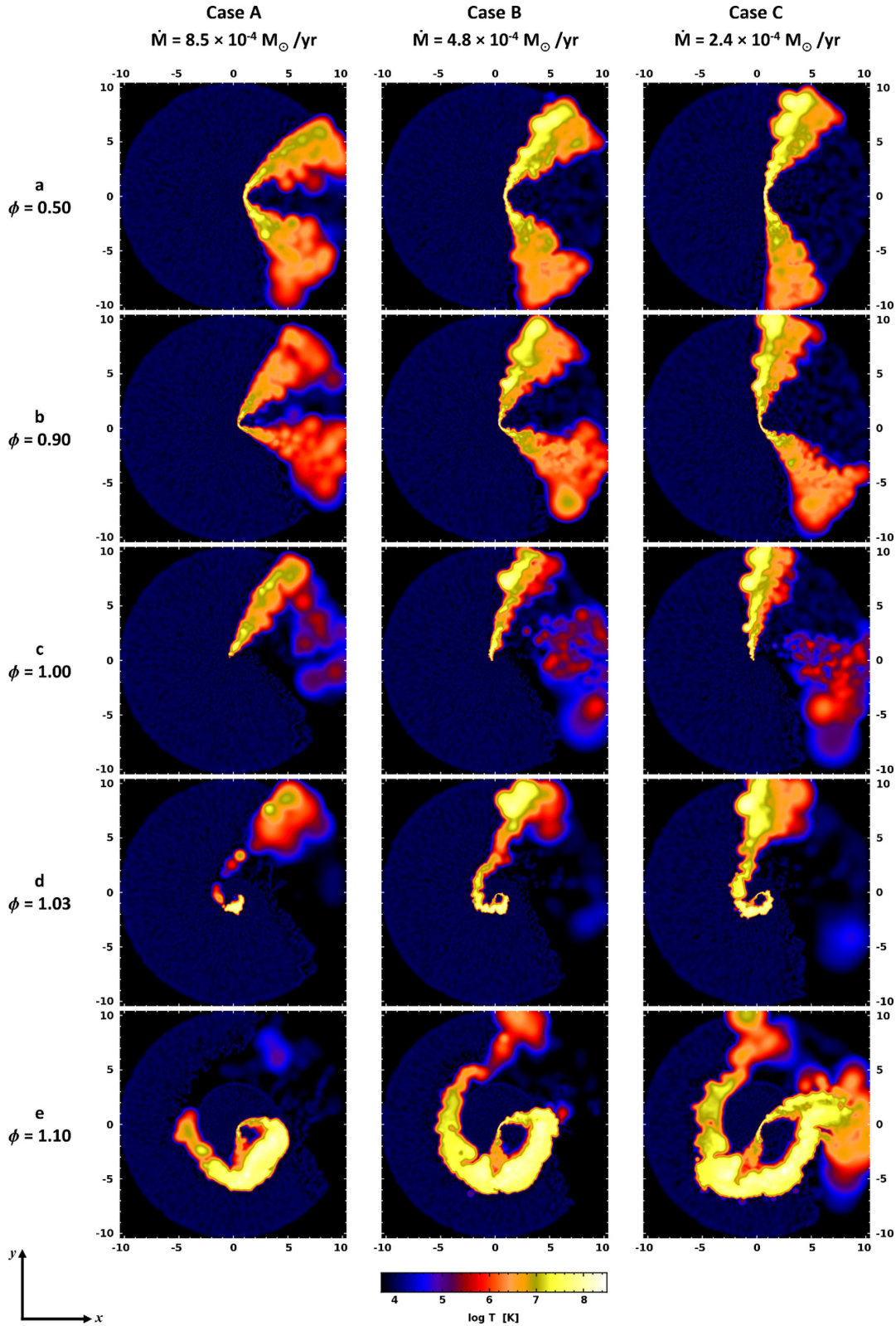$\phi = 1.00$

d
$\phi = 1.03$

e
$\phi = 1.10$

log T [K]

Figure 2. Same as Fig. 1, but with colour showing log temperature.

much thinner, colder ($T \approx 10^4$ K) region of dense post-shock η_A wind material, separated by a contact discontinuity (CD). The post-shock density of the η_A wind is roughly an order of magnitude larger than the pre-shock density. The post-shock density of the η_B

wind is approximately a factor of 4 higher than the pre-shock density, as expected for adiabatic shocks. The slower, denser η_A wind radiates more efficiently and has a characteristic cooling parameter $\chi \equiv t_{\rm cool}/t_{\rm escape} = v_8^4 d_{12}/\dot{M}_{-7} \ll 1$ (where v_8 is the pre-shock

wind velocity in units of $1000 \, \mathrm{km \, s^{-1}}$, d_{12} is the distance to the CD in units of $10^{12} \, \mathrm{cm}$ and $\dot{M}_{-7}$ is the mass-loss rate in units of $10^{-7} \, \mathrm{M_\odot \, yr^{-1}}$, see Stevens, Blondin & Pollock 1992). The lower density, high-velocity η_B wind has $\chi > 1$ and is adiabatic for most of the orbit. The maximum expected post-shock temperature in the η_B wind ($T = 3\bar{m}v_w^2/16k$, where $\bar{m} = 10^{-24} \, \mathrm{g}$ is the average mass per particle assuming solar abundances, v_w is the pre-shock wind speed and k is Boltzmann's constant, Stevens et al. 1992) at apastron is $\sim 1.2 \times 10^8 \, \mathrm{K}$, which is very near what is observed in the simulations at the WWC apex ($\sim 10^8 \, \mathrm{K}$, Fig. 2).

The overall fraction of η_B's wind shocked to high temperatures increases with $\dot{M}_{\eta_\mathrm{A}}$. The areas where the post-shock η_B wind is hottest (in bright yellow in rows a and b of Fig. 2) increase in size as $\dot{M}_{\eta_\mathrm{A}}$ is decreased. This is because for a given pre-shock wind speed, oblique shocks (like those in Case A) are less efficient at thermalizing the flow and produce lower post-shock temperatures (Pittard 2009). In contrast, Cases B and C have WWC zones that are more normal to the pre-shock flow, resulting in higher post-shock temperatures in the outer wings of the WWC region.

The post-shock η_A wind region appears to become somewhat thinner and less dense the lower the value of $\dot{M}_{\eta_\mathrm{A}}$. Since the colliding winds have very different speeds there is a velocity shear across the CD that can excite Kelvin–Helmholtz (KH) instabilities (Stevens et al. 1992; P11). The thin, dense and rapidly cooling post-shock η_A wind is also subject to non-linear thin-shell instabilities (NTSIs, Vishniac 1994; P11). As $\dot{M}_{\eta_\mathrm{A}}$ is decreased, the WWC zone seems to become more unstable. One possible reason for this is because the time-scale for exponential growth of the KH instability is $\propto \sqrt{\rho_1 \rho_2}/(\rho_1 + \rho_2)$, where ρ_1 and ρ_2 are the densities on the two sides of the CD (Stevens et al. 1992). Therefore, as $\dot{M}_{\eta_\mathrm{A}}$ is lowered, ρ_1 decreases and the growth time-scale for the KH instability shortens. We note, however, that standard SPH schemes are notorious for under-resolving the KH instability (Agertz et al. 2007; Price 2008), so these results should be interpreted with caution. In the case of the NTSI, the overall stability of a dense shell depends on the shell's thickness (Vishniac 1994; Blondin & Koerwer 1998). The thicker, denser compressed 'shell' of primary wind in Case A is thus probably less prone to the NTSI.

The aberration angle and degree of downstream curvature of the WWC zone are determined by the ratio of the orbital speed to the pre-shock wind speed (Parkin & Pittard 2008; Pittard 2009). As the stars approach periastron, the orbital speed of η_A relative to η_B ($\approx 360 \, \mathrm{km \, s^{-1}}$) increases to a value near its wind speed (420 km s^{-1}), thus highly distorting the WWC zone (Fig. 1, rows b and c). The increasing orbital speeds furthermore cause the post-shock η_B gas in the leading arm of the WWC zone to be heated to higher temperatures than the gas in the trailing arm (rows b and c of Fig. 2), a result also found by P11.

Because of the high orbital eccentricity, at $\phi \sim 0.97$–1.0, η_B and the WWC apex become deeply embedded in η_A's dense wind (row c of Figs 1 and 2). The rapid decrease in stellar separation at these phases and the adopted $\beta = 1$ velocity laws cause the two winds to collide before η_B's wind can reach its terminal speed. This, combined with RI of η_B's wind by η_A, leads to a significant decrease in the pre-shock velocity of η_B's wind (compared to phases around apastron, see Appendix A). The associated drop in η_B's wind momentum moves the WWC apex closer to η_B and decreases the WWC-zone's opening angle. Because of these effects, the trailing wind of η_B is unable to collide with η_A's downstream wind. As a result, the post-shock η_B wind in the trailing arm of the WWC zone cools below $10^6 \, \mathrm{K}$, making the hot shock noticeably asymmetric just before and at periastron (Fig. 2, row c). The higher the value of $\dot{M}_{\eta_\mathrm{A}}$, the earlier this process starts, with the hot gas in the trailing arm vanishing at $\phi \approx 0.985$ (0.995) in Case A (Case C). There is also a 'collapse' of the WWC zone around periastron (see Section 3.1.1 for details).

Rapid orbital motion during periastron passage distorts the WWC region, giving it a distinct spiral shape that is clearly visible at $\phi = 1.03$ (Figs 1 and 2, row d). The wind of η_B also carves a narrow, low-density spiral cavity in the back side of η_A's wind. This cavity flows in the $-x$ and $-y$ directions following periastron (rows d and e of Figs 1 and 2). The width of the cavity increases with decreasing $\dot{M}_{\eta_\mathrm{A}}$ due to the change in the wind momentum balance. The high-velocity η_B wind in the cavity also continuously ploughs into the denser, slower η_A wind that flows in the $-x$ and $-y$ directions. This makes the compressed wall or 'shell' of η_A wind material grow in density and accelerate to speeds a few hundred km s^{-1} greater than $v_{\infty,\eta_\mathrm{A}}$. The lower the $\dot{M}_{\eta_\mathrm{A}}$, the greater the outflow speed of the shell due to the more similar wind momenta. As the shell sweeps up more mass, it gradually slows to velocities comparable to $v_{\infty,\eta_\mathrm{A}}$. The thickness and density of the spiral shell of η_A wind also decrease with decreasing $\dot{M}_{\eta_\mathrm{A}}$.

At $\phi \approx 1.03$, the dense layer of post-shock η_A wind located in the trailing arm of the WWC region is photo-ablated by the intense stellar radiation fields. P11 originally identified this photo-ablation in their 3D AMR simulations. Interestingly, only in Case A does the photo-ablation cut off or 'snip' the spiral tail of the η_B wind cavity (row d of Figs 1 and 2). This snipping off of the cavity prevents the η_B wind from colliding with and heating the downstream η_A wind, causing a noticeable asymmetry in the temperature structure of the post-shock η_B gas in the spiral cavity. In Case A, only η_B wind that lies in the cavity in the forward direction remains hot, while material in the trailing direction cools to $T \sim 10^4 \, \mathrm{K}$. In Cases B and C, the entire η_B wind cavity is hot, with $T \gtrsim 10^6 \, \mathrm{K}$. The temperature asymmetry seen in Case A remains as the gas flows outward and is also visible at $\phi = 1.1$ (Fig. 2, row e).

Recovery of the WWC zone following periastron takes longer the higher the value of $\dot{M}_{\eta_\mathrm{A}}$. In Case A, the hot η_B-wind shock does not fully return until $\phi \approx 1.025$, whereas in Case C, the hot shock returns by $\phi \approx 1.015$ (see Section 3.1.1 for details). After periastron, η_B moves in front of η_A, its wind colliding with and heating the denser wind of η_A that flows unobstructed in the $+x$, $-y$ direction (row e of Figs 1 and 2). At $\phi \approx 1.1$, the arms of the WWC zone are so distorted by orbital motion that the leading arm collides with the old trailing arm formed before periastron passage. The lower the value of $\dot{M}_{\eta_\mathrm{A}}$, the sooner this collision takes place. The leading arm of the WWC zone, including the portion that collides with the old trailing arm, helps form another compressed shell of η_A wind that flows in the $+x$ and $-y$ directions after periastron (row e). The higher the $\dot{M}_{\eta_\mathrm{A}}$, the greater the mass in this shell and the slower it travels outward. Eventually, orbital speeds decrease and the WWC zone and η_B wind cavity regain their axisymmetric conical shape as the system moves slowly back towards apastron.

3.1.1 'Collapse' of the WWC zone during periastron passage

P09 and P11 showed that RI likely reduces the pre-shock velocity of η_B's wind during periastron passage, resulting in lower post-shock temperatures and rapid cooling of the post-shock η_B gas. Such rapid cooling can catastrophically disrupt the WWC zone via NTSIs, leading to a 'collapse', with dense fragments of post-shock η_A wind being driven into the acceleration zone of η_B's wind and sometimes colliding with η_B (P11). It has been postulated that such

a WWC collapse could explain η Car's observed extended X-ray minima in 1998 and 2003, with the shorter 2009 minimum caused by the lack of a collapse for some unknown reason (P09; C10; P11; Russell 2013).

3D AMR simulations of η Car by P11 surprisingly did not show the expected collapse of the WWC zone around periastron. Rapid orbital motion, which increases the pre-shock wind velocity and post-shock pressure of η_B's wind, is one key factor that helped prevent a collapse (P11). A second likely factor is the relatively weak coupling between η_A's radiation field and η_B's wind adopted for the simulations. P11 suggest that different couplings could result in stronger inhibition that leads to a disruption and collapse of the WWC zone on to η_B. Due to the high computational cost of 3D AMR simulations, P11 did not investigate other radiation–wind couplings. They were thus unable to demonstrate a WWC collapse around periastron in a 3D simulation that includes orbital motion.

Since orbital motion, radiative cooling and the velocity-altering effects of RI are included in our simulations, they provide a means to investigate further the possibility of a WWC collapse around periastron. Here, we focus on the inner $\pm 1a \approx \pm 15.45$ au region in the orbital plane during periastron passage ($\phi = 0.97 - 1.03$). In order to ensure that we are adequately resolving the WWC shocks and any possible WWC collapse, we performed a series of very small domain 3D SPH simulations with a computational domain size of $r = 1.5a$ and eight times the number of particles used in the $r = 10a$ simulations, leading to a roughly factor of 2 improvement in the overall spatial resolution compared to the $r = 10a$ simulations. We begin with the $\dot{M}_{\eta_A} = 8.5 \times 10^{-4}\,\mathrm{M_\odot\,yr^{-1}}$ simulation results (Fig. 3).

At $\phi = 0.98$ (Fig. 3, row a), we find that the pre-shock speed of η_B's wind along the line of centres is significantly reduced to $\sim$1950 km s^{-1}. The stellar separation at $\phi = 0.98$ ($\approx$5 au) is small enough for the two winds to collide while η_B's wind is still accelerating. The expected pre-shock speed of η_B's wind along the line of centres at $\phi = 0.98$ when assuming $\beta = 1$ wind-velocity laws and taking into account orbital motion is $\sim$2770 km s^{-1}. RI of η_B's wind by η_A explains the difference. Using the analysis in Appendix A2, the computed expected total η_B wind speed along the line of centres ($v_{2,\,\mathrm{tot}}$) at the location of ram pressure balance $r_b \approx 1.03$ au (equation A19) is $\approx$1953 km s^{-1}, in excellent agreement with the 1950 km s^{-1} found in the SPH simulation. Even at apastron, we find that η_B's pre-shock wind speed in the simulation is reduced to $\sim$2850 km s^{-1}, compared to the expected 2944 km s^{-1} when using simple $\beta = 1$ velocity laws (Fig. A3).

Due to the lower wind speed and shorter distance to the CD at $\phi = 0.98$, the colliding η_B wind heats to lower temperatures. The shorter distance to the CD also increases the pre- and post-shock η_B wind densities. The cooling parameter χ in the post-shock η_B wind near the WWC apex drops to $\sim$1.6 (Fig. 4). The post-shock temperature in the η_B wind at the WWC apex is reduced, which decreases the post-shock thermal pressure that helps support the WWC zone (P11). The lowered η_B wind speed also alters the wind momentum ratio and decreases the WWC opening angle.

Between $\phi = 0.98$ and 0.99, the stellar separation drops to $\sim$3 au and the winds collide at progressively deeper locations within the acceleration zone of η_B's wind. RI of η_B's wind by η_A also becomes stronger (Fig. A3). During this time, the pre-shock η_B wind speed along the line of centres in the simulation drops to $\sim$1500 km s^{-1} (Fig. 3). The WWC opening angle decreases further, the WWC apex moves closer to η_B, χ drops to well below unity (Fig. 4) and radiative cooling takes over. The post-shock η_B wind near the WWC apex now cools quickly to $T \approx 10^4$ K. At this point, we observe

a 'collapse' (P09; P11) or 'discombobulation' (Davidson 2002; Martin et al. 2006b) of the inner WWC region. Since a WWC zone is still present (although highly unstable due to the two radiative shocks), we believe it is more appropriate to say that the post-shock η_B wind undergoes a 'cooling-transition' phase. The entire apex and old trailing arm of the hot η_B-shock vanish (Fig. 3, rows b and c) as the post-shock η_B gas switches from the adiabatic to the radiative-cooling regime. With the thermal pressure from the hot η_B wind gone, the cold, dense η_A wind can penetrate deep into η_B's wind and come very close to the star, $\sim$3.5 $R_{\star,\eta_B}$ ($\sim$0.5 au) from η_B's surface at $\phi = 0.99$.

At periastron, there is almost a complete collapse of the apex of the WWC region in the simulation (row d of Fig. 3). The dense wind of η_A directly between the stars comes within $\sim$1.5 $R_{\star,\eta_B}$ of η_B's surface. η_B can only effectively drive a wind in directions away from η_A. Thus, only regions downstream where η_B's wind collides with the highly distorted spiral leading arm of the dense WWC zone are shock-heated to high T (yellow areas in second column of Fig. 3, row d). However, these regions have very low densities and volumes and are enshrouded by dense primary wind.

The equations in Appendix A2 predict that η_B should not be able to drive a wind along the line of centres at periastron due to the strong RI by η_A. In our SPH simulations, however, we launch the η_B wind at a value of twice the local sound speed (see Appendix A1). This, combined with the large transverse velocity of the stars at periastron, produces enough of an η_B wind to create a ram pressure balance at periastron in our simulations. In the absence of other forces (e.g. radiative braking), a full WWC collapse should occur along the line of centres at periastron.

The disappearance of the hot, inner WWC zone (i.e. the total cooling-transition phase) lasts $\sim$2.5 months ($\phi \approx 0.983 - 1.022$) in the simulation of Fig. 3. While the η_B wind speed at $\phi = 1.01$ is enough to restore a WWC at a few $R_\star$ above η_B's surface (row e of Fig. 3), it is not until $\phi \approx 1.02$ that η_B moves far enough from η_A that the hot, inner conical shock can start to be fully restored (Fig. 3, row f). Therefore, the hottest plasma near the WWC apex responsible for the observed X-ray emission is absent from $\phi \approx 0.983 - 1.022$. The pre-shock speed of η_A's wind along the line of centres is also slightly reduced by $\sim$30$-$40 km s^{-1} just after periastron ($\phi \sim 1.01 - 1.03$) due to the rapid orbital motion.

Figs 4 and 5 show that even with lowered η_A mass-loss rates, a cooling-transition phase occurs during periastron passage in the post-shock η_B wind located near the WWC apex. Although the details are somewhat different, the overall behaviour is the same as described above. In each case, η_A's wind penetrates deep into the acceleration zone of η_B's wind and comes very close to the star at periastron. The key point is that the lower the value of $\dot{M}_{\eta_A}$, the later the start of the cooling-transition phase and the earlier the recovery of the hottest X-ray emitting gas. In the Case B (Case C) simulation, the switch to the radiative-cooling regime occurs at $\phi \approx 0.987$ (0.991), with the hot η_B-shock apex fully recovering by $\phi \approx 1.018$ (1.014). The cause of this dependence on $\dot{M}_{\eta_A}$ is the decreased wind momentum of η_A relative to that of η_B, which places the CD farther from η_B and allows its wind to obtain larger pre-shock velocities and lower post-shock densities. This increases the value of χ since $\chi \propto v_{\mathrm{wind}}^4$ and decreases the importance of radiative cooling in η_B's wind around periastron.

The results of our 3D simulations are quite different from those of P11. The analysis in Appendix A2 can be used to help understand why. First, while the wind of η_B in our simulations is parametrized using a $\beta = 1$ velocity law, P11 use standard CAK parameters for η_B that are more consistent with $\beta \approx 0.8$. Our simulations also use
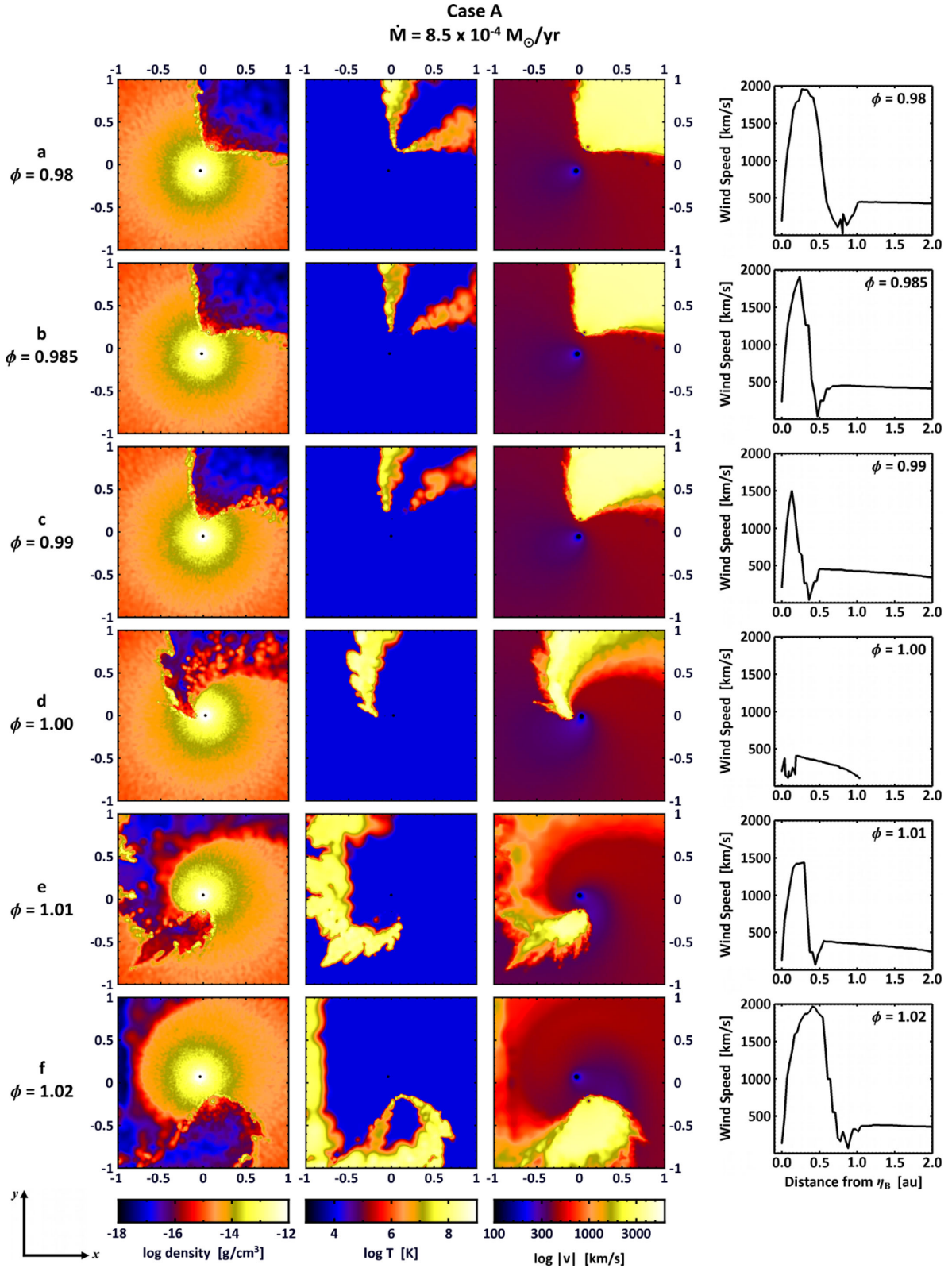
Figure 3. First three columns: Log density, temperature and total wind speed (left to right, respectively, cgs units) in the orbital plane at phases $\phi = 0.98, 0.985, 0.99, 1.00, 1.01$ and 1.02 (rows) from the very small domain 3D SPH simulation of η Car assuming $\dot{M}_{\eta_A} = 8.5 \times 10^{-4}\,\mathrm{M_\odot\,yr^{-1}}$ (Case A). All plots show the inner $\pm 1a$ region. Axis tick marks correspond to an increment of $0.1a \approx 1.54$ au. Rightmost column: line plots of the total wind speed ($\sqrt{v_x^2 + v_y^2 + v_z^2}$) along the line of centres between η_B and η_A from the simulation at each phase. Distance is measured from the surface of η_B in au. Note that all line plots extend only to $r = 2$ au from η_B in order to emphasize the WWC and pre-shock wind speeds. The stellar radius of η_B is $\mathrm{R}_{\star,\eta_B} \approx 0.14$ au.
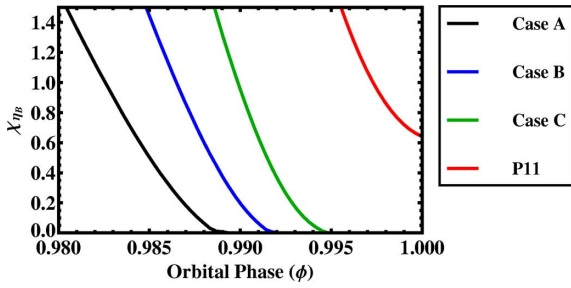
Figure 4. Cooling parameter χ in η_B's wind as a function of orbital phase ϕ assuming the simulation parameters in Table 1 (Cases A–C) and P11. The pre-shock wind speeds are computed using equations (A15)–(A19).

a slightly larger $R_\star$ for η_B ($30\,\mathrm{R}_\odot$ versus $20\,\mathrm{R}_\odot$). As illustrated in Fig. 6(a), even without RI, larger $R_\star$ and β lead to substantially lower η_B wind speeds at distances $\lesssim 1.5$ au from η_B. For our adopted $R_\star$, a $\beta = 1/2$ would be required to roughly match the η_B wind-velocity profile used by P11. However, simply reducing $R_\star$ would also result in a wind-velocity law that closely matches that of P11. Thus, the assumed $R_\star$ of η_B can have as much of an influence on the overall wind-velocity profile as the β index.

Inclusion of the velocity-altering effects of RI makes our pre-shock η_B wind speeds even lower compared to those of P11. Setting $\beta = 0.8$ in equation (A4) and substituting this into equation (A12), we can numerically integrate equation (A12) using the simulation parameters of P11. We can then compare the results to those for the parameters in Table 1. To allow for a more direct comparison with P11, we investigate here parameters for our Case B simulation with $\dot{M}_{\eta_A} = 4.8 \times 10^{-4}\,\mathrm{M}_\odot\,\mathrm{yr}^{-1}$ and $L_{\eta_B} = 3.3 \times 10^5\,\mathrm{L}_\odot$.

Fig. 6(b) shows the results for several D corresponding to $\phi = 0.5$, 0.96, 0.98 and 1.0. At apastron, the difference between our expected total pre-shock η_B wind speed and that using the parameters of P11 is relatively small, $\sim 100\,\mathrm{km\,s}^{-1}$. This is true for most of the orbit. However, the difference between the two models becomes much more pronounced as periastron is approached. At $\phi = 0.96$, our pre-shock η_B wind speed is $\sim 440\,\mathrm{km\,s}^{-1}$ lower than that of P11, while at $\phi = 0.98$, it is $\sim 815\,\mathrm{km\,s}^{-1}$ lower. The largest, most important difference occurs at periastron, where for our model parameters η_B is unable to drive a wind along the line of centres. η_B can, however, drive a wind to a rather large pre-shock velocity of $\sim 1920\,\mathrm{km\,s}^{-1}$ when using the parameters of P11.

P11 speculated that an increase in the wind velocities when moving into periastron helped stabilize the WWC in their 3D simulations and prevented a collapse. While this may be true, we find that the $R_\star$ and wind-velocity law assumed for η_B also have a big influence on
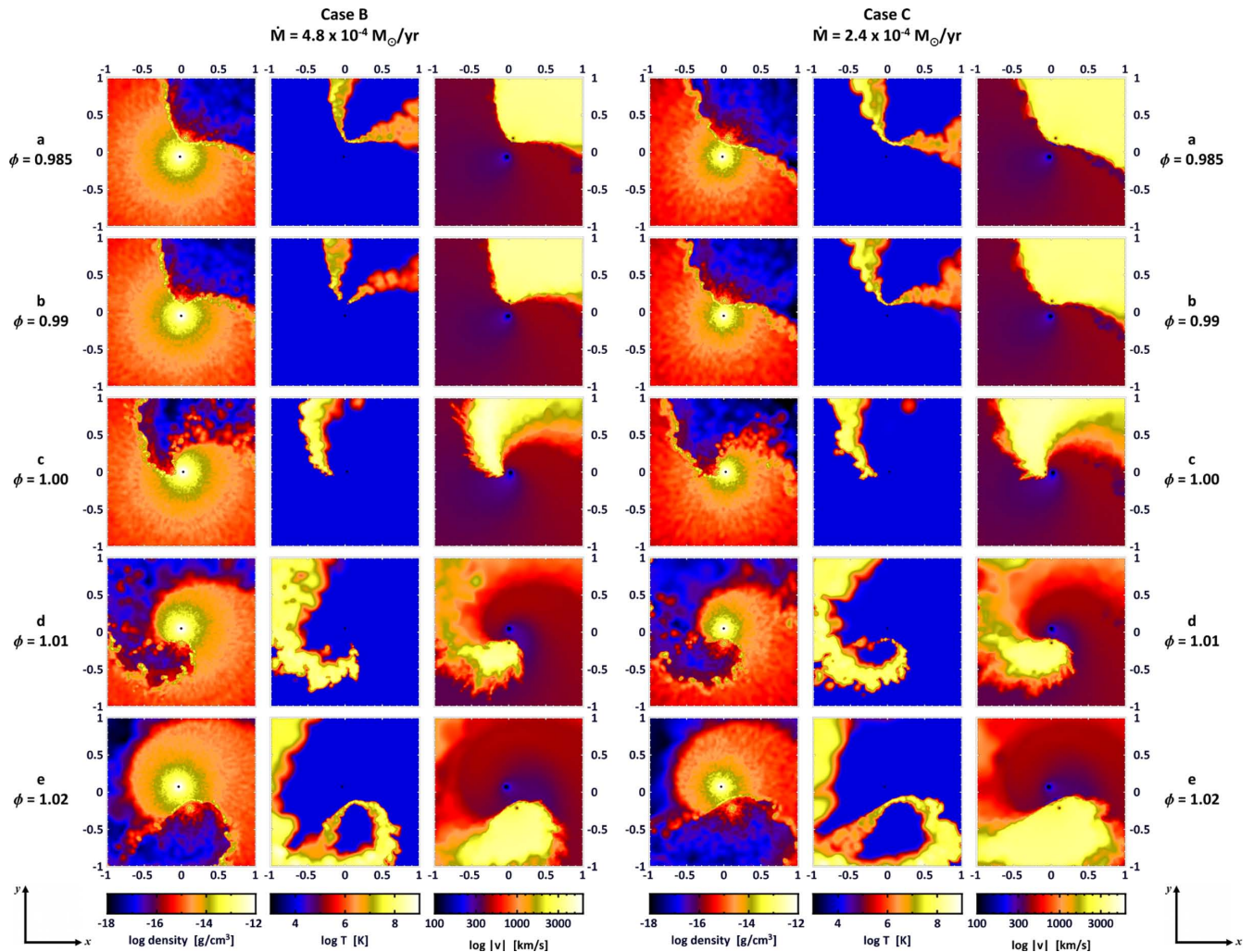
Figure 5. Same as the first three columns of Fig. 3, but for simulation Cases B (left three columns) and C (right three columns).
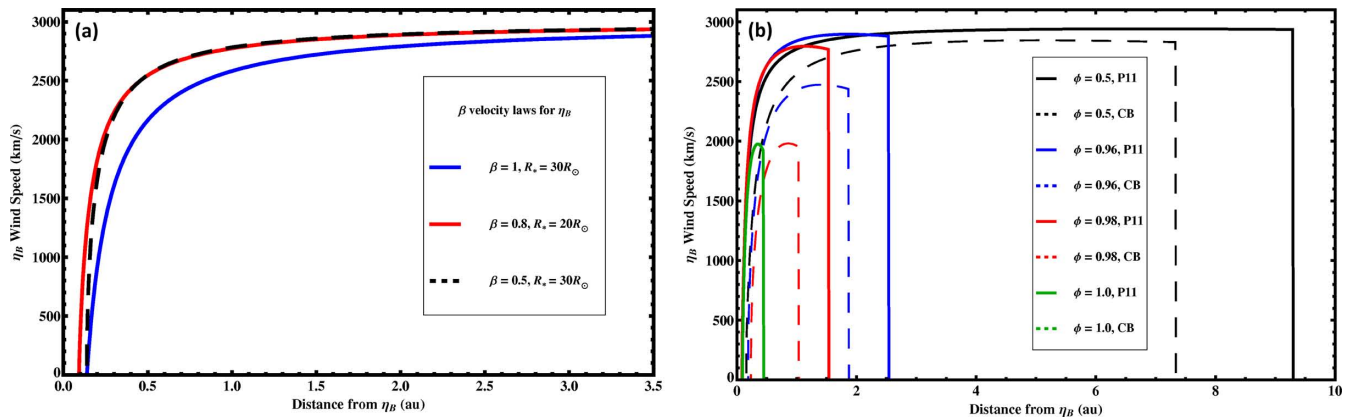
Figure 6. $\eta_{\rm B}$ wind speed along the line of centres as a function of distance from $\eta_{\rm B}$. Left panel: standard β-wind-velocity laws computed for the combinations of β and $R_\star$ that correspond to the $\eta_{\rm B}$ parameters of Table 1 (blue) and P11 (red). Included is the velocity profile for $\beta = 1/2$ and $R_\star = 30\,{\rm R}_\odot$ (dashed black line) that also roughly matches the velocity profile of $\eta_{\rm B}$ used by P11. Right panel: total $\eta_{\rm B}$ wind speed $v_{2,\,\rm tot}$ via equations (A15)–(A19), using the parameters in Table 1 with $\dot{M}_{\eta_{\rm A}} = 4.8 \times 10^{-4}\,{\rm M}_\odot\,{\rm yr}^{-1}$, $q = 15.22$ (the Case B simulation, dashed lines) and the simulation parameters of P11 (solid lines), for binary separations D corresponding to $\phi = 0.5$ (black), 0.96 (blue), 0.98 (red) and 1.00 (green). Each curve is truncated at the radius of ram pressure balance $r_{\rm b}$ given by equation (A19). There is no stable balance at $\phi = 1$ using the Case B parameters, implying a collapse of the apex of the WWC region.

determining whether there will be a cooling-transition phase in $\eta_{\rm B}$'s post-shock wind around periastron. The larger $R_\star$ and β used in our simulations lead to a significant reduction in the pre-shock $\eta_{\rm B}$ wind speed, which results in strong, rapid cooling of the post-shock $\eta_{\rm B}$ gas around periastron. Using the parameters of P11, we compute a $\chi < 1$ in the post-shock $\eta_{\rm B}$ wind only between $\phi \approx 0.997$ and 1.003 (Fig. 4), and a minimum value of $\chi \approx 0.64$ at periastron, implying that the reduction in $\eta_{\rm B}$'s wind speed by $\eta_{\rm A}$ is insufficient to cause $\eta_{\rm B}$'s wind to switch strongly to the radiative-cooling regime. This helps explain the absence of a WWC collapse in the 3D simulations of P11.

While radiative forces and inhibition are important factors that help determine whether a cooling-transition phase and WWC collapse occur in η Car at periastron, we agree with P11 that the key factor is radiative cooling. Earlier 3D SPH simulations of η Car that launched the stellar winds at their terminal speed and were isothermal (Okazaki et al. 2008) or adiabatic (M12; Madura & Groh 2012) did not show any cooling-transition phase or WWC collapse. Investigating further, we performed two very small domain ($r = 1.5a$) 3D SPH simulations with $\dot{M}_{\eta_{\rm A}} = 8.5 \times 10^{-4}\,{\rm M}_\odot\,{\rm yr}^{-1}$, focusing on phases around periastron. One simulation includes $\beta = 1$ velocity laws, RI effects and assumes adiabatic cooling, while the second simulation includes radiative cooling, but no radiative forces or inhibition (i.e. the winds are launched at terminal speed).

We find that a cooling-transition phase *only* occurs in the radiative cooling simulation (left-hand panel of Fig. 7). However, because the winds are launched at terminal speed and there is no RI, the pre-shock $\eta_{\rm B}$ wind speeds are much higher and the cooling transition occurs over a much narrower range of phases ($\phi \approx 0.998$–1.002). In the adiabatic simulation, the hot apex of the $\eta_{\rm B}$ shock survives throughout the entire simulation and there is no cooling transition phase (Fig. 7, right-hand panel). Due to the twisted WWC zone and embedding of $\eta_{\rm B}$ in $\eta_{\rm A}$'s dense wind at late phases ($\phi \approx 0.995$), the most distant parts of the trailing arm of the WWC region still cool to $T \lesssim 10^6$ K, producing a temperature asymmetry between the leading and trailing arms in the outermost post-shock $\eta_{\rm B}$ wind. This, however, is not a collapse or radiative cooling/inhibition effect, but a consequence of rapid orbital motion in a highly eccentric orbit. Our results thus suggest that radiative cooling of the post-shock $\eta_{\rm B}$ wind
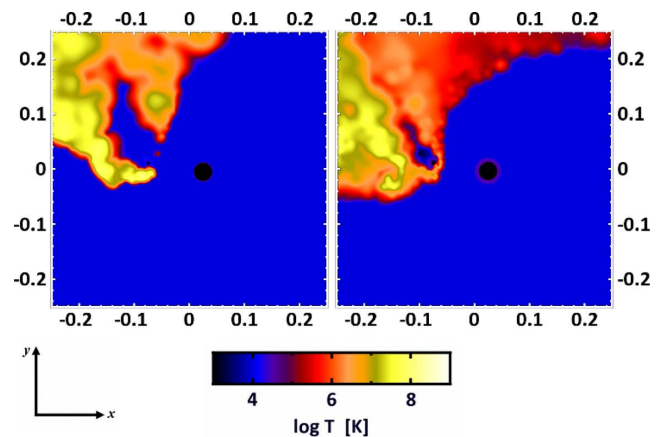
Figure 7. Slices showing log temperature in the orbital plane at periastron from very small domain SPH simulations of η Car that use radiative cooling with the stellar winds launched at terminal speed (left-hand panel) and adiabatic cooling with $\beta = 1$ velocity-law winds and RI effects (right-hand panel). All plots show the inner $\pm 0.25a$ region.

is primarily responsible for any disappearance of hot X-ray emitting gas and/or WWC collapse in η Car during periastron passage. Radiative forces (e.g. $\beta = 1$ wind-velocity laws and inhibition) assist the cooling transition by helping slow $\eta_{\rm B}$'s wind prior to periastron, allowing the transition to start earlier and last longer compared to a situation in which the winds collide at near their terminal speeds, since $\chi \propto v_{\rm wind}^4$.

3.1.2 The influence of radiative braking

Our antigravity approach does not currently permit the implementation of radiative braking in the SPH simulations (for details see Gayley et al. 1997; Russell 2013). P09 demonstrated that $\eta_{\rm A}$ cannot brake $\eta_{\rm B}$'s wind, irrespective of what CAK parameters they used. Kashi & Soker (2009) claim there should be a normal ram balance between η Car's colliding winds at periastron and no radiative braking. However, P09 found that $\eta_{\rm B}$ can radiatively brake $\eta_{\rm A}$'s wind if it comes extremely close to the stellar surface, e.g. within

$\sim 80\,R_\odot$ (~ 0.37 au) of η_B. While under normal circumstances this means radiative braking would not occur before the two winds collide, it implies that radiative braking may be able to prevent the collision of dense η_A wind material with the surface of η_B at periastron.

The two conditions required for radiative braking can be summarized as (1) $\hat{d} \equiv d/d_{rb} > 1$ and (2) $\hat{P} \equiv P_{12}/P_{rb} > \hat{d}^2$, where $d \equiv D/R_2$ is the binary separation scaled by the secondary's stellar radius, $P_{12} \equiv (\dot{M}_1 v_1)/(\dot{M}_2 v_2)$ is the primary/secondary wind momentum ratio, $P_{rb} = 4\beta^\beta d_{rb}^2/(2 + \beta)^{2+\beta}$ for a velocity law with index β, and d_{rb} is found by solving the transcendental expression $d_{rb} = 1 + (d_{rb}/\zeta)^{(1-\alpha)/(1+\alpha)}$ for standard CAK power index α and constant ζ given by

$$\zeta = \frac{(L_2/L_1)^{1/(1-\alpha)}}{(1+\alpha)\alpha^{\alpha/(1-\alpha)}} \frac{2\,GM_1}{R_2 v_{\infty,1}^2} \quad \text{(Gayley 1995).} \qquad (1)$$

Condition (1) implies that a photospheric collision of star 1's wind with the surface of star 2 is prevented, while condition (2) implies that there is no 'normal' ram pressure balance.

Using the values in Table 1 with $\dot{M}_{\eta_A} = 8.5 \times 10^{-4}\,M_\odot\,\text{yr}^{-1}$, $q = 22.28$ and $\alpha = 2/3$, we see that condition (1) is satisfied throughout η Car's 5.54 yr orbit, which means that η_B's radiation is capable of preventing η_A's wind from impacting η_B, even at periastron. For most of the orbit, condition (2) is *not* satisfied and there is no radiative braking. However, for $0.99 \lesssim \phi \lesssim 1.01$, Equations (A15) through (A19) indicate that there is no normal ram pressure balance along the line of centres because of the RI of η_B's wind by η_A. If there is indeed no ram balance between $\phi = 0.99$ and 1.01, then both (1) and (2) are satisfied and there *will* be radiative braking of η_A's wind by η_B. This is consistent with the findings of P09. The reason Kashi & Soker (2009) determined that there would be no radiative braking at periastron is because they neglected the effects of RI and orbital motion and assumed that P_{12} is constant throughout the orbital cycle. As shown in Appendix A2, η Car's wind momentum ratio *is not constant* and depends strongly on the binary separation. While our analysis shows that radiative braking may occur between $\phi = 0.99$ and 1.01 in η Car, this does not significantly affect our results or conclusions since the main effect of such braking would be the prevention of the collision of dense primary wind with η_B's surface at periastron if/when the WWC zone 'collapses'. Radiative braking, however, has important implications for models in which η_B is assumed to accrete wind material from η_A at periastron, such as that proposed by Kashi & Soker (2009), since the braking could likely prevent such accretion.

3.2 Large-domain simulations

Figs 8 and 9 show, respectively, the density and temperature in the orbital plane at five select phases from the $r = 100a$ simulations. Results for slices in the xz and yz planes are in Appendix B2, while movies of the simulations are available in the online version of this paper (see Supporting Information).

The dense arcs and shells of η_A wind visible in the outer ($>20a$) regions of Fig. 8 indicate that the binary has already undergone multiple orbits. Narrow cavities carved by η_B in η_A's wind during each periastron passage also exist on the back (periastron) side of the system. The width of these cavities increases with decreasing $\dot{M}_{\eta_A}$ due to the change in the wind momentum balance. The larger cavities in Cases B and C also contain hotter η_B wind material and extend farther in the $+y$ direction (Fig. 9).

Bordering the wind cavities on the periastron side of the system are compressed, high-density shells of η_A wind that form as a re-

sult of the rapid WWC. These shells flow outward at $v \gtrsim v_{\infty,\eta_A}$, accelerated by the collision with η_B's higher velocity wind. The speed of the shells increases with decreasing $\dot{M}_{\eta_A}$, while the density and thickness of the shells decrease with $\dot{M}_{\eta_A}$. The innermost shell closest to the stars has the highest outward velocity due to the more recent collision with η_B's wind. The outer shells move slower, at approximately v_{∞,η_A}, due to the gradual increase in the amount of swept-up η_A-wind mass in each shell.

The counter-clockwise direction of orbital motion in the xy plane also produces a noticeable difference in the thickness of the shells and width of the η_B wind cavities located in the $+y$ and $-y$ directions (Fig. 8). The shells of η_A wind that lie in the $-y$ direction are thinner and more compressed, while the η_B wind cavities are wider. This size difference becomes more apparent as the value of $\dot{M}_{\eta_A}$ is lowered, with Case C having the thinnest shells and widest cavities in the $-y$ direction.

Following periastron, η_B returns to the apastron side of the system, its wind colliding with the η_A wind that flows in the $+x$, $-y$ direction. At $\phi \approx 3.1$, the arms of the WWC region become extremely distorted by orbital motion and the leading arm collides with the old trailing arm from before periastron, forming another dense, compressed shell of η_A wind that flows in the $+x$ and $-y$ directions (rows d and e of Fig. 8). The overall stability of this expanding shell depends on the shock thickness (Vishniac 1994; Wünsch et al. 2010; P11). Portions of the shell moving in the $-y$ direction appear to be the most stable due to the large amount of η_A wind that borders it in this direction. The shells are also more stable and remain intact longer the higher the value of $\dot{M}_{\eta_A}$. In Case A, the upper part of the shell expanding in the $+x$, $+y$ direction does not start to fragment until $\phi \approx 3.34$. In Case C, the shell is completely disrupted in the $+x$, $+y$ direction by $\phi \approx 3.1$, the wind of η_B having ploughed through it, causing it to separate from the leading arm of the WWC zone (see rows d and e of Fig. 8, and row e of Figs 1 and B1). This separation produces a pair of dense 'arcs' of η_A wind on the apastron side of the system. Multiple pairs of arcs, formed during previous orbital cycles, are visible in Fig. 8. They are also quite spatially extended; by the time the system is back at periastron the arcs formed during the previous periastron are up to $80a \approx 1235$ au from the central stars.

As the dense arcs flow outward, the wind of η_B collides with and propels them at a speed slightly greater than v_{∞,η_A} into the low-density cavity created during the previous orbital cycle (Fig. 8). This produces another shock located $\sim 20a$ from the central stars (along the $+x$ axis at $\phi = 0.5$) that heats the outer η_B wind to $T > 10^7$ K (Fig. 9). The arcs also expand as they move outward. Since they are bordered on both sides by low-density, high-speed η_B wind, the arcs eventually become unstable and fragment, mixing with the surrounding η_B wind material. The lower the value of $\dot{M}_{\eta_A}$, the thinner and less dense the expanding arcs, and the sooner they fragment and mix with the η_B wind. An example of this fragmentation and mixing can be seen in the outermost arc/shell located at the bottom of the panels for Case C in Fig. 8.

4 IMPLICATIONS FOR VARIOUS OBSERVATIONAL DIAGNOSTICS

The SPH simulations show that for the range of explored values, a factor of 2 or more decrease in $\dot{M}_{\eta_A}$ alters significantly the time-dependent 3D density, temperature and velocity structure of η Car's spatially extended primary wind and WWC zones. Therefore, any such drop in $\dot{M}_{\eta_A}$ should result in detectable differences in numerous
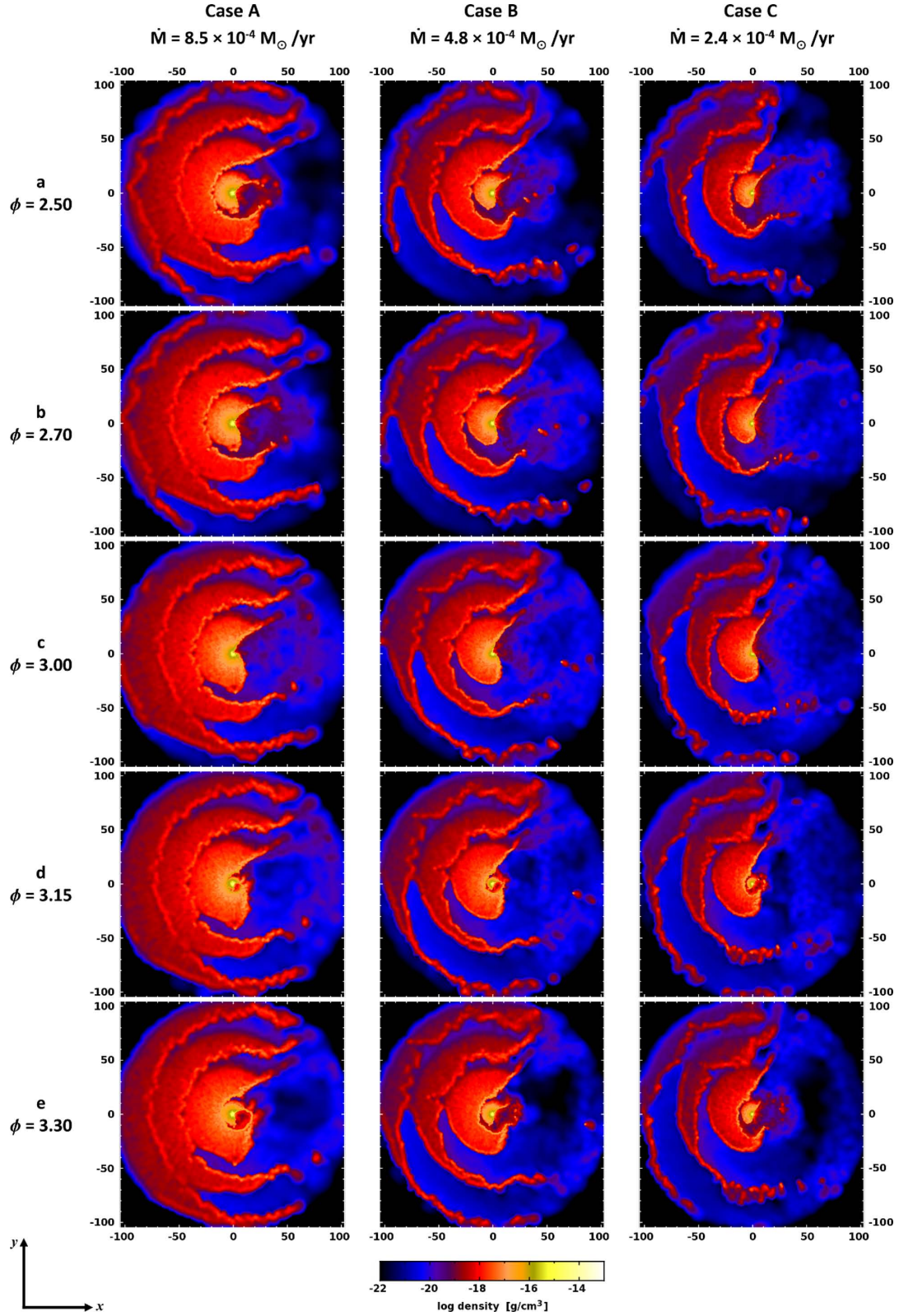
Figure 8. Slices in the orbital plane from the large-domain 3D SPH simulations of η Car (Table 1) at orbital phases $\phi = 2.5$ (apastron), 2.7, 3.0 (periastron), 3.15 and 3.30 (rows, top to bottom). Columns correspond to the three assumed η_A mass-loss rates. Colour shows log density in cgs units. The spherical computational domain size is $r = 100a \approx 1545$ au ≈ 0.67 arcsec ($D = 2.3$ kpc). Axis tick marks correspond to an increment of $10a \approx 155$ au ≈ 0.067 arcsec. The orbital motion of the stars is counter-clockwise. η_A is to the left and η_B is to the right at apastron.
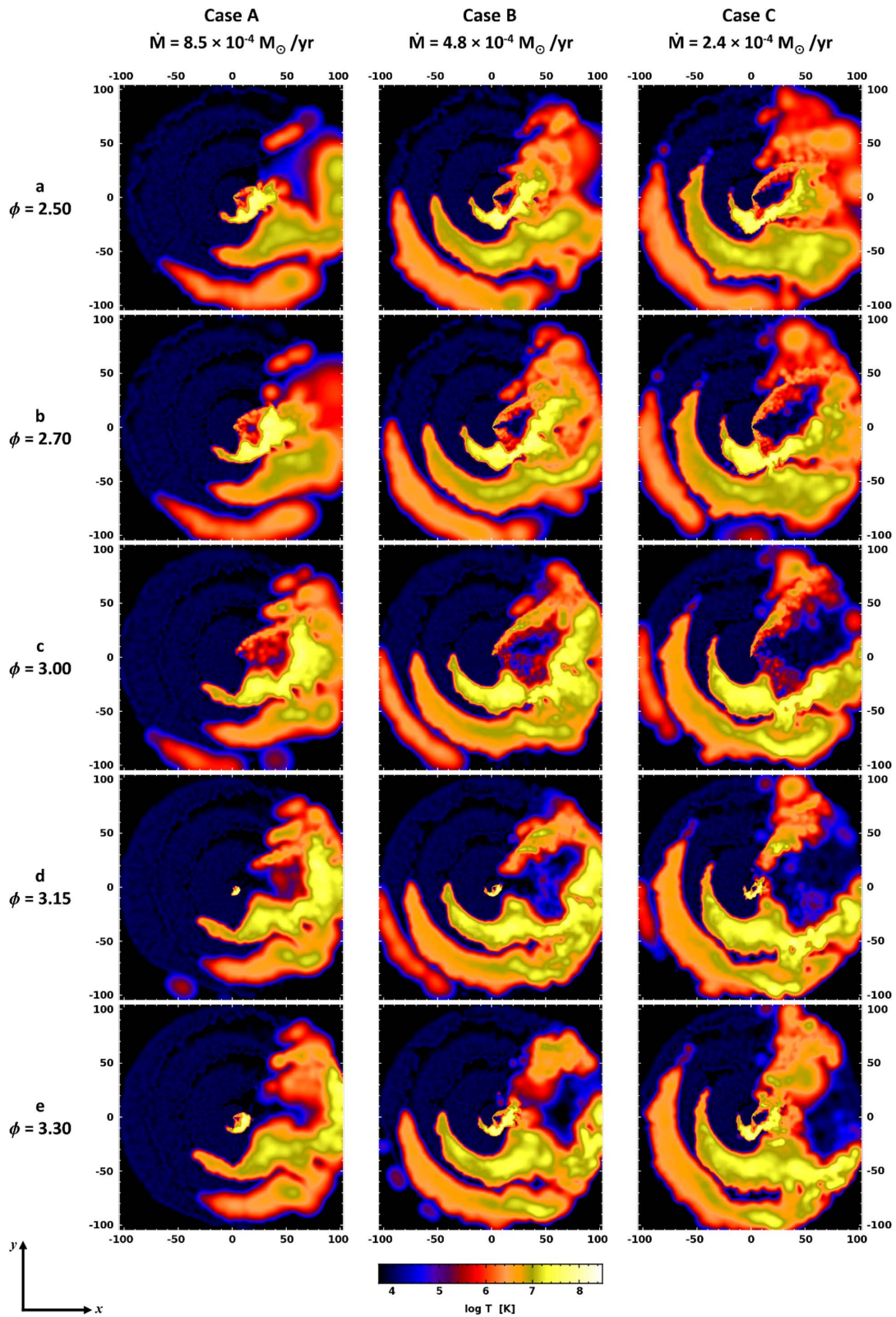
Figure 9. Same as Fig. 8, but with colour showing log temperature.

observational diagnostics (compared to earlier cycles). Guided by the SPH results, we qualitatively discuss below some of the expected changes and suggest observations to perform in order to further test whether $\dot{M}_{\eta_A}$ is decreasing. We focus here on changes that are

likely to be most important. Detailed quantitative modelling of the vast array of multiwavelength observations of η Car using the 3D simulations is beyond the scope of this paper and is left for future work.

4.1 Effects on the amount of material in line of sight

M12 tightly constrained, for the first time, the 3D orientation of η Car's binary orbit using a 3D dynamical model for the broad, spatially extended [Fe III] emission observed by the *HST*/STIS (Gull et al. 2009). M12 find that the observer's line of sight (LOS) has an argument of periapsis $\omega \approx 240°$ to $285°$, with the binary orbital axis closely aligned with the Homunculus polar axis at an inclination $i \approx 130°$ to $145°$ and position angle on the sky $PA_z \approx 302°$ to $327°$, implying that apastron is on the observer's side of the system and that η_B orbits clockwise on the sky (see rightmost panel of Fig. 10). This orientation and clockwise motion of η_B are consistent with all known observations of η Car to date (see the discussion in M12 and Madura & Groh 2012).

Assuming the orbital orientation in Fig. 10, a factor of 2 or more drop in $\dot{M}_{\eta_A}$, for the range of explored values, would change significantly the time-variable amount of material in LOS to the observer. For example, if $\dot{M}_{\eta_A} = 8.5 \times 10^{-4}$ M$_\odot$ yr^{-1}, then the half-opening angle of the WWC zone ($\approx 55°$) is quite close in value to the inclination angle of the binary away from the observer ($\approx 48°$). Therefore, the observer's LOS lies very near the edge of the WWC cavity (see bottom-left panel of Fig. 10), with portions of the dense, outer interacting winds passing through our LOS. The column density is thus expected to be greater for sightlines to the observer than to most other parts of the system, especially towards the Weigelt blobs, which lie in/near the orbital plane (Davidson et al. 1997; Smith et al. 2004a) surrounded by the low-density wind from η_B.

As discussed in G12a, this may resolve the long standing puzzle of why our direct view of the central star suffers more extinction than the Weigelt blobs located only 0.3 arcsec away (Davidson et al. 1995; H01). Furthermore, as suggested by Smith (2010) and G12a, dust formation in the densest parts of the outer interacting winds might explain the peculiar 'coronograph' described by H06.

A decrease of less than a factor of 2 in $\dot{M}_{\eta_A}$ is enough to increase the opening angle of the WWC cavity and cause the observer's LOS to no longer intersect portions of the WWC region (bottom row of Fig. 10). For $\dot{M}_{\eta_A} = 8.5 \times 10^{-4}$ M$_\odot$ yr^{-1}, the difference in angle between the observer's LOS and the dense wall of the WWC zone is $\sim 5°$–$10°$, whereas for 4.8×10^{-4} M$_\odot$ yr^{-1}, the difference is $\sim 15°$–$20°$. Fig. 10 shows that the lower the value of $\dot{M}_{\eta_A}$, the more the observer's LOS samples only low-density η_B wind. The column density in LOS to most other directions on the apastron side of the system, e.g. towards the Weigelt blobs, is not nearly as strongly affected by decreases in $\dot{M}_{\eta_A}$. Interestingly, since 1998, the Weigelt blobs have not brightened significantly, even though the central source has brightened by one stellar magnitude in the optical (Davidson 2005; Gull et al. 2009). A change in η caused by a slight decrease in $\dot{M}_{\eta_A}$ might explain this since the larger opening angle would decrease the amount of extinction in LOS to the observer, causing an apparent increase in the brightness of the central source while leaving the Weigelt blobs unaffected due to their location in the orbital plane. Additional observations are needed in order to determine that such a change in opening angle occurred and is due
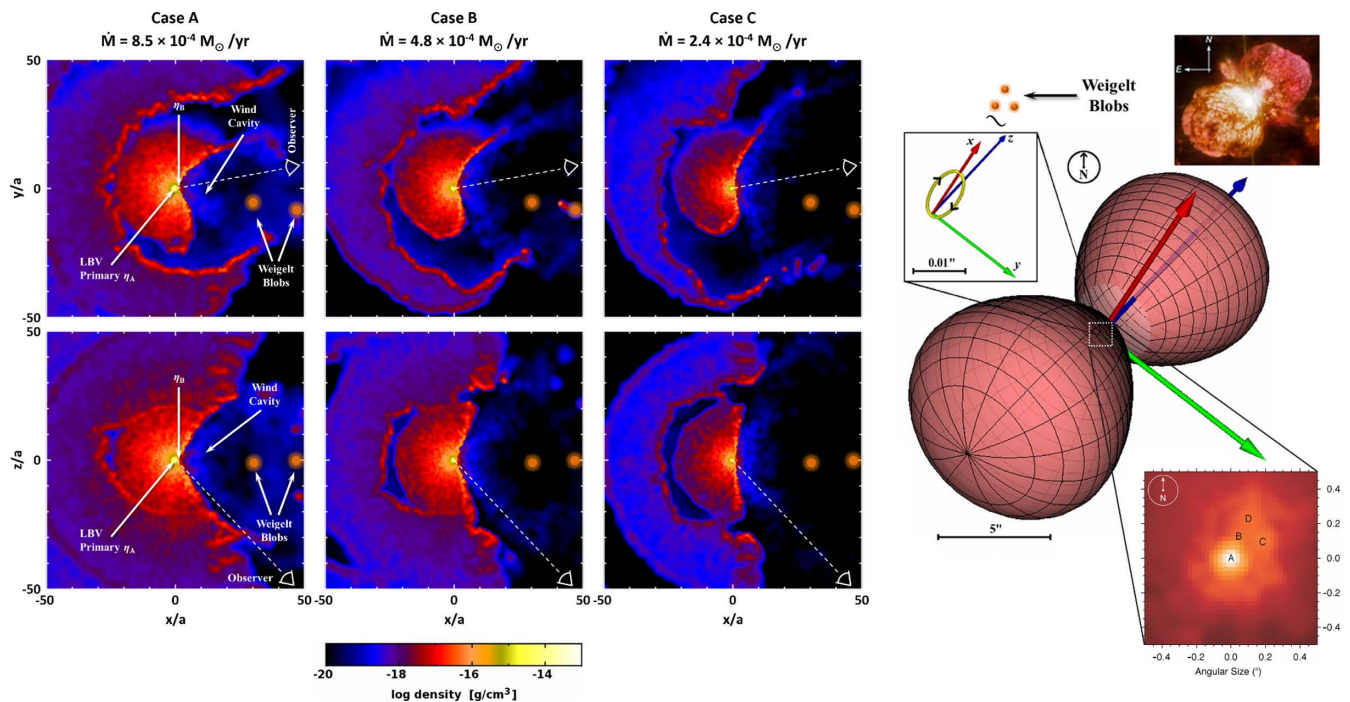
Figure 10. Geometry and location of the colliding stellar winds relative to the observer and the central stars, and incorporating the apparent position of two Weigelt blobs, at an orbital phase near apastron. Top row of three panels: slices showing log density in the orbital plane from the 3D SPH simulations for the three different values of $\dot{M}_{\eta_A}$. The locations of the stars, η_B wind cavity and Weigelt blobs are indicated by arrows. The dashed line and eye indicate the projected line of sight to the observer. Axis tick marks correspond to an increment of $10a \approx 155$ au ≈ 0.067 arcsec. Bottom row of three panels: same as top row, but for slices in the *xz* plane. Far right panel: illustration of η Car's binary orbit (upper left inset, yellow) on the sky relative to the Homunculus nebula assuming the binary orientation derived by M12 ($i = 138°$, $\omega = 263°$, and $PA_z = 317°$). The +*z* orbital axis (blue) is closely aligned with the Homunculus polar axis in 3D. η_B orbits clockwise on the sky relative to η_A (black arrows in inset) and apastron is on the observer's side of the system. The semimajor (+*x*) and semiminor (+*y*) axes are indicated by the red and green arrows, respectively, and North is up. Included for reference are insets showing an *HST* WFPC2 image of the Homunculus (top right, Credit: NASA, ESA and the Hubble SM4 ERO Team) and a 1 arcsec × 1 arcsec *HST*/ACS *F550M* image (lower right) showing the location of the central stars (A) and the bright Weigelt blobs (B, C, D).

solely to a decrease in $\dot{M}_{\eta_A}$ and not, say, an increase in the $\dot{M}$ and/or v_∞ of η_B.

4.2 Effects on X-rays

4.2.1 Column density and the X-ray minimum

Changes to the wind momentum ratio will change the WWC opening angle and alter the distribution of the shock-heated gas, which should have observable consequences in the X-ray band. An increase in the WWC opening angle of $\sim 10°$–$20°$ should cause a delay of ~ 20–40 d in the observed sharp rise in column density (N_H, Hamaguchi et al. 2007) that occurs prior to periastron. The decrease in N_H seen after periastron should also begin ~ 20–40 d earlier. When combined with the reduced duration of the cooling-transition phase of η_B's post-shock wind, the net result should be a shorter X-ray minimum during periastron passage for lower values of $\dot{M}_{\eta_A}$. This simple analysis reveals that for the range of explored $\dot{M}_{\eta_A}$, the total X-ray minimum should be ~ 40–80 d shorter than that of a previous orbital cycle.[1]

One mystery regarding η Car's X-ray light curve is why no significant change was observed in 2009 just prior to the X-ray minimum. Based on the simulations, the start of the 2009 minimum should have also been delayed if $\dot{M}_{\eta_A}$ dropped by a factor of 2 or more. Yet, only the timing of the X-ray recovery changed. One might argue that this is evidence of a sudden significant (e.g. $\gtrsim$ factor of 2) change in $\dot{M}_{\eta_A}$ during the 2009 event, with the apparent observed decrease in X-ray hardness between 2004 and 2009 due to a smaller, gradual decrease in $\dot{M}_{\eta_A}$ that was not enough to change the timing of the start of the 2009 X-ray minimum. Since the recovery from the 2009 event, the 3–10 keV X-ray flux has been ~ 20 per cent below the level seen in the previous two cycles (Corcoran 2013). A decrease in flux outside of the minimum is expected if $\dot{M}_{\eta_A}$ decreased. However, a drop in $\dot{M}_{\eta_A}$ by a factor of 2 should result in a flux decrease of about a factor of 2 (Russell 2013). The implication is that, if $\dot{M}_{\eta_A}$ decreased around the 2009 event, either (1) the change was by a factor $\lesssim 2$ or (2) the decrease occurred suddenly and by a factor $\gtrsim 2$, but immediately after the 2009 event, $\dot{M}_{\eta_A}$ quickly returned to its 'normal' value, resulting in an overall X-ray flux decrease of ~ 20 per cent at times away from periastron.

Furthermore, the 2003 X-ray minimum did not start earlier, which seems to rule out any large change in $\dot{M}_{\eta_A}$ prior to mid-2003. The first significant sign of a possible recent change in η Car was the early recovery of the 2009 X-ray minimum. Up until that point, most differences in η Car were viewed as typical cycle-to-cycle variations and/or caused by the continuous decrease in the amount of circumstellar extinction in LOS (Martin, Davidson & Koppelman 2006a; Smith 2010). Detailed analysis by C10 of η Car's X-rays over the last three cycles revealed later that the X-ray hardness and flux had decreased slightly between 2004 and 2009. The X-ray spectrum was also softer 100 d after the 2009 minimum than it was 100 d after the 2003.5 minimum, with the $E > 3$ keV flux lower as well. Moreover, it now appears that a high $\dot{M}_{\eta_A}$ of $\sim 10^{-3}$ M$_\odot$ yr^{-1} is necessary in 3D hydrodynamical simulations to reproduce the extended *RXTE* X-ray minima in 1998 and 2003.5, and the X-ray flux level observed between events (Russell 2013; Russell et al., in preparation). Therefore, the X-ray data suggest that if there was a recent large decrease in $\dot{M}_{\eta_A}$, it occurred sometime around/after

2004. The lack of any change in the He II λ4686 emission before the 2009 event supports this (see Section 4.3).

If the extended X-ray minima of 1998 and 2003.5 were the result of a long cooling-transition phase, perhaps the shorter minimum in 2009 was the result of some change in the effectiveness of radiative cooling in η_B's post-shock wind. A modest decrease in $\dot{M}_{\eta_A}$ of ~ 20 per cent (or a bit more) might have moved the WWC apex far enough from η_B to decrease the effectiveness of radiative cooling, but a factor of 2–4 drop does not appear to be fully consistent with the current X-ray data. On the other hand, if $\dot{M}_{\eta_A}$ is indeed decreasing and continues to do so, the 2014 X-ray minimum should be even shorter than that of 2009. Continued decrease of $\dot{M}_{\eta_A}$ would eventually lead to an even shorter X-ray minimum.

4.2.2 The CCE component

During the deep minimum, the X-ray emission is dominated by the 'Central Constant Emission' (CCE) component (Hamaguchi et al. 2007, hereafter H07). *Chandra* data indicate the CCE is pointlike ($\lesssim 2000$ au for $D = 2.3$ kpc). The X-ray luminosity of and column density to the CCE component suggest that it is a stable (over the course of the deep minimum), luminous X-ray source that exists beyond the primary wind in front of the WWC apex at periastron (H07). The large-domain SPH simulations (Figs 8, 9 and B5−B8) show that, at periastron, the collision of η_B's wind with the arcs of compressed η_A wind material located on the apastron side of the system could produce significant amounts of hot ($\gtrsim 10^7$ K) gas in front of the primary at distances <2000 au in size. The simulations further show that this emission varies slowly on time-scales of months, and so this faint, hot gas is a logical candidate for the source of the CCE. Any decrease of $\dot{M}_{\eta_A}$ will propagate into the outer wind structures of η Car, affecting the thermalization of the CCE component and/or the absorption to the CCE in LOS. Measurements of the X-ray emission measure, column density in LOS and ionization state of the CCE component during η Car's next periastron in 2014 would thus be useful. When compared to the same data from the 2009 event, the 2014 observations could help confirm or rule out a recent factor of 2–4 drop in $\dot{M}_{\eta_A}$.

4.2.3 X-ray emission line profiles

X-ray emission line profiles provide important information on the temperature and density distribution of the hot, post-shock η_B gas flowing along the boundary of the WWC zone (Henley et al. 2008). They can also be used to constrain the opening angle of the WWC cavity and the orientation of the system relative to our LOS (Henley et al. 2008, P11). *Chandra* high-energy grating spectra show that strong, narrow emission lines are relatively unshifted during most of η Car's orbit. Just prior to the X-ray minimum ($\phi \approx 0.98$–0.99), the strongest lines become increasingly blueshifted and broader, reaching velocities ≈ -2000 km s^{-1} as the flow of shocked η_B wind along the trailing arm of the WWC zone swings rapidly past the observer's LOS (Henley et al. 2008; Corcoran 2011).

The small-domain simulations show that an increase in the WWC opening angle causes the hot trailing arm of the WWC zone to cross the observer's LOS (with $\omega \approx 260°$) at later orbital phases as the system approaches periastron. The observer will thus not see hot, high-velocity post-shock η_B gas until much closer to periastron. This should result in a detectable phase delay in when the X-ray lines become blueshifted and broader. The magnitude of this delay will be proportional to the increase in WWC opening angle.

---

[1] For detailed quantitative modelling of η Car's X-ray observations that support this result, see Russell (2013).

4.2.4 X-ray flaring

η Car's *RXTE* light curve also exhibits short-term rapid variations in brightness or 'flares' (Corcoran et al. 1997; Moffat & Corcoran 2009; C10). These flares become more frequent and shorter in duration as periastron is approached. Moffat & Corcoran (2009) presented a series of models for explaining the flares, their preferred model consisting of large stochastic wind clumps from η_A that enter and compress the hard X-ray-emitting WWC zone. As an alternative, they considered that the flares are the result of instabilities intrinsic to the WWC zone. P11 indicate that such instabilities, especially if combined with a clumpy LBV wind, may be a viable explanation for the X-ray flares. The SPH simulations suggest that a decrease in the value of $\dot{M}_{\eta_A}$ leads to a more unstable, clumpy WWC region. A decrease in $\dot{M}_{\eta_A}$ would therefore result in a higher flare frequency, especially as periastron is approached. The relative duration and amplitude of the flares may also change, although detailed numerical modelling is required to test this.

4.2.5 Changes to η_B's wind parameters?

An increase in the opening angle of the WWC zone combined with a shortened cooling-transition phase during periastron passage might explain the shortened duration of the 2009 X-ray minimum. However, these effects may not necessarily be a result of a drop in $\dot{M}_{\eta_A}$. A comparable increase in the $\dot{M}$ and/or v_∞ of η_B's wind would also increase the WWC opening angle. One argument against a recent increase in the v_∞ of η_B's wind is that such a change should increase the X-ray hardness at all phases. However, the X-ray hardness appears to have declined somewhat between 2004 and 2009 (C10). A significant increase in the $\dot{M}$ of η_B is harder to quantify since the densities in the post-shock η_B wind would increase, affecting the X-ray emission measure. Recent flux measures are lower compared to previous cycles, suggesting a decrease in the emission measure of the shocked η_B wind. One argument against an increase in η_B's $\dot{M}$ is that such an increase should strengthen the effectiveness of radiative cooling in the post-shock wind at phases close to periastron. One would then expect a longer cooling-transition phase that leads to a longer minimum, as opposed to the observed shorter minimum. Finally, a decrease in stellar radius or change in the velocity-law profile (e.g. β) of η_B could also allow its wind to reach higher pre-shock velocities without drastically altering v_∞, moving the WWC zone closer to η_A and again decreasing the effectiveness of radiative cooling during periastron passage. Such changes could in principle produce a shortened X-ray minimum compared to previous cycles, although the physical reasons for a sudden alteration of η_B's stellar parameters seem inexplicable. Numerical simulations investigating η_B's stellar/wind parameters are needed in order to determine if such changes can explain the X-ray observations.

4.3 The He II λ4686 emission

Somewhat related to the X-ray emission is the peculiar behaviour of the He II λ4686 emission around periastron (Steiner & Damineli 2004; Martin et al. 2006b; Mehner et al. 2011; Teodoro et al. 2012). The He II λ4686 line intensity increases suddenly by a factor of 10 just before phase 1.0 and then drops sharply to zero, after which it recovers to a second peak in intensity before declining back to zero again. A highly luminous source of He$^+$-ionizing photons with $h\nu > 54.4$ eV is required for the formation of this line. The necessary soft X-rays are thought to come from the shocked η_A wind, while

the He II λ4686 emission is hypothesized to originate in the η_A wind just before the WWC and/or in the cold, dense post-shock η_A wind (Martin et al. 2006b; Abraham & Falceta-Gonçalves 2007; Mehner et al. 2011; Teodoro et al. 2012). Earlier alternative explanations in which the He II λ4686 arises in the wind of η_B can be found in Steiner & Damineli (2004) and Soker & Behar (2006).

Mehner et al. (2011) argue that the He II emission behaved differently during the 2009 spectroscopic event and included a second intensity peak just after periastron that was not present during the 2003 event or delayed. However, Teodoro et al. (2012) claim that the two events were not drastically different. In any case, both Mehner et al. (2011) and Teodoro et al. (2012) support a scenario in which there is a WWC 'collapse' during periastron that helps explain the behaviour of the He II λ4686 line. A WWC disruption seems necessary to explain the fact that the He II behaviour is remarkably similar for both reflected spectra from the polar region of η_A and a direct view of the central stars (Stahl et al. 2005; Mehner et al. 2011).

4.3.1 Formation of the He II λ4686 emission in η Car

Before elaborating on how the He II emission should change if there is a large drop in $\dot{M}_{\eta_A}$, it is important to clarify how/where the He II emission forms in η Car, and why the equivalent width (EW) behaves the way it does around periastron (see e.g. fig. 4 of Mehner et al. 2011 or fig. 3 of Teodoro et al. 2012). Some of the ideas below have been discussed in Martin et al. (2006b); Mehner et al. (2011) and Teodoro et al. (2012), to which we refer the reader for details. However, we present several new concepts that are crucial for understanding the formation of the observed He II λ4686 emission and its dependence on $\dot{M}_{\eta_A}$.

As discussed by Martin et al. (2006b); Mehner et al. (2011) and Teodoro et al. (2012), the low-density pre-shock wind of η_B, the acceleration region of the wind of η_B and the post-shock wind of η_B can all easily be excluded as the source of the He II λ4686 emission, based simply on energy and density requirements. While it is often assumed that the He II emission arises in the dense wind of η_A, two key remaining questions are (1) why is strong He II emission only observed between $\phi \sim 0.98$ to 1.03 and (2) how/where do the required He$^+$ ions form?

According to fig. 9 of H01, for $r > 10R_{\star,\eta_A}$, helium is *neutral* in the dense wind of η_A (assuming $\dot{M}_{\eta_A} = 10^{-3}$ M$_\odot$ yr^{-1}). Therefore, under normal circumstances, there can be no He II emission for most of η Car's cycle since there is no He$^+$ near the WWC zone to be ionized. Moreover, for most of the orbit, soft X-rays formed in the WWC zone cannot penetrate the dense primary wind that lies between η_B and the small He$^+$ zone at $r < 10R_{\star,\eta_A}$. There is no other known source of photons capable of ionizing the inner η_A He$^+$ zone. One might try to argue that radiation from the WWC shocks ionizes the neutral helium in η_A's wind located near the WWC region. However, the WWC shocks are unsuitable for this since the 3000 km s^{-1} shocked wind of η_B produces mainly hard X-rays with energies above 500 eV, while the 420 km s^{-1} wind of η_A produces photons with energies of the order of a few hundred eV. Both are highly inefficient for ionizing neutral helium, and only the shocked wind of η_A is suitable for providing photons to ionize He$^+$.

The only other possible source of neutral-helium ionizing photons at times away from periastron is η_B. As noted by Nielsen et al. (2007) and Humphreys, Davidson & Koppelman (2008), during most of the binary orbit, η_B *may* photoionize neutral helium in a small region of the pre-shock η_A wind located just beyond the WWC zone (similar

to fig. 12 of Humphreys et al. 2008).[2] Neutral helium in portions of the colder, denser post-shock η_A wind would also be ionized by η_B. The He$^+$ in the dense post-shock η_A wind will very quickly recombine, producing He I emission. Some of the He$^+$ in the lower-density, pre-shock η_A wind would also recombine and create He I emission (Humphreys et al. 2008). However, we suggest that *if* η_B can photoionize neutral helium in the pre-shock wind of η_A, some of the resulting He$^+$ will be additionally ionized by soft X-rays created in the colliding η_A wind, producing a very small amount of He II λ4686 emission at times away from periastron. The amount of He II emission is likely to be small because of the lower densities in the pre-shock η_A wind near the WWC region, and because of the likely very small volume of He$^+$ created by η_B's radiation. This is consistent with the observations and explains why little to no He II λ4686 emission is detected during most of η Car's 5.54 yr cycle (Steiner & Damineli 2004; Stahl et al. 2005; Martin et al. 2006b; Mehner et al. 2011; Teodoro et al. 2012).

Earlier proposed scenarios for the He II λ4686 emission also have difficulty explaining the emission peaks observed just prior to and after periastron. Here, we present a new, simple explanation for these peaks. fig. 9 of H01 shows that He$^+$ exists in η_A's wind only between $\sim 2.4 R_{\star,\eta_A}$ and $10 R_{\star,\eta_A}$ (0.7–3 au). The densities in this region ($\sim 10^{11}$–10^{13} cm^{-3}) are capable of explaining the observed He II emission if the He$^+$ can be ionized by soft X-rays. If we assume that the 54–500 eV photons needed to ionize the He$^+$ come from the post-shock η_A wind, we find that for most of η Car's orbit, the WWC zone is too far from η_A's He$^+$ zone to produce any He II emission (Fig. 11).

Plotting the separation between η_A and the WWC apex as a function of phase assuming the parameters in Table 1, we see that only for $0.986 \lesssim \phi \lesssim 1.014$ does the WWC apex penetrate into the He$^+$ zone of η_A (bottom panel of Fig. 11). Therefore, the soft X-rays from the WWC region can ionize the He$^+$ only during these times. This is almost *exactly* the same range of spectroscopic phases that strong He II λ4686 emission is detected. Furthermore, this is roughly the same range of phases that the post-shock η_B wind is in the radiative-cooling regime. During this time, the post-shock η_B wind will also produce photons capable of ionizing He$^+$.

Martin et al. (2006b) and Mehner et al. (2011) speculated that high densities in the post-shock η_B gas around periastron could lead to a switchover to the radiative-cooling regime, which would make the WWC zone unstable and collapse, and lead to the increased generation of the soft X-rays required to form He II. According to our SPH simulations, a complete WWC collapse is not required for the additional generation of soft X-rays to ionize He$^+$. A mass-ejection event, accretion by η_B and/or changes to a latitudinally dependent primary wind (Martin et al. 2006b; Soker & Behar 2006; Mehner et al. 2011) are also not required. Instead, we suggest that the strong He II λ4686 emission arises in the inner He$^+$ zone of η_A's dense wind and that the first peak in EW observed just before the spectroscopic event ($\phi \approx 0.98$–0.995) is due to a combination of two important effects; (1) penetration of the WWC region into the He$^+$ zone of η_A that allows soft X-rays generated in the WWC zone to ionize the He$^+$ and (2) a switchover of the post-shock wind of η_B to the radiative-cooling regime that results in additional soft X-rays that can ionize the He$^+$ and produce extra
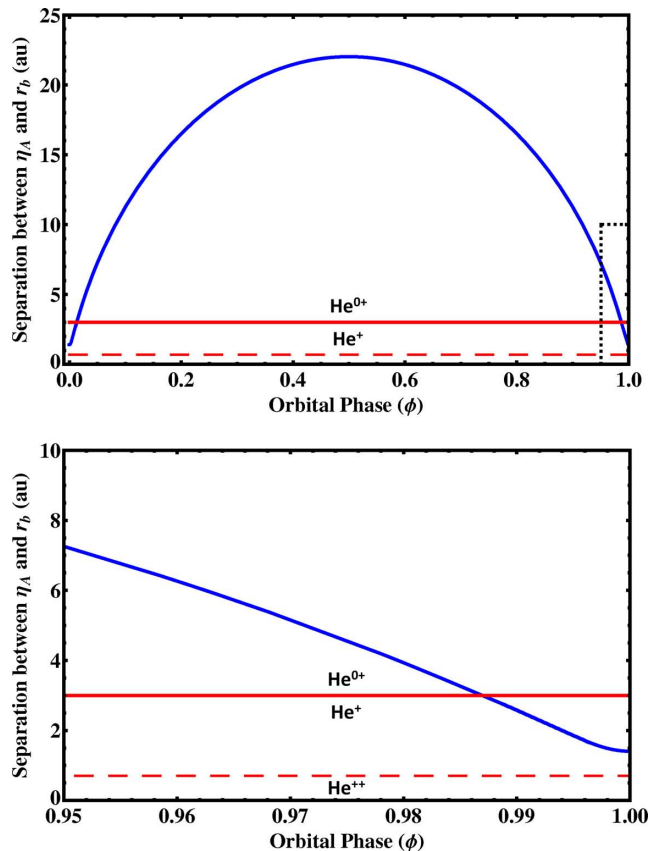
Figure 11. Plot of the separation between η_A and the apex of the WWC zone as a function of orbital phase ϕ, assuming the parameters in Table 1 with $\dot{M}_{\eta_A} = 8.5 \times 10^{-4}$ M$_\odot$ yr^{-1}, $q = 22.28$, and using Equations (A15) and (A19) to determine the location of ram pressure balance (r_b). Apastron occurs at $\phi = 0.5$ and periastron at $\phi = 0, 1$. The solid-red horizontal line indicates the radius in the wind of η_A where, based on fig. 9 of H01, helium transitions from being neutral to singly ionized. The dashed-red line marks the radius in η_A's wind where helium transitions from being singly to doubly ionized ($r \sim 0.7$ au). The lower plot is a zoom of the dashed-box region in the upper plot ($0.95 \leq \phi \leq 1.0$).

He II emission. The fact that the timing of both matches almost perfectly with the observed first He II peak provides strong support for our scenario. The sharp drop in He II EW at $\phi \approx 1.0$ may be due, at least in part, to a physical collapse of the WWC zone at periastron.

We further suggest that the second, smaller emission peak in He II λ4686 that occurs $\sim +20$ d after $\phi = 1.0$ represents the period just after perisatron when η_B returns to our side of the system and begins to carve a new cavity within η_A's wind. During this time, the WWC zone may still be highly unstable, but two important facts will remain. Namely, the WWC region will be within the He$^+$ zone of η_A and the post-shock wind of η_B will be in the radiative-cooling regime and supplying additional soft X-rays to produce He II. The decreased height of the second He II peak could be due to a combination of instability in the WWC zone and increased optical depth in LOS caused by the dense η_A wind that flows in the apastron direction during periastron passage. The He II behaviour should look relatively similar for both a direct view of the central source and reflected spectra corresponding to high stellar latitudes, with some possible changes in the line profiles.

---

[2] We say 'may' because it is possible that the dense post-shock η_A wind will prevent η_B from ionizing neutral helium in the pre-shock η_A wind, in which case there would be no He II λ4686 emission. Detailed 3D radiative transfer simulations are needed to test this though.

4.3.2 Behavior of the He II λ4686 with decreasing $\dot{M}_{\eta_A}$

If $\dot{M}_{\eta_A}$ is lowered to $\sim 2.5 \times 10^{-4}\,\mathrm{M}_\odot\,\mathrm{yr}^{-1}$, keeping the other stellar and wind parameters constant, 1D CMFGEN models show that η_A's He$^+$ zone increases greatly and extends to $r \sim 120$ au. As a result, the WWC zone is within the He$^+$ region for the entire 5.54 yr cycle. Soft X-rays generated in the post-shock η_A wind should ionize the He$^+$ and produce significant, detectable He II emission at all phases, with the exception of a possible short, sharp drop in He II EW at periastron. This emission, though, is not observed.

If $\dot{M}_{\eta_A}$ is lowered to $\sim 5.0 \times 10^{-4}\,\mathrm{M}_\odot\,\mathrm{yr}^{-1}$ while keeping the other parameters constant, CMFGEN models show that η_A's He$^+$ zone extends to $r \sim 7.5$ au, more than a factor of 2 larger than in the $10^{-3}\,\mathrm{M}_\odot\,\mathrm{yr}^{-1}$ model. Combined with the movement of the WWC apex closer to η_A, this should lead to a significant change in the timing of the He II emission peaks. The WWC apex is predicted to penetrate the He$^+$ zone at $\phi \sim 0.94$, or ~ 85 d earlier. The first He II peak should therefore also appear ~ 85 d earlier. While this first peak may appear earlier, its initial amplitude may not be as large. This is because a lower $\dot{M}_{\eta_A}$ produces a shorter cooling-transition phase in η_B's post-shock wind, resulting in the generation of less soft X-rays to ionize the He$^+$. Therefore, an initial, broad He II peak could begin at $\phi \sim 0.94$, created when the WWC apex penetrates the He$^+$ zone and the soft X-rays formed in the post-shock η_A wind produce He II emission. Another sharper peak could then occur near $\phi \sim 0.99$ when η_B's wind switches to the radiative-cooling regime and produces an additional burst of soft X-rays to further ionize the He$^+$ and create additional He II emission. Since the WWC zone will be more stable in a lower $\dot{M}_{\eta_A}$ situation, the sharp drop in He II EW near $\phi = 1.0$ may be delayed, while the recovery to a second He II peak after periastron may be sped up. Because the WWC zone will remain in the He$^+$ zone longer after periastron, the height and duration of the second He II peak should both increase. The time taken for the He II to decline back to near zero EW should also increase.

Based on these results, it is clear that for the explored parameter space, any change in $\dot{M}_{\eta_A}$ of a factor $\gtrsim 2$ should lead to an equally significant change in the behaviour of the He II λ4686 EW. Interestingly, as shown by both Mehner et al. (2011) and Teodoro et al. (2012), the first He II peak during the 2009 event occurred almost exactly 2023 d after the 2003.5 event. This and the fact that the sharp drop in X-rays also occurred nearly 2023 d after the 2003 periaston very strongly suggest that there was no large decrease of $\dot{M}_{\eta_A}$ before 2009. As the available observations make it unclear whether a second He II peak occurred during the 2003 event, there is a possibility $\dot{M}_{\eta_A}$ dropped during the 2009 event. However, such a drop would likely have to be by a factor of $\lesssim 2$ (in contrast to C10), otherwise, there would be a detectable increase in the amount of He II λ4686 emission at phases far from periastron. Such emission is currently not seen. If $\dot{M}_{\eta_A}$ has decreased, or continues to do so, changes in the behaviour of He II λ4686 during the next spectroscopic event in 2014 should be clearly visible.

4.4 Effect on line profiles of broad wind-emission features

4.4.1 Expected changes

Using 2D radiative transfer models, G12a showed that the WWC cavity significantly affects the formation of Hα, Hβ and Fe II lines in η_A's dense extended wind, even at apastron, by reducing the amount of P-Cygni absorption in LOS. Ionization of portions of η_A's extended wind by η_B also affects the shape and strength of these stellar

wind lines (G12a; Groh et al. 2012b, hereafter G12b). The WWC cavity furthermore induces a latitudinal and azimuthal dependence in these line profiles at orbital phases around apastron, explaining the stronger P-Cygni absorption observed in spectra scattered off of the poles of the Homunculus (G12a,b), which was originally interpreted as being caused by rapid stellar rotation (Smith et al. 2003; Mehner et al. 2012). Observed latitudinal changes in the line profiles during periastron, specifically the appearance of strong P-Cygni absorption in LOS, is explained by the flow of dense primary wind towards the observer for a brief period when η_B is behind η_A at periastron (G12a,b; Madura & Groh 2012, see also rows c and d of Figs 2 and B1).

Since the broad wind-emission features of Hα, Hβ and Fe II are so greatly affected by the WWC cavity, a change to $\dot{M}_{\eta_A}$ that alters the WWC opening angle should have significant observable consequences for these and similar lines. We can make some predictions using the SPH simulations and the previous spectral models of H01, H06 and G12a,b. Fig. 11 of H06 shows that, keeping the other parameters (e.g. $R_\star$, $L_\star$, etc.) fixed, as $\dot{M}_{\eta_A}$ is lowered, the Balmer P-Cygni emission and absorption in LOS weaken, with the absorption eventually disappearing. The Fe II emission lines weaken as well, but emission lines of He I strengthen. Eventually, for low enough values of $\dot{M}_{\eta_A}$ ($\sim 2.5 \times 10^{-4}\,\mathrm{M}_\odot\,\mathrm{yr}^{-1}$), lines of N III and He II λ4686 come into emission (H06).

It is important to note that the results of H01, H06 were derived from 1D spherically symmetric radiative transfer models and do not take into account the presence of the WWC cavity or η_B. Inclusion of the WWC cavity will further reduce the amount of Balmer P-Cygni absorption in LOS (G12a). The effect of the cavity on the absorption for a direct view of the central source may be difficult or impossible to detect though since for low values of $\dot{M}_{\eta_A}$ ($\sim 2.5 \times 10^{-4}\,\mathrm{M}_\odot\,\mathrm{yr}^{-1}$), the P-Cygni absorption is sometimes completely absent in the 1D models, depending on the assumed $R_\star$. There is no P-Cygni absorption in Hα in the models only if $R_{\star,\eta_A}$ is small ($\sim 60\,\mathrm{R}_\odot$). Assuming $L_\star = 5 \times 10^6\,\mathrm{L}_\odot$, a model with $60\,\mathrm{R}_\odot$ has a temperature at the hydrostatic core of $T_\star \approx 35\,000$ K, while the model with $300\,\mathrm{R}_\odot$ has $T_\star \approx 15\,000$ K. This results in a big difference in the ionizing fluxes between models, which ultimately determines the amount of Hα absorption.

However, the increase in cavity opening angle *will* alter the latitudinal and azimuthal variation of the P-Cygni absorption (G12a). The photoionization cavity created by η_B will also increase in size. Based on Fig. B1, a factor of 2 or more drop in $\dot{M}_{\eta_A}$ should reduce the η_A wind density, and thus the amount of P-Cygni emission and absorption in Hα, over the stellar poles (see also H06). A factor of 4 drop in $\dot{M}_{\eta_A}$ might result in almost no P-Cygni absorption in Hα over the poles of η_A at phases far from periastron (assuming that the dense, post-shock η_A wind is ionized). The models predict that any larger drop in $\dot{M}_{\eta_A}$ will increase the opening angle of the WWC cavity in such a way that it starts to bend towards η_A, likely resulting in little to no P-Cygni absorption in Hα at high stellar latitudes during most of η Car's cycle.

The SPH simulations also suggest that a drop in $\dot{M}_{\eta_A}$ should result in the detection of less P-Cygni absorption in LOS in Hα and similar lines during periastron passage. This is because, as shown in Figs 1 and B1, as $\dot{M}_{\eta_A}$ is decreased, the volume of η_A wind that flows towards the observer during periastron also decreases, producing a thinner, less-dense wall of η_A wind between the star and the observer after periastron. If $\dot{M}_{\eta_A}$ is low enough ($\sim 2.5 \times 10^{-4}\,\mathrm{M}_\odot\,\mathrm{yr}^{-1}$), for $R_\star = 60\,\mathrm{R}_\odot$, there may be *no* increase in P-Cygni absorption in LOS during periastron since η_A will be able to fully ionize hydrogen in this outflowing primary-wind region (H06). The decreased
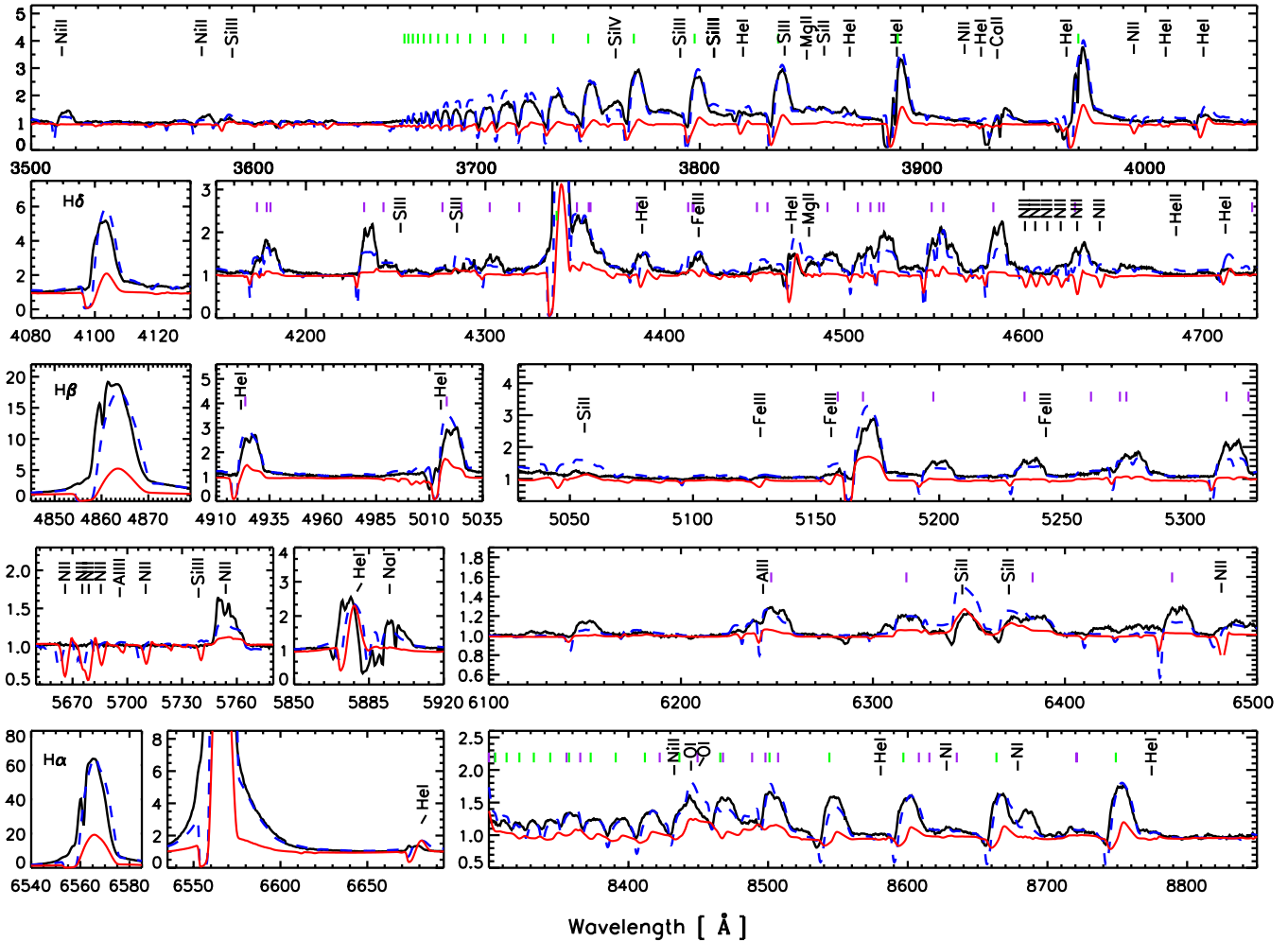
Figure 12. Comparison of the spectrum of η Car observed with *HST*/STIS in 2001 Apr 17 ($\phi = 10.603$; black solid line) with 1D CMFGEN models assuming $v_\infty = 420\,\mathrm{km\,s^{-1}}$ with $\dot{M}_{\eta_A} = 8.5 \times 10^{-4}\,\mathrm{M_\odot\,yr^{-1}}$ (blue dashed line) and $2.5 \times 10^{-4}\,\mathrm{M_\odot\,yr^{-1}}$ (red solid line). The fluxes are continuum normalized. The main spectral lines are identified, with green and purple ticks marking the laboratory wavelength of H and Fe II transitions, respectively. Details on the modelling approach can be found in G12a. We note that a stellar core radius of $300\,\mathrm{R_\odot}$ was used for the $2.5 \times 10^{-4}\,\mathrm{M_\odot\,yr^{-1}}$ model (versus $60\,\mathrm{R_\odot}$ when $\dot{M}_{\eta_A} = 8.5 \times 10^{-4}\,\mathrm{M_\odot\,yr^{-1}}$) in order to keep the He I $\lambda6678$ line contribution from η_A within the observed levels.

thickness and density of the shell will cause it to break apart quicker after periastron as well. The observed duration during which any increased absorption is detected in LOS around periastron should thus also decrease with $\dot{M}_{\eta_A}$.

4.4.2 Comparison to recent observed changes

Mehner et al. (2011, 2012) show that between $\sim$1998 and 2011, the strengths of various broad stellar-wind emission lines (e.g. Hα, Hδ and blends of Fe II, [Fe II], Cr II, [Cr II]) for our direct view of the central source of η Car decreased by factors of 1.5–3 relative to the continuum, while at the same time the line strengths for reflected spectra corresponding to an η_A stellar latitude of $\sim$75° showed no major variations (figs 6 and 7 of Mehner et al. 2012). The terminal velocity was found to be similar at all stellar latitudes and relatively unchanged as well (Mehner et al. 2011, 2012). The lack of any significant changes in η Car's reflected polar spectra poses a serious problem for the hypothesis that there has been a recent large global modification of $\dot{M}_{\eta_A}$. Spherically symmetric 1D radiative transfer models of η Car should be representative of the stellar spectrum at high latitudes, which are mostly unaffected by the WWC cavity

and η_B radiation field (G12b). To illustrate expected changes, we computed a 1D CMFGEN model similar to those described in H01, H06, G12a, but with $\dot{M}_{\eta_A}$ decreased to $2.5 \times 10^{-4}\,\mathrm{M_\odot\,yr^{-1}}$ and $R_{\star,\eta_A}$ increased to $300\,\mathrm{R_\odot}$. This model shows that a factor of 3–4 decrease in $\dot{M}_{\eta_A}$ should produce obvious changes in the reflected polar spectra (Fig. 12). The Hδ emission should decrease by a factor of $\sim$2.5, while Hα and Hβ should show a decrease in emission of a factor of 3–4. The broad Fe II/Cr II blend between 4570 and 4600 Å and other Fe II lines should practically vanish. The emission and absorption of numerous other lines, like He I, would also be affected. Based on these results and the observed lack of any changes over the stellar poles, any recent decrease in $\dot{M}_{\eta_A}$ was probably by a factor of $\lesssim$2. It is beyond the scope of this paper to provide a detailed fit to the post-2009 observations of η_A, since other stellar parameters could have changed in addition to $\dot{M}_{\eta_A}$. Such detailed analysis will be reported elsewhere (Groh et al., in preparation). Additional evidence for the lack of a recent large drop in $\dot{M}_{\eta_A}$ comes from *HST*/STIS measurements of the Hα EW at Weigelt blobs C and D, which show a long-term decrease in emission strength of only $\sim$10–20 per cent (Gull et al. 2009; Mehner et al. 2012). The continuum flux at Weigelt D also has not greatly changed, even though in LOS
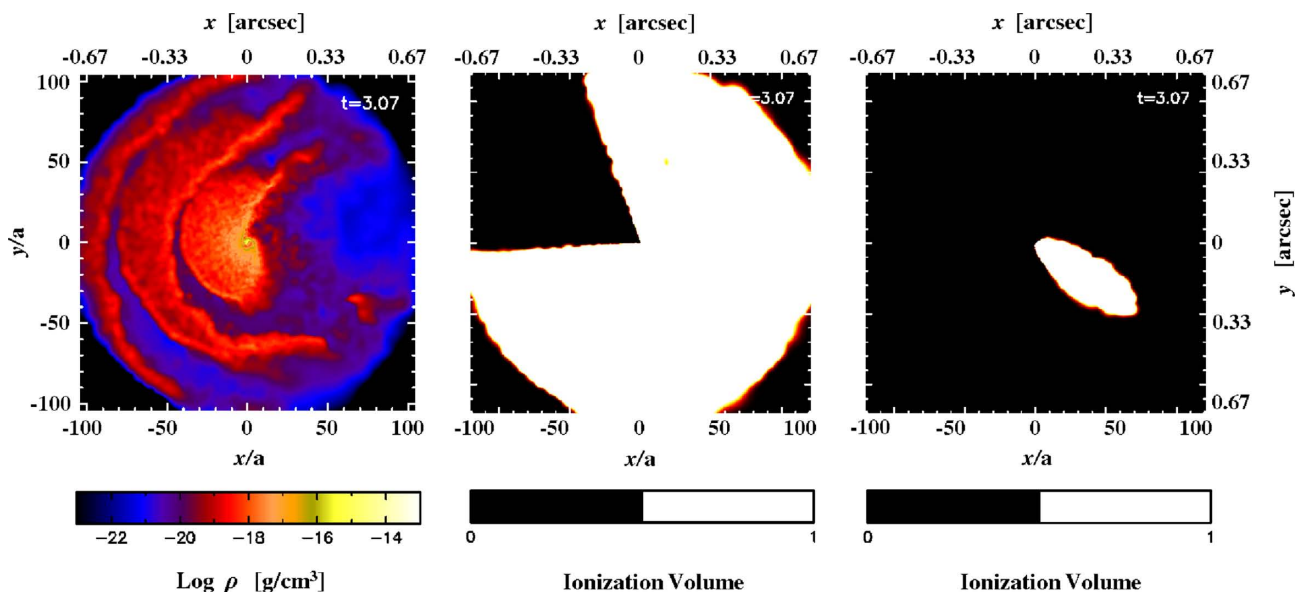
Figure 13. Slices in the orbital plane from an $\dot{M}_{\eta_A} = 2.5 \times 10^{-4}\,\mathrm{M_\odot\,yr^{-1}}$ 3D SPH simulation of η Car showing the density structure (left-hand panel) and photoionization region created by η_B (right two panels) at $\phi = 3.07$, assuming $\mathrm{H^0}$ ionizing fluxes of $10^{49.48}$ photons s^{-1} (middle panel) and $10^{48.2}$ photons s^{-1} (right-hand panel). The method for computing the photoionization region is the same as that in M12, to which we refer the reader for details.

to η_A it has increased by a factor of 10 since 1998 (Gull et al. 2009; Mehner et al. 2012).

4.5 Effects in the UV

G12a showed that the WWC cavity in η Car also has a big influence on the observed UV spectrum, which is strongly dominated by bound–bound transitions of Fe II. Spherically symmetric radiative transfer models have difficulties fitting the observed UV spectrum, even at apastron (H06; G12a). However, the presence of the WWC cavity, introduced in the context of a 2D model, reproduces well both the observed UV and optical spectra of η Car by reducing the optical depth of Fe II transitions in LOS to η_A (G12a).

Given the extremely large UV-emitting region of η_A (H06), any large change in the half-opening angle of the WWC cavity (of $\gtrsim 20°$, G12a) will affect the observed UV spectrum. This is in addition to any other changes in the UV caused by a decrease in $\dot{M}_{\eta_A}$. Fig. 11 of H06 shows that a factor of 4 drop in $\dot{M}_{\eta_A}$ drastically reduces both the emission and absorption of lines between 1250 and 1450 Å. Note also the dramatic increase in emission strength (nearly a factor of 4) of the lines between 1390 and 1410 Å. Detailed 2D models of η Car's UV spectrum for different $\dot{M}_{\eta_A}$ and taking into account the WWC cavity are needed to better determine what changes are expected and can be observed.

Mehner et al. (2011) note that the depth of the minimum in the UV during the 2009 photometric event, as observed in the *F250W* and *F350W* filters on *HST*, was approximately twice as deep as the minimum of the 2003.5 event (their fig. 1), speculating that the increased depth of the 2009 event may be due to a sudden increase in η_A's mass-loss during periastron. However, it is unclear what would cause such enhanced mass-loss. One would normally expect a decrease in $\dot{M}_{\eta_A}$ to reduce the size of the UV photosphere and make it hotter (Mehner et al. 2011). The hypothesized increase in mass-loss around periastron may instead be due to an increase in density in LOS caused by the wind of η_A that flows towards the observer during periastron passage. The primary wind between η_A and the observer at periastron may now be blocking a larger relative

amount of flux in LOS, leading to an increase in the depth of the UV minimum. The increase in WWC opening angle will, however, also alter greatly the amount of UV flux that can escape from the hotter, inner regions of η_A's wind (Madura & Groh 2012). It is unclear how the UV flux in LOS would be affected by such a change, especially given the unusual circumstellar extinction. Therefore, it is difficult to determine whether a decrease in $\dot{M}_{\eta_A}$ is consistent with the observed increased minimum-depth in the UV photometry. Nevertheless, the results of Madura & Groh (2012) show that any large change in WWC opening angle should affect the time-dependent directional UV illumination of circumbinary material in the system (see also Smith et al. 2004b).

4.6 The spatially extended forbidden line emission

Gull et al. (2009) presented an analysis of *HST*/STIS observations taken between 1998 and 2004, identifying spatially extended (up to 0.8 arcsec), velocity-resolved forbidden emission lines from low- and high-ionization[3] species. Using 3D SPH simulations, M12 developed a 3D dynamical model for the broad [Fe III] emission described in Gull et al. (2009) and showed that the broad high-ionization forbidden emission arises in portions of the dense, extended WWC structures photoionized by η_B. The first detailed spatial maps showing the time evolution of the broad [Fe III] emission (Gull et al. 2011) provide strong support for the results of M12.

M12 found that the observed broad forbidden line emission depends strongly on $\dot{M}_{\eta_A}$ and the ionizing flux from η_B. If the flux from η_B remains constant, but $\dot{M}_{\eta_A}$ drops by a factor of 2 or more, the photoionization region created by η_B should grow considerably (Fig. 13). The spatial extent and flux of the observed high-ionization forbidden lines should thus change. The emissivity should decrease with $\dot{M}_{\eta_A}$ since, for densities much less than the line's critical density, the emissivity scales with the density squared (M12). The phase

---

[3] Low and high ionization refer here to atomic species with ionization potentials (IPs) below and above the IP of hydrogen, 13.6 eV.

dependence should differ as well, with the high-ionization emission vanishing at later phases (compared to earlier orbital cycles) when going into periastron, and reappearing at earlier phases afterward. Changes in the WWC opening angle will result in the broad forbidden line emitting regions exhibiting different Doppler velocities, leading to observed variations with slit position angle and spatial location on the sky. New components at different spatial locations and Doppler velocities may appear, while components identified in earlier observations might vanish.

The ring-like [Fe III] emission structures identified by Gull et al. (2009) and modelled by M12 should disappear in future observations if $\dot{M}_{\eta_A}$ drops by a factor of 2 or more. This is because the dense arcs of η_A wind where the broad high-ionization forbidden lines form disperse sooner after periastron the lower the value of $\dot{M}_{\eta_A}$ (see Section 3.2). The flux, location and velocity of broad, redshifted, lower-ionization lines of [Fe II] that form in the periastron side of η_A's wind (Gull et al. 2009; Teodoro et al. 2013) should also change if $\dot{M}_{\eta_A}$ drops. The flux should decrease due to the lower wind density, while the spatial distance from η_A and overall outward velocity of the emitting material should increase due to the increased momentum of η_B's wind relative to that of η_A.

During periastron passage, the high-ionization forbidden line emission vanishes, both the broad features in the interacting stellar winds and the narrow features in the Weigelt blobs (Verner et al. 2005; Gull et al. 2009; Mehner et al. 2010). Gull et al. (2009) found that the high-ionization forbidden emission was absent during the 2003.5 event between $\phi = 1.0$ and 1.068, but reappeared strongly by $\phi = 1.122$.[4] Thus, there is an effective shutting-off of the UV flux from η_B as it becomes temporarily enshrouded in the dense, extended wind of η_A around periastron. Therefore, during the 2003.5 event, $\dot{M}_{\eta_A}$ was large enough to significantly reduce the size of the photoionization region created by η_B, from a few thousand au across to just several au wide. An $\dot{M}_{\eta_A} \sim 10^{-3} \, M_\odot \, \mathrm{yr}^{-1}$ is consistent with this result, assuming η_B is an O5 giant with $T_{\mathrm{eff}} \approx 40\,000 \, \mathrm{K}$ and an H^0 ionizing flux of $10^{49.48}$ photons s^{-1} (Martins, Schaerer & Hillier 2005; Verner et al. 2005; Madura 2010; Mehner et al. 2010, M12). A factor of 4 drop in $\dot{M}_{\eta_A}$ would create a much larger photoionization region during periastron passage (e.g. middle panel of Fig. 13), resulting in large amounts of high-ionization forbidden line emission.

In order to avoid a large photoionization region at $\phi \approx 1.068$ with such a low $\dot{M}_{\eta_A}$, one must drastically reduce the number of ionizing photons from η_B, by a factor of ~ 20 (right-hand panel of Fig. 13). This has important implications for the spectral type of η_B. According to Martins et al. (2005), there are no O-type giants or supergiants with hydrogen ionizing fluxes near $10^{48.2}$ photons s^{-1}. Rather, an O8.5–O9 main-sequence star would be required, with a $T_{\mathrm{eff}} \approx 32\,000 - 34\,000 \, \mathrm{K}$ and $\log L/L_\odot \approx 4.75$-4.85 (Martins et al. 2005). However, such a star lies outside the range of acceptable candidates for η_B from both the works of Verner et al. (2005) and Mehner et al. (2010) (see their fig. 12). Thus, a large drop in $\dot{M}_{\eta_A}$ should reveal itself in the broad forbidden line emission during η Car's next periastron passage in 2014. If not, the implication is either (1) $\dot{M}_{\eta_A}$ has not dropped significantly since 2004 or (2) our current understanding of η_B is incorrect and the star has a lower effective temperature and hydrogen ionizing flux.

Another major issue regarding the forbidden line emission concerns the population of available Fe^+ to be photoionized to Fe^{2+}

by η_B so that [Fe III] emission can form. It is generally accepted that the energy required to ionize Fe^+ to Fe^{2+} comes from photons provided by η_B (Verner et al. 2005; Gull et al. 2009; Mehner et al. 2010). Thus, the iron in any [Fe III] emitting region needs to initially be in the Fe^+ state. H01, H06 show that the ionization structure of η_A's wind and the amount of Fe^+ present depend strongly on charge exchange processes between Fe^{2+} and neutral H via the reaction $Fe^{2+} + H \leftrightarrow Fe^+ + H^+$. According to fig. 9 of H01, which assumes $\dot{M}_{\eta_A} = 10^{-3} \, M_\odot \, \mathrm{yr}^{-1}$, Fe^+ is the dominant ionization state of iron for radii $r \gtrsim 50$ au in η_A's wind. Below this, higher ionization states dominate. However, in CMFGEN models of η_A that assume $\dot{M}_{\eta_A} = 2.5 \times 10^{-4} \, M_\odot \, \mathrm{yr}^{-1}$ (with the other parameters held fixed), H recombination never occurs and the iron is primarily Fe^{2+} in the outer wind. H01, H06 discuss this issue and use it as a reason for favouring a higher $\dot{M}_{\eta_A}$, as it provides a better fit to the observed spectrum.

Thus, if $\dot{M}_{\eta_A}$ were to drop to $\sim 2.5 \times 10^{-4} \, M_\odot \, \mathrm{yr}^{-1}$, Fe^{2+} would be the dominant ionization state of iron in the outer η_A wind. η_B would then be unnecessary for [Fe III] emission to form, provided the η_A wind is in the right density and temperature regimes and has not recombined to Fe^+ or been excited to higher states. This has a number of major ramifications. First, while a hot η_B would not be necessary for [Fe III] emission, η_B's UV flux would be necessary for forming the other observed higher ionization lines of [Ne III] and [Ar III] (Verner et al. 2005; Gull et al. 2009). A large drop in $\dot{M}_{\eta_A}$ would hence lead to huge differences between the wind structures observed in lines like [Ar III] and those of [Fe III].

Secondly, if Fe^{2+} became the dominant state of iron, then broad, *red-shifted* [Fe III] emission would become observable in most directions for most of the binary orbit, arising in the periastron side of η_A's wind and portions of the WWC region that are moving away from the observer. More importantly, the broad [Fe III] emission would not completely vanish during periastron passage. The sudden appearance of large amounts of [Fe II] emission during periastron passage, as previously observed (Gull et al. 2009), would also not occur. If the photoionization region extended far enough, the narrow high-ionization lines that arise in the Weigelt blobs and which also vanish during periastron would remain visible as well.

It is conceivable that in such a low $\dot{M}_{\eta_A}$ situation, the Fe^{2+} in η_A wind that gets compressed in the WWC regions will recombine to Fe^+. Such material on the η_B side of the system could then be photoionized to reform Fe^{2+} and allow [Fe III] emission. Iron in the dense shells of compressed primary wind on the periastron side of η_A created during periastron passage could also recombine to Fe^+. As these shells would be shielded from η_B's radiation, the gas in them would remain in the Fe^+ state and produce broad red-shifted [Fe II] emission. However, the uncompressed η_A wind would still consist of Fe^{2+} and exhibit significant amounts of broad red-shifted [Fe III] emission. This emission would appear at nearly all phases in directions to the south-east on the sky at Doppler velocities up to v_{∞, η_A}. The latest *HST* observations show no such emission (Gull et al. 2011). However, future *HST* observations of the forbidden lines could help constrain any new changes to $\dot{M}_{\eta_A}$. A major benefit of studying the extended, broad forbidden line structures is that they provide an excellent record of η Car's mass-loss over the past 2–3 orbital cycles (Gull et al. 2009, 2011; M12; Teodoro et al. 2013).

4.7 Other expected changes

There are other observable changes expected from a large decrease in $\dot{M}_{\eta_A}$ that are worth briefly mentioning. First, a drop in $\dot{M}_{\eta_A}$ could affect any periodic dust formation during periastron passage, as

---

[4] These are spectroscopic phases, which are not necessarily equal to the orbital phase. The two are not expected to differ by more than four-to-six weeks.

mentioned in Smith (2010). A large decrease in $\dot{M}_{\eta_A}$ would decrease the density in the compressed WWC zone where dust is expected to form, leading to a decrease in the near-IR flux and/or changes to the spectral energy distribution. An overall decrease in primary wind density and WWC-region density could also allow the intense radiation from the stars to more easily destroy any dust that forms. Older dust that lies in extended regions farther from the stars could also be destroyed or heated if intense radiation flowing through the WWC cavity can reach it. This may help explain the recent decrease in extinction and increase in brightness of the central source in LOS, e.g. an increase in WWC opening angle that allows more radiation to escape in LOS and destroy dust between us and the stars, thereby altering the extinction in LOS.

The wavelength-dependent apparent size of η_A is also controlled by the wavelength- and radially dependent opacity and emissivity, which depend on $\dot{M}_{\eta_A}$ (H01, H06, G12a). As $\dot{M}_{\eta_A}$ drops, the continuum extension of η_A in the optical and near-IR should drop as well. In other words, η_A should appear smaller than it was when observed between 2003 and 2004 (van Boekel et al. 2003; Weigelt et al. 2007; Groh et al. 2010b). Continuum flux changes at a given wavelength that occur when the apex of the WWC cavity penetrates the surface of optical depth $\tau = 2/3$ (e.g. the 'bore-hole' effect, see Madura 2010; Madura & Owocki 2010) would also be affected, changing the behaviour of the optical and near-IR photometric eclipse-like events observed to occur every 5.54 yr around periastron (White-lock et al. 2004; Fernández-Lajús et al. 2010; Madura 2010). A reduced $\dot{M}_{\eta_A}$ should cause the eclipse-like events to start later due to the longer time it takes for the WWC cavity to reach optical depth $\tau = 2/3$ in the wind photosphere of η_A. Similarly, the events should end earlier as the apex recedes from the location of optical depth $\tau = 2/3$. For low enough $\dot{M}_{\eta_A}$ ($\lesssim 10^{-4}\,\mathrm{M_\odot\,yr^{-1}}$), the WWC cavity would never penetrate η_A's optically thick wind photosphere and the photometric eclipse-like events would very likely cease. As of the writing of this paper, no significant decrease in the apparent continuum extension of η_A in the near-IR has been observed. No major differences are seen between the 2003.5 and 2009 events in the ground-based optical photometry either (Fernández-Lajús et al. 2010).

5 SUMMARY AND CONCLUSIONS

Using 3D SPH simulations, we showed that $\dot{M}_{\eta_A}$ has profound effects on the 3D time-dependent hydrodynamics of η Car's binary colliding winds on a wide range of spatial scales. These simulations lay the foundation for future work generating synthetic data that can be compared directly to past and future observations of η Car. Such modelling provides information that is important for helping constrain η Car's recent mass-loss history and possible future state.

The 3D SPH simulations and 1D CMFGEN models of η_A's spectra show that for the range of explored values, a factor of 2 or more drop in $\dot{M}_{\eta_A}$ results in substantial changes to numerous observables across a wide range of wavelengths. Below we summarize the most important changes expected.

(1) For $\dot{M}_{\eta_A} \sim 10^{-3}\,\mathrm{M_\odot\,yr^{-1}}$, our LOS intersects portions of the dense, outer WWC region. For lower $\dot{M}_{\eta_A}$ (by factors of 2 or more), our LOS passes primarily through the wind cavity carved by η_B. An increase in WWC opening angle may thus explain the observed brightening of the system and changes to various wind-emission line profiles seen in LOS, with little to no changes at high stellar latitudes or at the Weigelt blobs.

(2) Increases in WWC opening angle cause LOSs to the WWC apex to move into η_A's dense wind at later ϕ as the system goes into periastron, and to move out of η_A's wind at earlier ϕ as the system leaves periastron. Combined with the decreased cooling-transition phase of η_B's post-shock wind, the net result is a shorter X-ray minimum (by ~40–80 d) during periastron passage for simulation Cases B and C, versus Case A.

(3) A decrease in $\dot{M}_{\eta_A}$ leads to a corresponding drop in X-ray flux at phases far from periastron. Decreases in $\dot{M}_{\eta_A}$ also propagate into η Car's extended interacting winds and may change the thermalization and/or absorption of the CCE component.

(4) Increases in WWC opening angle cause the trailing arm of hot post-shock η_B gas to cross the observer's LOS at later ϕ as the system approaches periastron, delaying when the strongest observed X-ray lines become increasingly blueshifted and broader.

(5) As $\dot{M}_{\eta_A}$ is lowered, the spatial extent of the He$^+$ zone in η_A's dense inner wind increases considerably, altering the timing of the emission peaks observed in He II λ4686 around periastron. Assuming an initial $\dot{M}_{\eta_A} = 10^{-3}\,\mathrm{M_\odot\,yr^{-1}}$, a factor of 4 drop should lead to the detection of significant He II emission at all orbital phases. A factor of 2 drop should change the timing of the He II event, with the first peak occurring ~3 months earlier and the second peak lasting ~2–3 months longer.

(6) An increase in WWC opening angle will greatly affect broad wind-emission features of Hα, Hβ and Fe II lines. The amount of Balmer P-Cygni absorption in LOS will be reduced and possibly entirely absent. The latitudinal and azimuthal variation of the Balmer P-Cygni absorption will also change. For $\dot{M}_{\eta_A} \lesssim 2.5 \times 10^{-4}\,\mathrm{M_\odot\,yr^{-1}}$, there could be little to no absorption in reflected spectra over the stellar poles of η_A.

(7) The observed increase in Balmer P-Cygni absorption in LOS during η Car's spectroscopic events should decrease for decreased $\dot{M}_{\eta_A}$. The density and amount of primary wind that flows towards the observer during periastron passage will also decrease. For $\dot{M}_{\eta_A} \lesssim 2.5 \times 10^{-4}\,\mathrm{M_\odot\,yr^{-1}}$, the absorption in LOS during the events should vanish since η_A will be able to easily ionize hydrogen throughout its extended wind.

(8) A decrease in $\dot{M}_{\eta_A}$ by a factor of 2–4 should decrease the emission strength of Hα, Hβ and Hδ by a factor of 2–3. The broad Fe II/Cr II blend between 4570 and 4600 Å and other Fe II lines should practically vanish. Such changes should be visible not only in LOS, but also at high stellar latitudes and in other spatial directions, such as at the Weigelt blobs.

(9) Given the extremely large UV-emitting region of η_A, large changes in WWC half-opening angle of ~20° will alter the observed UV spectrum. Detailed 2D radiative transfer models of the resulting spectrum are needed, but current 1D models show that a factor of 4 drop in $\dot{M}_{\eta_A}$ reduces both the emission and absorption of lines between 1250 and 1450 Å, and increases the emission strength of lines between 1390 and 1410 Å.

(10) The observed broad forbidden line emission depends strongly on $\dot{M}_{\eta_A}$ and the ionizing flux from η_B. As $\dot{M}_{\eta_A}$ drops, the size of the photoionization region where the highest ionization forbidden lines form grows considerably. The size, location, flux and time variability of the various forbidden lines will thus change. Ring-like emission structures that form in the dense arcs of primary wind on the apastron side of the system will be less structured and could vanish altogether since the arcs disintegrate sooner after periastron for lower $\dot{M}_{\eta_A}$.

(11) A decreased η_A wind density due to a large drop in $\dot{M}_{\eta_A}$ may lead to the inability of η_A's wind to trap the ionizing radiation from η_B at periastron. This would cause a drastic change in the behaviour

of the low- and high-ionization forbidden emission lines during periastron passage. The high-ionization lines would no longer vanish at periastron, while the low-ionization lines would fail to appear. This behaviour could occur in both the extended wind structures of η Car and the Weigelt blobs.

(12) For $\dot{M}_{\eta_A} \lesssim 2.5 \times 10^{-4} \, \mathrm{M_\odot \, yr^{-1}}$, Fe^{2+} becomes the dominant ionization state of iron at large radii in η_A's wind, resulting in large amounts of broad, red-shifted [Fe III] emission in most directions over most of the orbital cycle.

(13) A large decrease in $\dot{M}_{\eta_A}$ could affect periodic dust formation during periastron passage since it would decrease the density in the compressed WWC zone and increase the likelihood of heating and/or destruction by the intense stellar radiation fields.

(14) The wavelength-dependent apparent size of η_A in the optical and near-IR continuum decreases with $\dot{M}_{\eta_A}$. Continuum flux changes that occur when the WWC apex penetrates the surface of high optical depth in η_A's wind photosphere would be affected, making the periodic photometric eclipse-like events shorter due to the smaller continuum size of η_A. For $\dot{M}_{\eta_A} \lesssim 10^{-4} \, \mathrm{M_\odot \, yr^{-1}}$, the eclipse-like events would likely cease.

Given all of the multiwavelength changes expected, a recent factor of 2 or more decrease in $\dot{M}_{\eta_A}$ should be discernable with the right observations. However, as discussed in the previous section, there are a large number of inconsistencies between what is observed and what numerous models predict should occur if $\dot{M}_{\eta_A}$ were to drop by a factor of 2–4 from its historically accepted value of $\sim 10^{-3} \, \mathrm{M_\odot \, yr^{-1}}$. One of the most problematic is the lack of any observed changes in the broad wind-emission lines at high stellar latitudes or different spatial locations (Mehner et al. 2012). Also puzzling is the fact that the timing of the start of the 2009 spectroscopic event in X-rays, He II λ4686 and the ground-based optical photometry was not delayed by any noticeable amount. It furthermore seems odd that $\dot{M}_{\eta_A}$ would change with no corresponding change in wind terminal speed. Taken together with the other unobserved but expected changes, it appears that contrary to earlier claims, there has not been a recent significant drop in $\dot{M}_{\eta_A}$. Current evidence suggests that any decrease in $\dot{M}_{\eta_A}$ was likely by a factor of $\lesssim 2$ and occurred sometime after 2004, quite possibly during the 2009 event itself.

We speculate that most of the observed recent changes in η Car are due to a slight ($\lesssim 10°$) increase in the half-opening angle of the WWC zone, which altered the amount of extinction in LOS to the central source. This would explain why the continuum flux and broad wind-emission features in LOS have changed, while features at high latitudes and in other directions (e.g. at the Weigelt blobs) remain relatively constant. It would also explain why the start of the 2009 event at multiple wavelengths did not change. A modest decrease in $\dot{M}_{\eta_A}$ by a factor of $\lesssim 2$ sometime after 2004 could be responsible, and would hardly be surprising given η Car's nature. However, changes in η_B's wind/stellar parameters, while less likely, cannot be fully ruled out at this time. Other less likely alternatives to a drop in $\dot{M}_{\eta_A}$ are discussed in Mehner et al. (2010, 2012).

Finally, we note that the results of Sections 3.1.1 and 3.1.2 depend on rather complicated shock and radiative-wind-driving physics. In addition to the known effects of RI and braking, there is the rather new phenomenon of so-called self-regulated shocks (SRSs), in which ionizing X-rays from the WWC shocks inhibit the wind acceleration of one or both stars, leading to lower pre-shock velocities and lower shocked plasma temperatures (Parkin & Sim 2013). For most of η Car's orbit, the SRS effect is likely to be negligible due to the large binary separation. However, during periastron passage,

SRSs may further inhibit the acceleration of η_B's wind, helping trigger a cooling-transition phase of η_B's post-shock wind and a possible WWC 'collapse'. SRSs may cause the cooling-transition phase to occur earlier and/or last longer compared to what our simulations predict. The potential for a WWC collapse on to η_B in the context of SRSs is difficult to determine without a detailed time-dependent model since radiative braking (not included in the analysis of Parkin & Sim 2013) may prevail over the SRS effect and prevent a wind–photosphere collision (Parkin & Sim 2013). Inclusion of SRSs in future models of η Car is thus worthwhile and may further elucidate the peculiar behaviour of X-rays, He II λ4686 and other lines around periastron.

Many recent works suggest that very massive stars experience extreme η Car-like mass ejections of ~ 1–$10 \, \mathrm{M_\odot}$ in the year to decade before they explode as Type II SNe (Kotak & Vink 2006; Smith et al. 2007; Ofek et al. 2007, 2010, 2013; Chevalier 2012; Quataert & Shiode 2012). The narrow emission lines indicative of Type IIn SNe are interpreted as signatures of the SN ejecta interacting with this freshly expelled circumstellar material (Smith et al. 2007; Ofek et al. 2007, 2013). In fact, the most likely detection of a progenitor before its explosion as a Type IIn involved an LBV (Gal-Yam & Leonard 2009; Ofek et al. 2013), thus raising the question of η Car's near-term fate. η Car's numerous massive eruptions point strongly to repeated phases of instability and may be an indication of its imminent demise as a powerful Type IIn SN (Smith et al. 2007; Stritzinger et al. 2012). Constraining η Car's recent mass-loss history is therefore crucial for determining its possible near- and long-term states. The 3D simulations and analysis in this paper provide detailed information that is important for helping achieve this goal. Extensive monitoring of η Car's next periastron passage in 2014 will undoubtedly play a pivotal role as well.

REFERENCES

Abraham Z., Falceta-Gonçalves D., 2007, MNRAS, 378, 309
Agertz O. et al., 2007, MNRAS, 380, 963
Bate M. R., Bonnell I. A., Price N. M., 1995, MNRAS, 285, 33
Benz W., Bowers R. L., Cameron A. G. W., Press W. H., 1990, ApJ, 348, 647
Blondin J. M., Koerwer J. F., 1998, New Astron., 3, 571
Canto J., Raga A. C., Wilkin F. P., 1996, ApJ, 469, 729
Castor J. I., Abbott D. C., Klein R. I., 1975, ApJ, 195, 157
Chevalier R. A., 2012, ApJ, 752, L2
Conti P. S., 1984, in Maeder A., Renzini A., eds, Proc. IAU Symp. 105, Observational Tests of the Stellar Evolution Theory. Reidel, Dordrecht, p. 233
Corcoran M. F., 2005, ApJ, 129, 2018
Corcoran M. F., 2011, Bull. Soc. R. Sci. Liege, 80, 578
Corcoran M. F., 2013, Cent. Eur. Astrophys. Bull., 37, 283
Corcoran M. F., Ishibashi K., Davidson K., Swank J. H., Petre R., Schmitt J. H. M. M., 1997, Nat., 390, 587
Corcoran M. F., Ishibashi K., Swank J. H., Petre R., 2001, ApJ, 547, 1034 (C01)
Corcoran M. F., Hamaguchi K., Pittard J. M., Russell C. M. P., Owocki S. P., Parkin E. R., Okazaki A., 2010, ApJ, 725, 1528 (C10)
Cox P., Mezger P. G., Sievers A., Najarro F., Bronfman L., Kreysa E., Haslam G., 1995, A&A, 297, 168

Daminelli A., Conti P. S., Lopes D. F., 1997, New Astron., 2, 107
Daminelli A. et al., 2008a, MNRAS, 384, 1649
Daminelli A. et al., 2008b, MNRAS, 386, 2330
Davidson K., 2002, in Eric M. S., Saeqa D. V., eds, ASP Conf. Ser. Vol. 262, The High Energy Universe at Sharp Focus: Chandra Science. Astron. Soc. Pac., San Francisco, p. 267
Davidson K., 2005, in Humphreys R., Stanek K., eds, ASP Conf. Ser. Vol. 332, The Fate of the Most Massive Stars. Astron. Soc. Pac., San Francisco, p. 101
Davidson K., Humphreys R. M., 1997, ARA&A, 35, 1
Davidson K., Ebbets D., Weigelt G., Humphreys R. M., Hajian A. R., Walborn N. R., Rosa M., 1995, AJ, 109, 1784
Davidson K. et al., 1997, AJ, 113, 335
Ferland G. J., Korista K. T., Verner D. A., Ferguson J. W., Kingdon J. B., Verner E. M., 1998, PASP, 110, 761
Fernández-Lajús E. et al., 2010, New Astron., 15, 108
Gal-Yam A., Leonard D. C. A., 2009, Nat., 458, 865
Gayley K. G., 1995, ApJ, 454, 410
Gayley K. G., Owocki S. P., Cranmer S., 1997, ApJ, 475, 786
Groh J. H. et al., 2010a, A&A, 517, A9
Groh J. H., Madura T. I., Owocki S. P., Hillier D. J., Weigelt G., 2010b, ApJ, 716, L223
Groh J. H., Hillier D. J., Madura T. I., Weigelt G., 2012a, MNRAS, 423, 1623 (G12a)
Groh J. H., Madura T. I., Hillier D. J., Kruip C., Weigelt G., 2012b, ApJ, 759, L2 (G12b)
Gull T. R. et al., 2009, MNRAS, 396, 1308
Gull T. R., Madura T. I., Groh J. H., Corcoran M. F., 2011, ApJ, 743, L3
Hamaguchi K. et al., 2007, ApJ, 663, 522 (H07)
Henley D. B., Corcoran M. F., Pittard J. M., Stevens I. R., Hamaguchi K., Gull T. R., 2008, ApJ, 680, 705
Hillier D. J., Davidson K., Ishibashi K., Gull T., 2001, ApJ, 553, 837 (H01)
Hillier D. J. et al., 2006, ApJ, 642, 1098 (H06)
Humphreys R., Davidson K., 1994, PASP, 106, 1025
Humphreys R. M., Davidson K., Koppelman M., 2008, AJ, 135, 1249
Ishibashi K., Corcoran M. F., Davidson K., Swank J. H., Petre R., Drake S. A., Daminelli A., White S., 1999, ApJ, 524, 983
Kashi A., Soker N., 2009, New Astron., 14, 11
Kotak R., Vink J. S., 2006, A&A, 460, 5
Madura T. I., 2010, PhD dissertation, Univ. Delaware
Madura T. I., Groh J. H., 2012, ApJ, 746, L18
Madura T. I., Owocki S. P., 2010, Rev. Mex. Astron. Astrofis. Ser. Conf., 38, 52
Madura T. I., Gull T. R., Owocki S. P., Groh J. H., Okazaki A. T., Russell C. M. P., 2012, MNRAS, 420, 2064 (M12)
Martin J. C., Davidson K., Koppelman M., 2006a, AJ, 132, 2717
Martin J. C., Davidson K., Humphreys R. M., Hillier D. J., Ishibashi K., 2006b, ApJ, 640, 474
Martins F., Schaerer D., Hillier D. J., 2005, A&A, 436, 1049
Mehner A., Davidson K., Ferland G. J., Humphreys R. M., 2010, ApJ, 710, 729
Mehner A., Davidson K., Martin J. C., Humphreys R. M., Ishibashi K., Ferland G. J., 2011, ApJ, 740, 80
Mehner A., Davidson K., Humphreys R. M., Ishibashi K., Martin J. C., Ruiz M. T., Walter F. M., 2012, ApJ, 751, 73
Moffat A. F. J., Corcoran M. F., 2009, ApJ, 707, 693
Monaghan J. J., 1992, ARA&A, 30, 543
Monaghan J. J., 2005, Rep. Prog. Phys., 68, 1703
Nielsen K. E., Corcoran M. F., Gull T. R., Hillier D. J., Hamaguchi K., Ivarsson S., Lindler D. J., 2007, ApJ, 660, 669
Ofek E. O. et al., 2007, ApJ, 659, L13
Ofek E. O. et al., 2010, ApJ, 724, 1396
Ofek E. O. et al., 2013, Nat., 494, 65
Okazaki A. T., Owocki S. P., Russell C. M. P., Corcoran M. F., 2008, MNRAS, 388, L39 (O08)
Parkin E. R., Pittard J. M., 2008, MNRAS, 388, 1047
Parkin E. R., Sim S. A., 2013, ApJ, 767, 114
Parkin E. R., Pittard J. M., Corcoran M. F., Hamaguchi K., Stevens I. R., 2009, MNRAS, 394, 1758 (P09)
Parkin E. R., Pittard J. M., Corcoran M. F., Hamaguchi K., 2011, ApJ, 726, 105 (P11)
Pittard J. M., 2009, MNRAS, 396, 1743
Pittard J. M., Corcoran M. F., 2002, A&A, 383, 636
Price D. J., 2004, PhD dissertation, Univ. Cambridge
Price D. J., 2008, J. Comput. Phys., 227, 10040
Quataert E., Shiode J., 2012, MNRAS, 423, L92
Russell C. M. P., 2013, PhD dissertation, Univ. Delaware
Smith N., 2006, ApJ, 644, 1151
Smith N., 2010, MNRAS, 402, 145
Smith N., 2011, MNRAS, 415, 2020
Smith N., Owocki S., 2006, ApJ, 645, L45
Smith N., Townsend R., 2007, ApJ, 666, 967
Smith N., Davidson K., Gull T. R., Ishibashi K., Hillier D. J., 2003, ApJ, 586, 432
Smith N. et al., 2004a, ApJ, 605, 405
Smith N., Morse J. A., Collins N. R., Gull T. R., 2004b, ApJ, 610, L105
Smith N. et al., 2007, ApJ, 666, 1116
Soker N., Behar E., 2006, ApJ, 652, 1563
Stahl O., Weis K., Bomans D. J., Davidson K., Gull T. R., Humphreys R. M., 2005, A&A, 435, 303
Steiner J. E., Daminelli A., 2004, ApJ, 612, L133
Stevens I. R., Pollock A. M. T., 1994, MNRAS, 269, 226
Stevens I. R., Blondin J. M., Pollock A., 1992, ApJ, 386, 265
Stritzinger M. et al., 2012, ApJ, 756, 173
Teodoro M. et al., 2012, ApJ, 746, 73
Teodoro M., Madura T. I., Gull T. R., Corcoran M., Hamaguchi K., 2013, ApJ, 773, L16
Townsend R. H. D., 2009, ApJS, 181, 391
van Boekel R. et al., 2003, A&A, 410, L37
Verner E., Bruhweiler F., Gull T., 2005, ApJ, 624, 973
Vishniac E. T., 1994, ApJ, 428, 186
Weigelt G., Ebersberger J., 1986, A&A, 163, L5
Weigelt G. et al., 2007, A&A, 464, 87
Whitelock P. A., Feast M. W., Marang F., Breedt E., 2004, MNRAS, 352, 447
Wünsch R., Dale J. E., Palous J., Whitworth A. P., 2010, MNRAS, 407, 1963

APPENDIX A: AN ANTIGRAVITY APPROACH FOR IMPLEMENTING RADIATIVE FORCES IN SPH SIMULATIONS OF COLLIDING STELLAR WINDS

A1 Basic approach

The SPH method used for the simulations in this paper follows the Lagrangian motion of the modelled gas particles, removing the need for a complex spatial grid. In the SPH scheme, spatial derivatives are calculated via analytical differentiation of interpolation formulae (Monaghan 1992), as opposed to Eulerian grid-based methods where derivatives are computed using finite-difference or finite-volume techniques. While the SPH approach allows us to perform large-scale 3D simulations with significantly less computational cost compared to a grid-based code, the lack of a spatial grid complicates the calculation of the projected velocity gradient required for computing the CAK (Castor, Abbott & Klein 1975) line force that drives the individual stellar winds. We therefore employ an alternative approach, described below, that produces a stellar wind that follows the desired beta-velocity law and is consistent with the results of standard CAK theory.

We start by considering the radial equation of motion for a steady, spherically symmetric stellar wind driven by a radiation force $g_{\rm rad} = \kappa L_\star/(4\pi c r^2)$ and competing against stellar gravity $GM_\star/r^2$:

$$v\frac{{\rm d}v}{{\rm d}r} = g_{\rm rad} - \frac{GM_\star}{r^2}\,. \tag{A1}$$

Here, v is the wind speed, r is the local radius, $M_\star$ and $L_\star$ are the stellar mass and luminosity, κ is the wind opacity and c is the speed of light. We neglect standard sound speed terms that are, in practice, negligible. Since the key to driving a stellar wind is overcoming gravity, it is convenient to define a dimensionless equation of motion that is scaled by the gravity,

$$\frac{{\rm d}w}{{\rm d}x} = \Gamma - 1\,, \tag{A2}$$

where the dependent variable $w \equiv v^2/v_{\rm esc}^2$ is the ratio of the radial kinetic energy to the surface escape energy $v_{\rm esc}^2 = 2GM_\star/R_\star$, and the independent variable is the inverse radius coordinate $x \equiv 1 - R_\star/r$, measured from the stellar surface radius $R_\star$. $\Gamma \equiv r^2 g_{\rm rad}/(GM_\star)$ is the ratio of the local radiative force to gravity, sometimes called the 'Eddington parameter'.

A simple model to consider is one in which we assume that, at some $R_\star$, $g_{\rm rad}$ suddenly jumps from below gravity to some fixed factor $\Gamma > 1$ above gravity. In such a simple 'antigravity' model, static material at the surface $R_\star$ effectively 'falls' away from the star with a local net outward acceleration at radius r of $(\Gamma - 1)GM_\star/r^2$. In terms of equation (A2), integration yields a solution $w(x) = (\Gamma - 1)x$, which in dimensional form gives $v(r) = v_\infty(1 - R_\star/r)^{1/2}$, where $v_\infty = v_{\rm esc}\sqrt{\Gamma - 1}$. This is just a specific $\beta = 1/2$ form of the beta-velocity law $v(r) = v_\infty(1 - R_\star/r)^\beta$.

While we considered only a simple example above, this antigravity approach can readily give a beta-velocity law with any index β. To demonstrate this, we rewrite equation (A2) in terms of $v(x)$ and require the Eddington parameter to have a spatial variation $\Gamma(x)$. Then,

$$\frac{2v(x)}{v_{\rm esc}^2}\frac{{\rm d}}{{\rm d}x}v(x) = \Gamma(x) - 1\,. \tag{A3}$$

With $v(x) = v_\infty x^\beta$ and defining $w_\infty \equiv v_\infty^2/v_{\rm esc}^2$, the above gives

$$\Gamma(x) = 2\beta w_\infty x^{2\beta - 1} + 1\,. \tag{A4}$$

Obtaining the desired velocity laws simply requires specifying the correct opacity for each wind. Using equation (A4) together with $\Gamma(r) = r^2 g_{\rm rad}/(GM_\star) = \kappa L_\star/(4\pi GM_\star c)$ yields

$$\kappa_i(r_i) = \frac{4\pi c}{L_i}\left[v_{\infty,i}^2 R_i \beta_i (1 - R_i/r_i)^{2\beta_i - 1} + GM_i \right]\,, \tag{A5}$$

where $i = 1, 2$ correspond to the individual stars and r_i is measured with respect to star i. Achieving the different wind terminal speeds requires $\kappa_1 \neq \kappa_2$. However, regions where the two winds mix requires weighting the local opacity by the relative mass contribution from each star,

$$\bar{\kappa} = \kappa_1\left(\frac{\rho_1}{\rho}\right) + \kappa_2\left(\frac{\rho_2}{\rho}\right) = \kappa_1 + (\kappa_2 - \kappa_1)\frac{\rho_2}{\rho}\,, \tag{A6}$$

where $\rho = \rho_1 + \rho_2$ is the total density.

In order to ensure that the stellar mass-loss rates correspond to what is expected from CAK theory, e.g.

$$\dot{M}_{\rm CAK} = \frac{L_\star}{c^2}\frac{\alpha}{1-\alpha}\left[\frac{\bar{Q}\Gamma}{1-\Gamma}\right]^{(1-\alpha)/\alpha} \quad \text{(Gayley 1995)}, \tag{A7}$$

we require that the ratio of the two stellar luminosities satisfy

$$\frac{L_2}{L_1} = \left(\frac{M_2}{M_1}\right)^{1-\alpha}\left(\frac{\dot{M}_2}{\dot{M}_1}\right)^\alpha\,, \tag{A8}$$

where α, typically $= 2/3$, is the CAK power index. Given an observed primary star luminosity L_1, the above equation can be used to find that of the secondary, L_2. Therefore, with L_1 and M_i, R_i, $\dot{M}_i$, β_i and $v_{\infty,i}$ specified for each of the stars, the total force per mass $g_{\rm tot}$ exerted on the wind particles can be computed as corrections to the vector gravities g_i of the stars,

$$g_{\rm tot} = \left(1 - \frac{\bar{\kappa}L_1}{4\pi GM_1 c}\right)g_1 + \left(1 - \frac{\bar{\kappa}L_2}{4\pi GM_2 c}\right)g_2\,. \tag{A9}$$

With the above formalism in place, we incorporate the effect of radiative forces into the 3D SPH simulations by

(1) Specifying the input parameters $L_1 = 5 \times 10^6\,{\rm L}_\odot$ and M_i, R_i, $\dot{M}_i$, β_i and $v_{\infty,i}$ for each star (Table 1).

(2) For the given L_1 and assumed stellar mass and mass-loss rate ratios, using equation (A8) with $\alpha = 2/3$ to obtain L_2.

(3) Using equation (A5) to compute κ_1 and κ_2. Particles from each star are distinguished via their specified distinct masses.

(4) Computing $\bar{\kappa}$ at each location in the wind using equation (A6).

(5) Computing the associated $g_{\rm tot}$ at each point with equation (A9).

The stellar winds are initiated at twice the sound speed in order to ensure information characteristics that point from the star into the computational domain. The SPH particles from each star i are injected at a radius $r_{{\rm inj},i} = R_i/[1 - (2c_s/v_{\infty,i})^{1/\beta_i}]$, where the sound speed $c_s = \sqrt{T\gamma k_B/\mu}$ and T, γ, k_B and μ are the photospheric temperature, ratio of specific heats, Boltzmann's constant and mean molecular weight, respectively.

Fig. A1 shows that the antigravity method produces the correct wind-velocity and density structures. Plots of $v(r)$ and $\rho(r)$ through the back side of η_A's wind, taken at apastron from the $\dot{M}_{\eta_A} = 8.5 \times 10^{-4}\,{\rm M}_\odot\,{\rm yr}^{-1}$ 3D SPH simulation, are compared to the analytic expressions $v(r) = v_\infty(1 - R_\star/r)^\beta$ and $\rho(r) = \dot{M}/[4\pi r^2 v(r)]$ for the wind structure of an isolated star, assuming the values for η_A from Table 1. The SPH simulation results are in very good agreement with the analytic scalings, which helps
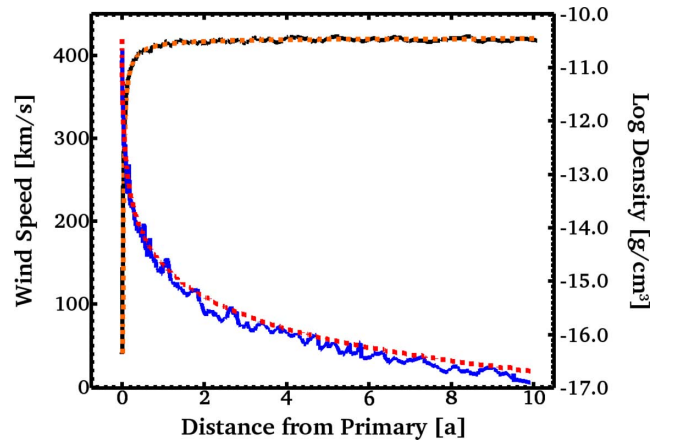
Figure A1. Line plots of the total wind speed (orange and black) and log density (red and blue) as a function of distance from η_A (in units of $a = 15.45$ au) taken from the $\dot{M}_{\eta_A} = 8.5 \times 10^{-4}\,{\rm M}_\odot\,{\rm yr}^{-1}$ 3D SPH simulation at apastron (solid lines) compared to the simple analytic expressions for $v(r)$ and $\rho(r)$ for an isolated star (dashed lines).
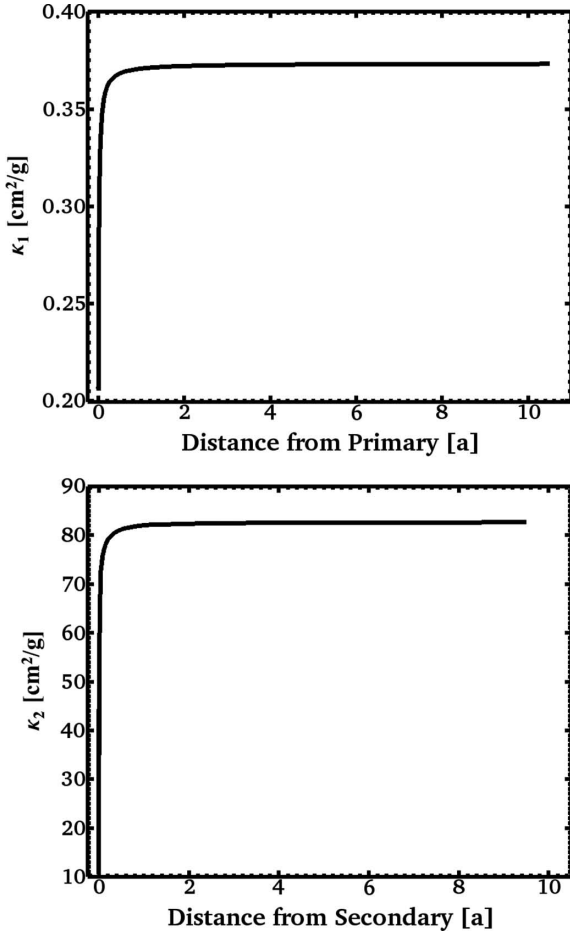
Figure A2. Line plots of the opacity κ_i (equation A5) as a function of distance from the star (in units of $a = 15.45$ au) for η_A (top) and η_B (bottom) for the $\dot{M}_{\eta_A} = 8.5 \times 10^{-4} \, \text{M}_\odot \, \text{yr}^{-1}$ simulation.

verify our approach and results. Fig. A2 shows line plots of the opacity κ_i used to drive the individual stellar winds for the desired mass-loss rates and wind terminal speeds. Note that κ_2 is significantly larger than κ_1. More extensive testing and analysis of the antigravity method can be found in Russell (2013).

A2 An analytic solution for the flow along the line of centres

Since the radiative force from both stars is present throughout the computational domain, the velocity-altering effects of RI and stellar gravity are included in the simulations (Stevens & Pollock 1994; Russell 2013). To assist in the interpretation and understanding of the 3D SPH simulations, we derive here a sample analytic 1D solution for the effect of the antigravity radiative forces on the flow along the line of centres between the stars. Because the SPH simulations use $\beta = 1$ velocity laws to parametrize the stellar winds, we focus on the $\beta = 1$ case.

As η_B has a much lower luminosity than η_A, its wind will be the one most strongly affected by the radiative force of its companion. We therefore investigate how η_B's wind velocity along the line of centres is affected by the radiation and gravity of η_A. The equation of motion along the line of centres in terms of the radius r measured

from η_B, for a given binary separation D, is

$$v_2 \frac{dv_2}{dr} = \frac{GM_1}{(D-r)^2}\left(1 - \frac{\bar{\kappa}L_1}{4\pi GM_1 c}\right) - \frac{GM_2}{r^2}\left(1 - \frac{\bar{\kappa}L_2}{4\pi GM_2 c}\right), \quad \text{(A10)}$$

where subscripts 1 and 2 refer to η_A and η_B, respectively. Because we are interested in the effect of η_A in slowing η_B's wind before the WWC, we can set $\bar{\kappa} = \kappa_2$. Multiplying both sides of equation (A10) by $r^2/(GM_2)$ and using the definition of the Eddington parameter $\Gamma_i = \kappa_i L_i/(4\pi GM_i c)$, we get

$$\frac{v_2 r^2}{GM_2}\frac{dv_2}{dr} = (\Gamma_2 - 1) - \frac{r^2}{(D-r)^2}\left(\frac{M_1}{M_2}\right)\left[\frac{\kappa_2 \Gamma_1}{\kappa_1} - 1\right]. \quad \text{(A11)}$$

Defining $x \equiv 1 - R_2/r$, $w \equiv (v_2^2 R_2)/(2 GM_2)$, $q \equiv L_1/L_2$, $m \equiv M_1/M_2$, and using the fact that $\kappa_i = (4\pi GM_i c\Gamma_i)/L_i$, equation (A11) becomes

$$\frac{dw}{dx} = (\Gamma_2 - 1) - \frac{q\Gamma_2 - m}{[D(1-x)/R_2 - 1]^2}. \quad \text{(A12)}$$

Equation (A4) gives the spatial variation of Γ with x. Therefore, for $\beta = 1$ and $w_\infty \equiv (v_{\infty,2}/v_{\text{esc},2})^2$, $\Gamma_2(x) = 1 + 2w_\infty x$ and

$$\frac{dw}{dx} = 2w_\infty x - \frac{q(1 + 2w_\infty x) - m}{[D(1-x)/R_2 - 1]^2}. \quad \text{(A13)}$$

Equation (A13) can be integrated straightforwardly to give the variation of the scaled wind kinetic energy w as a function of the scaled inverse radius x. Letting $d \equiv D/R_2$, we find

$$w(x) = w_\infty x^2 - \frac{2qw_\infty \ln[(1-x)d - 1]}{d^2}$$
$$+ \frac{qd - md - 2qw_\infty + 2qdw_\infty}{d^2[1 + (x-1)d]}. \quad \text{(A14)}$$

With $w/w_\infty = (v_2/v_{\infty,2})^2$, the radial variation of the velocity of η_B's wind along the line of centres can be found from

$$\frac{v_2^2}{v_{\infty,2}^2} = \left(1 - \frac{R_2}{r}\right)^2 - \frac{2qR_2^2}{D^2}\ln\left[\frac{D}{r} - 1\right] + \frac{2qR_2(1 - \frac{R_2}{D})}{D(1 - D/r)}$$
$$+ \frac{2GM_2(q-m)}{v_{\infty,2}^2 D(1 - D/r)}. \quad \text{(A15)}$$

The corresponding expression for the radial variation of η_A's wind velocity v_1 along the line of centres is similarly

$$\frac{v_1^2}{v_{\infty,1}^2} = \left(1 - \frac{R_1}{r'}\right)^2 - \frac{2q'R_1^2}{D^2}\ln\left[\frac{D}{r'} - 1\right] + \frac{2q'R_1(1 - \frac{R_1}{D})}{D(1 - D/r')}$$
$$+ \frac{2GM_1(q'-m')}{v_{\infty,1}^2 D(1 - D/r')}, \quad \text{(A16)}$$

where $q' = 1/q$, $m' = 1/m$ and r' is measured from η_A.

In addition to the effects of RI, orbital motion will increase the wind speeds as the system moves from apastron to periastron. The stellar velocity along the line of centres for each star i with respect to the system COM is $v_{r,i} = \sqrt{v_\star^2 - v_{t,i}^2}$, where

$$v_{t,1} = hM_2/(M_T D)$$
$$v_{t,2} = hM_1/(M_T D) \quad \text{(A17)}$$

are the transverse components of the stellar velocities with respect to the COM, and $M_T = M_1 + M_2$, $h^2 = GaM_T(1 - e^2)$, G is the
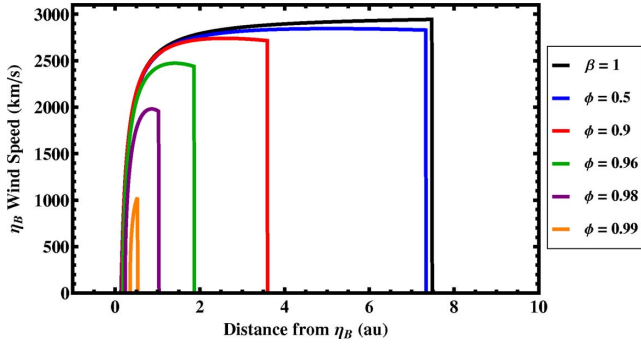
Figure A3. Total η_B wind speed $v_{2,\text{tot}} = v_2 + v_{r,2}$ along the line of centres as a function of distance from η_B assuming the parameters in Table 1 and $\dot{M}_{\eta_A} = 8.5 \times 10^{-4}\,\text{M}_\odot\,\text{yr}^{-1}$, $q = 22.28$, for binary separations D corresponding to $\phi = 0.5$ (apastron), 0.9, 0.96, 0.98 and 0.99. For reference, the solid black line is the standard $\beta = 1$ law without RI effects. Each curve is truncated at the radius of ram pressure balance r_b given by equation (A19), indicated by the vertical lines. There is no stable balance at periastron ($\phi = 1$), implying that η_B cannot drive a wind towards η_A.

gravitational constant, a is the semimajor axis length, e is the orbital eccentricity and $v_\star$ is the stellar orbital speed given by

$$v_\star^2 = GM_T \left(\frac{2}{D} - \frac{1}{a} \right) . \tag{A18}$$

Fig. A3 plots the total η_B wind speed along the line of centres $v_{2,\text{tot}} = v_2 + v_{r,2}$ versus r for several D corresponding to various phases leading up to periastron. Each curve is truncated at the radius of wind–wind ram pressure balance r_b measured from η_B (indicated by the vertical lines), which is found by solving the ram pressure balance condition

$$\frac{D}{r_b} = 1 + \sqrt{\frac{\dot{M}_1[v_1(r' = D - r_b) + v_{r,1}]}{\dot{M}_2[v_2(r = r_b) + v_{r,2}]}} , \tag{A19}$$

where $v_2(r = r_b)$ and $v_1(r' = D - r_b)$ are given by equations (A15) and (A16). The standard $\beta = 1$ velocity-law profile for η_B is included for comparison.

Note how when the effects of RI are included, η_B's wind is initially accelerated from the stellar surface, but then eventually decelerates as it approaches η_A. The offset position from η_A of the deceleration depends on the luminosity ratio q. This deceleration weakens the colliding wind shocks in the 3D SPH simulations and enhances the dominance of η_A's wind over that of η_B, thus moving the WWC apex closer to η_B and narrowing the opening angle of the WWC zone around η_B. Because it has a strong dependence on the binary separation D, these velocity-altering effects are time dependent and most pronounced near periastron.

We find there is no stable balance solution at $\phi = 1$, i.e. according to equation (A15), η_B cannot drive a wind along the line of centres towards η_A at periastron. This implies that in the absence of other effects, η_A's wind would collide with the surface of η_B. However, because we set $\bar{\kappa} = \kappa_2$ in equation (A10), there is a strong coupling between η_A's radiation field and η_B's wind. To investigate the effect of a weaker coupling analogous to that used by P11, we rederived equation (A15) assuming $\bar{\kappa} = \kappa_1$ for the coupling between η_A's radiation and η_B's wind. Fig. A4 plots the resulting total η_B wind speed along the line of centres. One notices immediately that the weaker coupling decreases greatly the importance of RI and leads to much higher pre-shock η_B wind speeds. The higher pre-shock
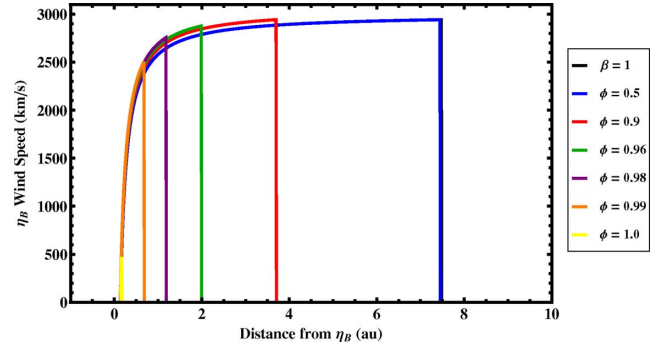
Figure A4. Same as Fig. A3, but using $\bar{\kappa} = \kappa_1$ for the influence of η_A's radiation field on η_B's wind and including periastron ($\phi = 1.0$). The solid blue line for $\phi = 0.5$ overlaps almost exactly with the solid black line that corresponds to the standard $\beta = 1$ law without RI effects. Unlike Fig. A3, there is a stable ram balance at periastron.

wind speeds reduce the importance of radiative cooling in the post-shock gas and there is no longer a 'collapse' of the WWC zone at periastron, but rather a stable ram balance. This is the same result obtained by P11, indicating that a strong coupling between η_A's radiation field and η_B's wind is necessary for RI effects to be important.

A3 Possible changes to $\dot{M}$

Because we fix the mass-loss rates in our antigravity approach, possible changes to the stellar mass-loss due to RI are not included. Such changes though are not expected to be significant in η Car, with the exception of at periastron for η_B.

As demonstrated in Russell (2013), the mass-loss rate factor $\dot{m}$ that describes the change in star 1's mass-loss rate due to the radiation and gravity of star 2 is

$$\dot{m} = \left[1 - \frac{L_2}{L_1} \left(\frac{R_1}{R_2} \right)^2 \left(1 - \left[1 - \left(\frac{R_2}{D - R_1} \right)^2 \right]^{1+\alpha} \right) \right]^{\frac{1}{\alpha}}$$
$$\times \left[1 - \frac{M_2/M_1}{(D/R_1 - 1)^2} \right]^{1 - \frac{1}{\alpha}} , \tag{A20}$$

Using the values in Table 1 and $\alpha = 2/3$, we find that the radiation and gravity of η_B are insufficient to modify η_A's mass-loss rate at any phase, and so $\dot{m} = 1$ for the entire 5.54 yr orbit and there is no difference in $\dot{M}_{\eta_A}$ compared to the expected single-star values.

For most of η Car's cycle ($0.5 \leq \phi \leq 0.98$), D is large enough that η_A does not modify η_B's mass-loss and $\dot{m} \approx 1$. At $\phi = 0.99$, $\dot{m} \approx 0.87$ and there is a slight reduction in η_B's $\dot{M}$. Only between $\phi = 0.996$ ($\dot{m} \approx 0.66$) and periastron ($\dot{m} \approx 0.52$) is there a significant reduction in the $\dot{M}$ of η_B. Since this occurs only for an extremely brief period at periastron, it should not greatly affect our results or conclusions. We further note that the above results assume $\dot{M}_{\eta_A} = 8.5 \times 10^{-4}\,\text{M}_\odot\,\text{yr}^{-1}$ and $q = 22.28$ (Table 1). Because our lower $\dot{M}_{\eta_A}$ simulations use slightly larger η_B luminosities, the reduction in η_B's $\dot{M}$ will be less, with $\dot{m} \approx 0.66$ and 0.79 at periastron for $\dot{M}_{\eta_A} = 4.8 \times 10^{-4}\,\text{M}_\odot\,\text{yr}^{-1}$ and $2.4 \times 10^{-4}\,\text{M}_\odot\,\text{yr}^{-1}$, respectively.

APPENDIX B: THE STRUCTURE OF ETA CAR'S BINARY COLLIDING WINDS IN THE *xz* AND *yz* PLANES PERPENDICULAR TO THE ORBITAL PLANE

B1 Results from the small-domain simulations

Figs B1 through B4 show density and temperature slices in the *xz* and *yz* planes perpendicular to the orbital plane at the same five orbital phases of Figs 1 and 2 for the small-domain 3D SPH simulations, allowing one to more fully appreciate the complex 3D structure of the winds and their collision. Row a of Figs B1 and B2 further demonstrates the axisymmetry of the shock cone at phases around apastron, the increase in cavity opening angle with decreasing $\dot{M}_{\eta_A}$, and the increase in distance between the WWC apex and η_A as $\dot{M}_{\eta_A}$ is increased. Decreases in the thickness, density and stability of the cold, post-shock primary wind region with decreasing $\dot{M}_{\eta_A}$ are also apparent.

At $\phi = 0.9$, the WWC zone starts to become distorted and η_B begins to move to the back side of η_A. Slices centred in the *xz* plane sample the leading edge of the trailing arm of the WWC zone above and below the orbital plane. Fig. B2 shows the changing temperature structure of the hot post-shock η_B wind as the trailing arm sweeps through the *xz* plane. The *xz* slice at $\phi = 0.9$ samples more of the leading edge of the trailing arm the higher the value of $\dot{M}_{\eta_A}$. This is because higher $\dot{M}_{\eta_A}$ produce smaller shock-cone opening angles. The overall result is the appearance that the arms of the hot shock increase in width in the *xz* plane as the system moves from $\phi = 0.5$ to 0.9, filling in the cooler wind cavity.

At periastron (row c), η_B is behind η_A, and there is a brief moment when the wind of η_A can flow unimpeded in the $+x$ (apastron) direction. During this time, the apex of the low-density cavity on the $+x$ side of the system fills with dense η_A wind. The inner η_A wind region in the $+x$ direction also starts to look more spherical (see e.g. row d of Fig. B1). The thickness and density of this inner primary wind region increases with $\dot{M}_{\eta_A}$. The wind momentum balance is responsible for this since a higher value of $\dot{M}_{\eta_A}$ moves the apex of the WWC zone farther from η_A, allowing the primary wind to fill a larger volume in the $+x$ direction during periastron passage. Slices in the *xz* plane at periastron also sample mostly cold ($\sim 10^4$ K) material from both winds, although the η_B wind cavity in the lower $\dot{M}_{\eta_A}$ simulations contains warmer material due to the larger WWC opening angle and less oblique shocks.

Following periastron, η_B emerges from η_A's dense wind, carving a new low-density wind cavity that is visible on the $-x$ side of the *xz*-plane slices (Figs B1 and B2, row d). Eventually η_B moves back to the $+x$ side of the system and the WWC zone is reestablished (row e). A new wind cavity is slowly carved in η_A's wind on the $+x$ side while the spiral WWC region and low-density cavity created on the $-x$ side flow outward. Due to the more similar wind momenta, the wind cavity is larger and hotter in the lower $\dot{M}_{\eta_A}$ simulations. The size and geometry of the cavities on the $+x$ and $-x$ sides of the system are also very distinct. The wind of η_B is able to plough through the dense shell of primary wind on the $+x$ side of the system at earlier phases after periastron in the lower $\dot{M}_{\eta_A}$ simulations (Fig. B1, row e).

For most of the orbit, slices of the density and temperature in the *yz* plane are very similar for all three simulations since only the dense wind of η_A is sampled. The exception is around periastron, mainly for Case C (Figs B3 and B4). There is a clear density and temperature difference between the $+y$ and $-y$ sides of the system in the *yz*-plane slice for Case C at $\phi = 0.9$ (row b). This is because of Case C's extremely large WWC-cavity opening angle. Examination of row b of Fig. 1 shows that at $\phi = 0.9$, only in Case C has the leading arm of the WWC zone passed through the *yz* plane. In Cases A and B, the leading arm does not pass through the *yz* plane until close to $\phi = 1$ (Figs B3 and B4, row c).

Again, following periastron passage, η_B returns to the $+x$ side of the system, carving a new wind cavity along the way. We see in the density and temperature slices taken at $\phi = 1.03$ (Figs B3 and B4, row d) that this produces a difference in the size of the cavity on the $+y$ and $-y$ sides of the system. The magnitude of this difference increases with decreasing $\dot{M}_{\eta_A}$. The larger cavity on the $+y$ side of the system is the remnant of the WWC cavity from before periastron, while the smaller cavity on the $-y$ side is part of the new cavity created after periastron. A temperature difference also exists within the cavity, with the $+y$ side being much colder than the $-y$ side in the simulations for Cases A and B. After enough time passes, the new cavity on the $-y$ side of the system expands to a size comparable to the cavity on the $+y$ side, although there is still a clear difference in the temperature and density structure of the two cavities (Figs B3 and B4, row e).

B2 Results from the large-domain simulations

Figs B5 through B8 show density and temperature slices in the *xz* and *yz* planes at the same five orbital phases of Figs 8 and 9 for the large-domain 3D SPH simulations. There is a clear left–right asymmetry in the density and temperature in each panel of the figures. Fig. B5 shows that the higher the value of $\dot{M}_{\eta_A}$, the smaller the wind cavities carved by η_B on the $-x$ side of the system become in the *xz* plane. They are almost not visible in the Case A simulation, with the wind of η_A in the $-x$ direction looking continuous, but containing shells of enhanced density at periodic intervals. Fig. B5 also shows that the gradual fragmentation of the shell of dense η_A material on the $+x$ side of the system produces a series of small, cold, dense blobs within the larger, low-density wind cavity created by η_B. The higher the value of $\dot{M}_{\eta_A}$, the larger and denser these blobs are, and the longer they last before mixing with the surrounding η_B wind. Fig. B6 illustrates how in Case A, the winds on the $-x$ side of the system in the *xz* plane remain cold, while the wind cavity on the $+x$ side remains hot. In Cases B and C, the low-density cavities on both sides of the system remain hot, with only the intermediate regions of dense η_A wind cold.

In Fig. B7, we see that the extended narrow wind cavities on the $+y$ side of the system in the *yz* plane are always smaller than the wind cavities carved on the $-y$ side. These smaller cavities are always cold, while the larger cavities are always hot (Fig. B8). The difference in size between these cavities grows with decreasing $\dot{M}_{\eta_A}$. In Case A, the cavities are of comparable size, but in Case C, the cavities on the $-y$ side are much larger. The temperature of the gas in the $-y$ cavities is also nearly an order of magnitude hotter in Cases B and C than in Case A. Finally, the shells of dense η_A material on the $-y$ side of the system are thicker and remain intact longer in the higher $\dot{M}_{\eta_A}$ simulations.
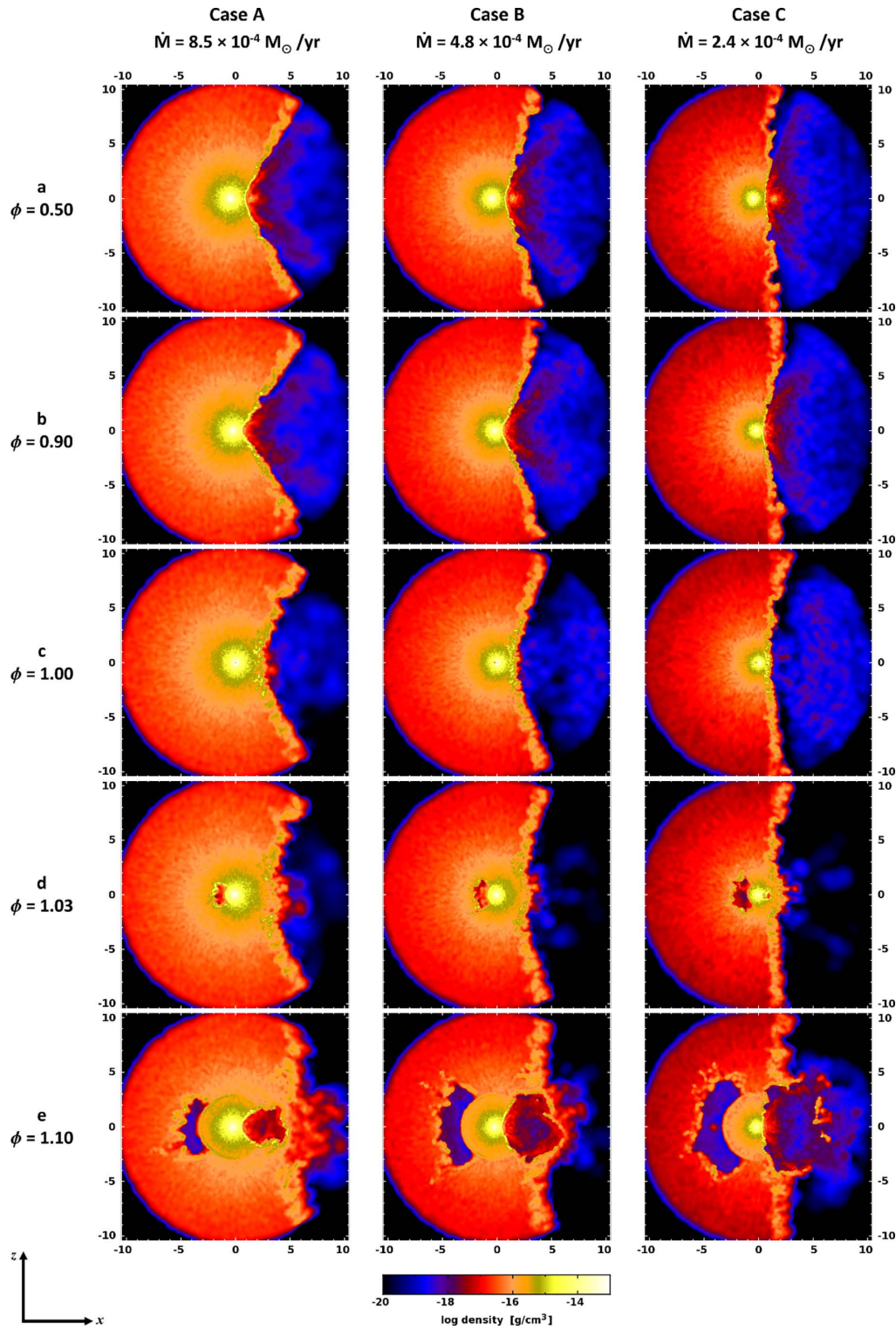
Figure B1. Same as Fig. 1, but for slices in the *xz* plane containing the binary semimajor (*x*) and orbital angular momentum (*z*) axes.
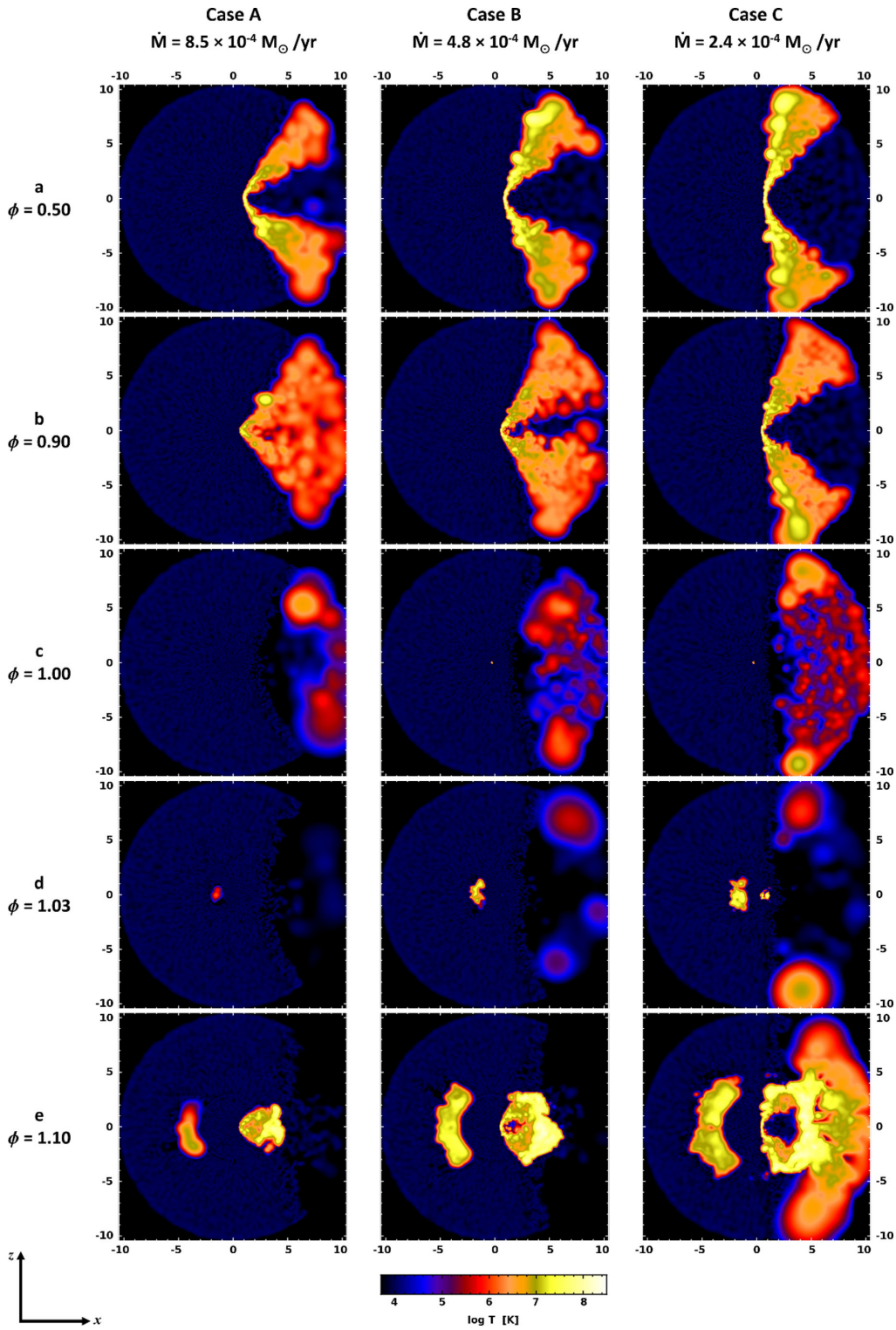
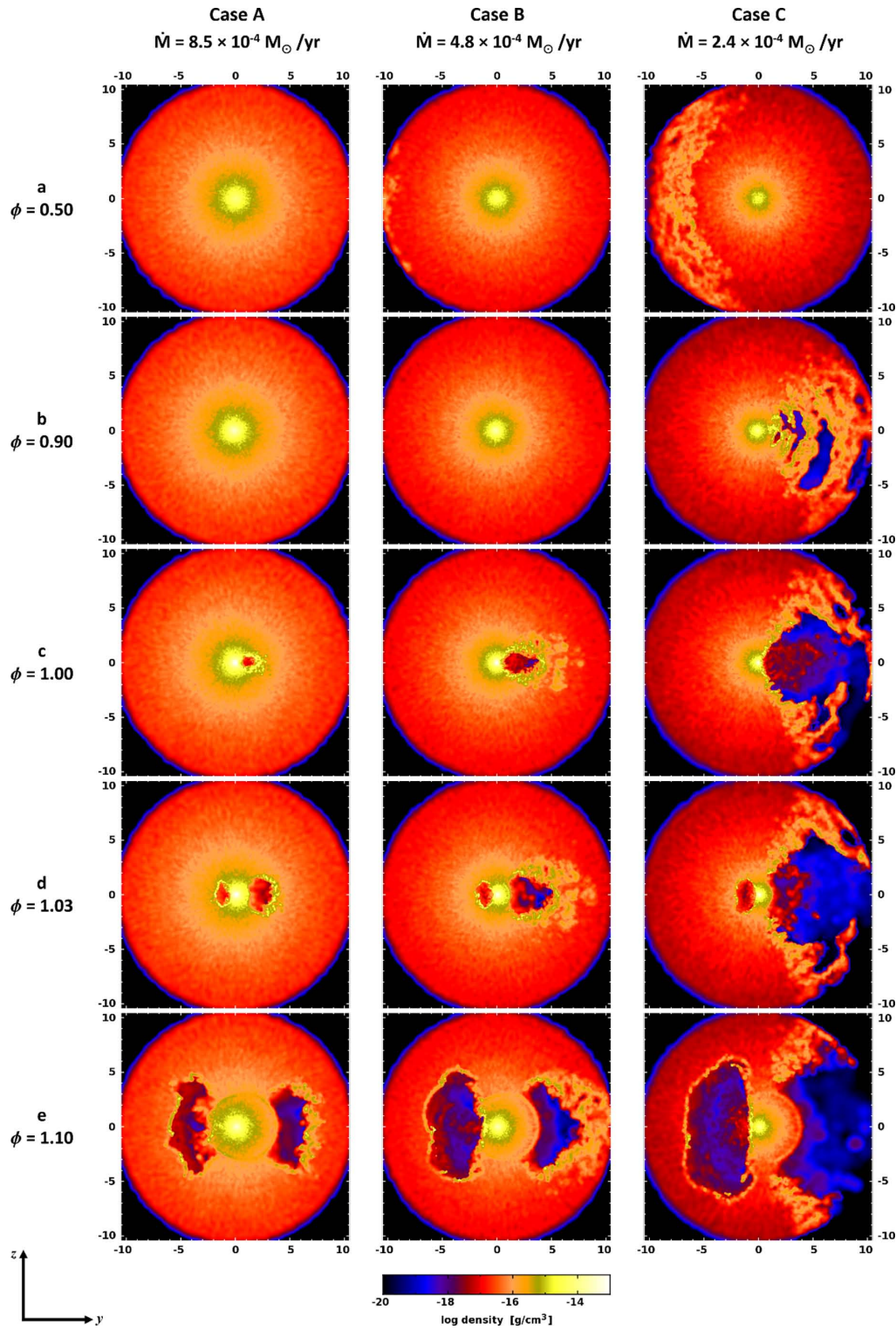**Figure B2.** Same as Fig. B1, but with colour showing log temperature.

Figure B3. Same as Fig. 1, but for slices in the *yz* plane containing the binary semiminor (*y*) and orbital angular momentum (*z*) axes.
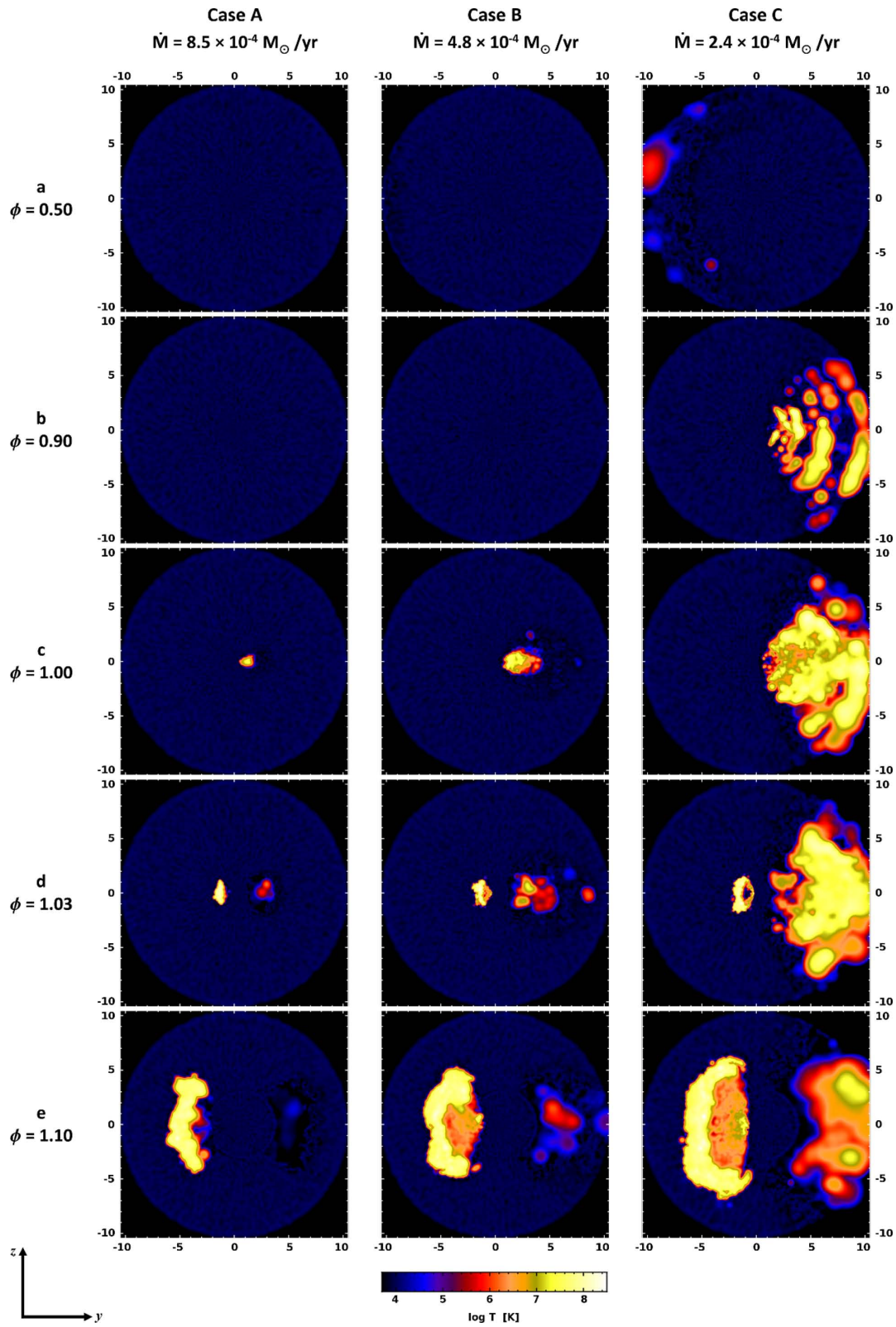
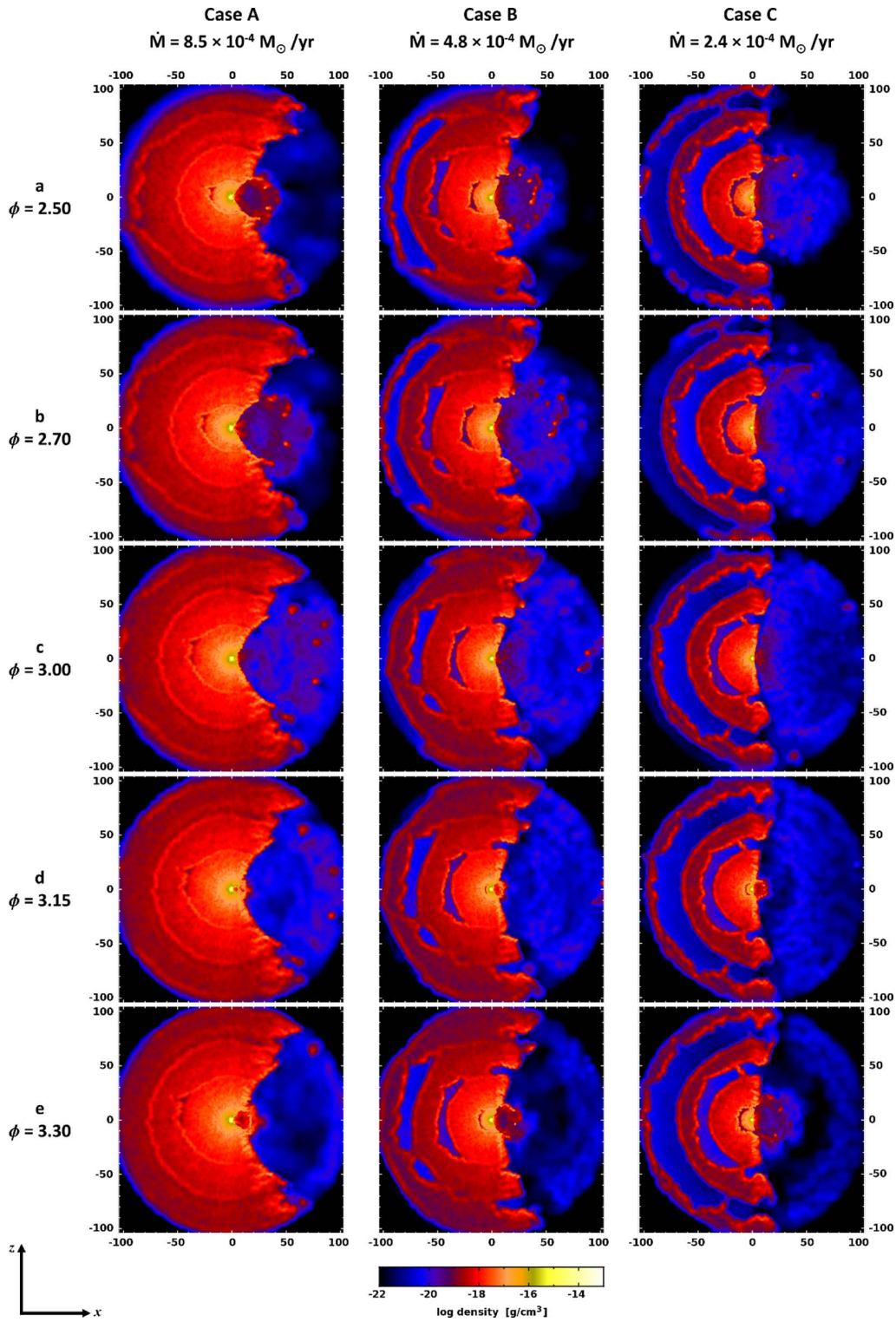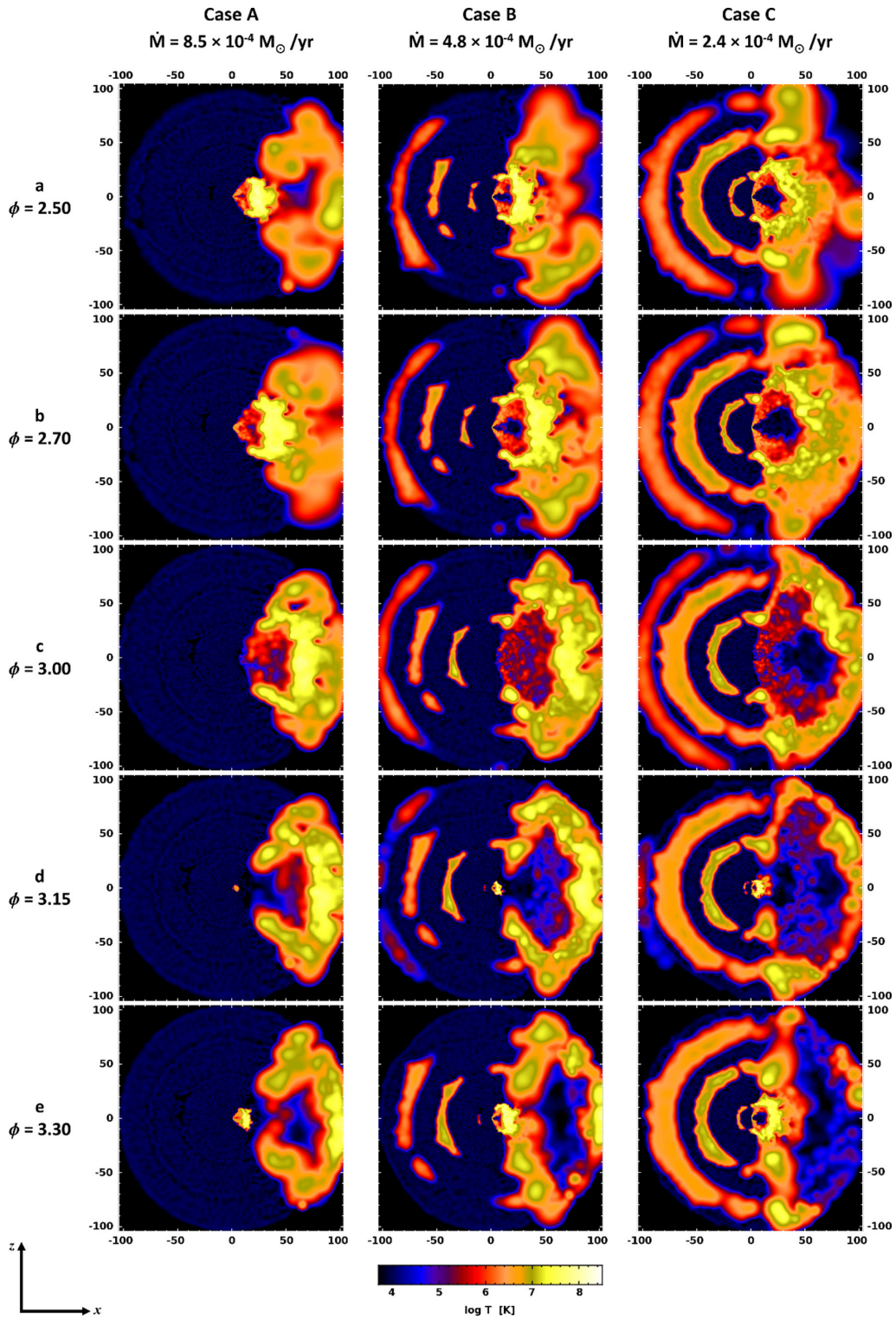**Figure B4.** Same as Fig. B3, but with colour showing log temperature.

Case A
$\dot{M} = 8.5 \times 10^{-4}$ M$_\odot$ /yr

Case B
$\dot{M} = 4.8 \times 10^{-4}$ M$_\odot$ /yr

Case C
$\dot{M} = 2.4 \times 10^{-4}$ M$_\odot$ /yr

log density [g/cm^3]

Figure B5. Same as Fig. 8, but for slices in the *xz* plane containing the binary semimajor (*x*) and orbital angular momentum (*z*) axes.

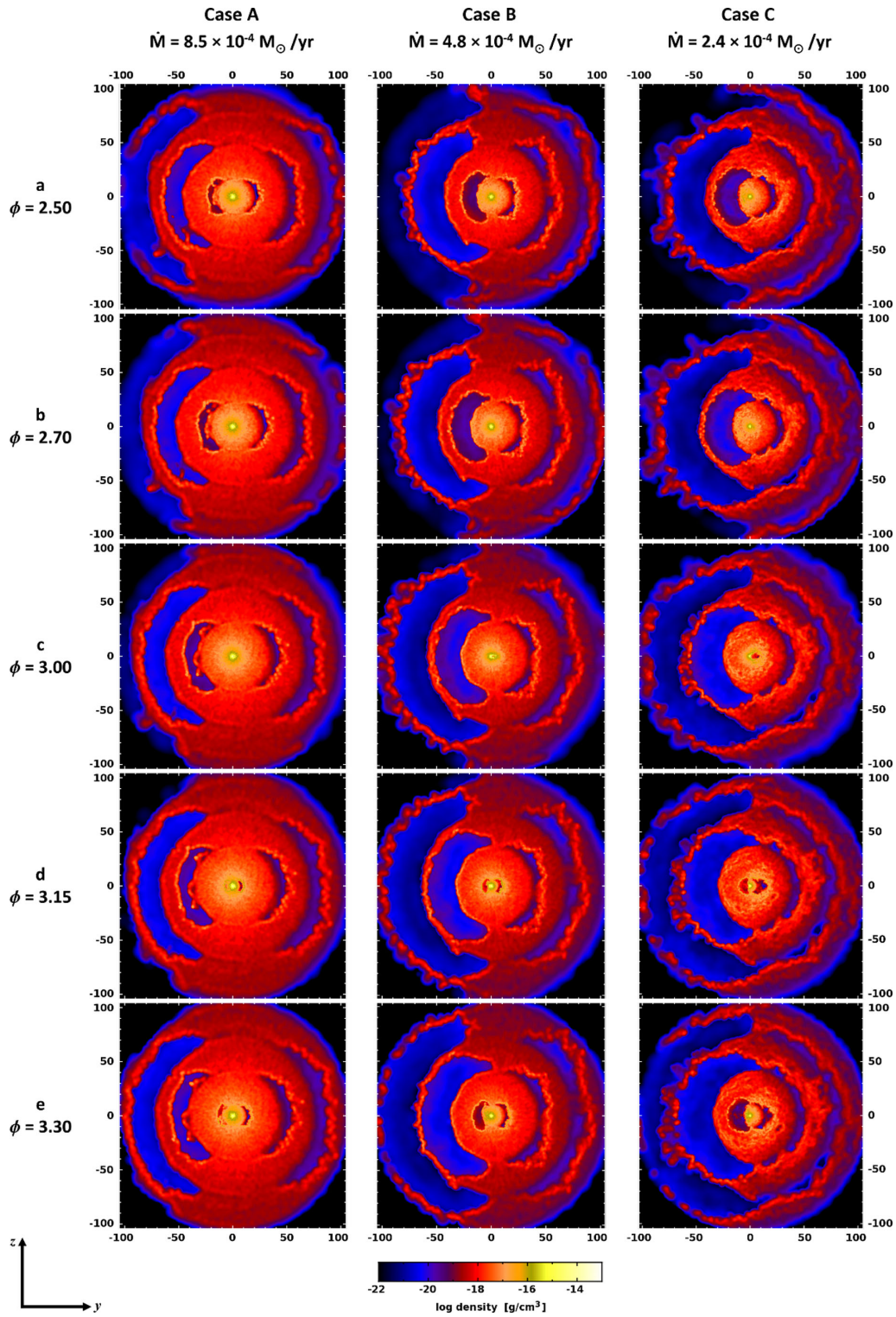**Figure B6.** Same as Fig. B5, but with colour showing log temperature.

Case A
$\dot{M} = 8.5 \times 10^{-4}\ M_\odot\ /yr$

Case B
$\dot{M} = 4.8 \times 10^{-4}\ M_\odot\ /yr$

Case C
$\dot{M} = 2.4 \times 10^{-4}\ M_\odot\ /yr$

a
$\phi = 2.50$

b
$\phi = 2.70$

c
$\phi = 3.00$

d
$\phi = 3.15$

e
$\phi = 3.30$

log density [g/cm^3]

Figure B7. Same as Fig. 8, but for slices in the *yz* plane containing the binary semiminor (*y*) and orbital angular momentum (*z*) axes.
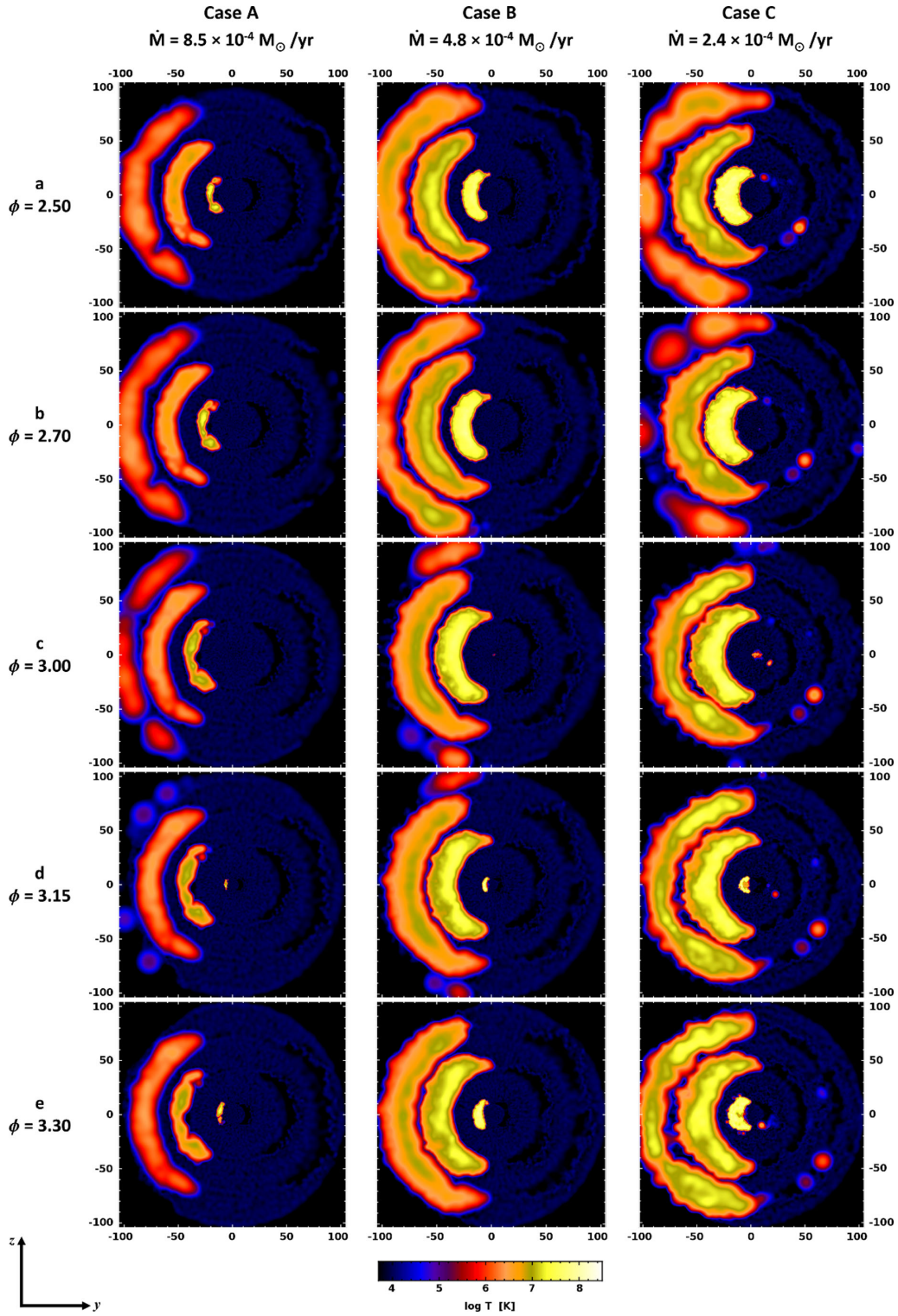
Figure B8. Same as Fig. B7, but with colour showing log temperature.

SUPPORTING INFORMATION

Additional Supporting Information may be found in the online version of this article:

Movies: Movies depicting the small-domain and large-domain simulations (http://mnras.oxfordjournals.org/lookup/suppl/doi:10.1093/mnras/stt1871/-/DC1).

Please note: Oxford University Press are not responsible for the content or functionality of any supporting materials supplied by the authors. Any queries (other than missing material) should be directed to the corresponding author for the article.

This paper has been typeset from a TEX/LATEX file prepared by the author.